JUSTUS-LIEBIG-
UNIVERSITÄT
GIESSEN

Mass measurements at the N=Z and N=126 limits at the FRS Ion Catcher and development of the Cryogenic Stopping Cell for the Super-FRS

Inauguraldissertation
zur Erlangung des Doktorgrades der
Naturwissenschaftlichen Fakultät der
Justus-Liebig-Universität Gießen

vorgelegt von

Daler Amanbayev
geboren in Chirchiq, Usbekistan

Fachbereich 07 - Mathematik und Informatik, Physik, Geographie

II. Physikalisches Institut, Justus-Liebig-Universität Gießen

December, 2023

Selbstständigkeitserklärung

Ich erkläre: Ich habe die vorgelegte Dissertation selbständig und ohne unerlaubte fremde Hilfe und nur mit den Hilfen angefertigt, die ich in der Dissertation angegeben habe. Alle Textstellen, die wörtlich oder sinngemäß aus veröffentlichten Schriften entnommen sind, und alle Angaben, die auf mündlichen Auskünften beruhen, sind als solche kenntlich gemacht. Ich stimme einer evtl. Überprüfung meiner Dissertation durch eine Antiplagiat-Software zu. Bei den von mir durchgeführten und in der Dissertation erwähnten Untersuchungen habe ich die Grundsätze guter wissenschaftlicher Praxis, wie sie in der „Satzung der Justus-Liebig-Universität Gießen zur Sicherung guter wissenschaftlicher Praxis“ niedergelegt sind, eingehalten.

Datum

Daler Amanbayev

Erstgutachter: Prof. Dr. Christoph Scheidenberger
Zweitgutachter: Prof. Dr. Kai-Thomas Brinkmann

Tag der Disputation: 04.12.2023

Contents

Motivation

"If you believe in things
That you don't understand
Then you suffer.
Superstition ain't the way!"

— Stevie Wonder, Superstition

Over the past century, nuclear physics has played a vital role in our understanding of the atomic nucleus, its structure and interactions. Most of this knowledge, however, originates from a few hundred nuclei that naturally occur on Earth. One of the ways of testing and improving our understanding is to study versions of nuclei with extreme ratios of neutrons to protons – the so-called exotic nuclei. They exhibit unusual phenomena, and their properties drive processes of creation of elements in the Universe. Exotic nuclei are created in stellar events and in radioactive ion beam (RIB) facilities. The research with exotic nuclei poses major challenges because these nuclei are unstable and can be produced in small quantities only. Furthermore, the more exotic the nucleus is, the larger is the difficulty to reach it.

There exists a gap between the nuclei that the scientific community is interested in and the nuclei that are accessible. One prominent instance is the rapid neutron-capture process (r-process), responsible for the creation of approximately half of the nuclei heavier than iron. The nuclei around N=126 which lead to the formation of the third r-process abundance peak (at A≈195) still cannot be accessed in state-of-the art RIB facilities. Therefore, the description of the r-process relies on predictions of theoretical models. The models quite often deviate from true values, and thus require new data to be validated against.

On the experimental side, this issue is approached from three perspectives: (i) building more powerful next-generation RIB facilities, (ii) pushing the limits of the existing RIB facilities by improving the instrumentation and detection methods, and (iii) exploring new techniques and reactions for producing the exotic nuclei. The example of the next-generation RIB facility is the Facility for Antiproton and Ion Research (FAIR), which is under construction at the GSI Helmholtz Center for Heavy Ion Research (Darmstadt, Germany). The superconducting fragment separator (Super-FRS) is the central instrument of FAIR's research program on nuclear structure, astrophysics and reactions.

This work contributes to our understanding of atomic nucleus by building an advanced and more powerful detection system, and demonstrating its potential to shrink the mentioned gap between "interesting" and "accessible". It is centered on a novel cryogenic stopping cell (CSC) for the Super-FRS at FAIR. The CSC converts

intense and fast beams of exotic nuclei of all elements produced at the Super-FRS into low-energy beams in a quick and efficient manner, to enable a variety of experiments *e.g.*, mass, decay and laser spectroscopy. In this work, its concepts are developed in detail to ensure the unprecedented performance parameters and maximize the discovery potential of these experiments at the Super-FRS, FAIR.

Furthermore, the CSC, as shown in this work, can be used for investigating reaction mechanisms. These include both conventional reactions like fission, projectile fragmentation and promising candidates like multi-nucleon transfer reactions, aimed to produce hard-to-reach very heavy neutron-rich exotic nuclei. The related developments are tested on a prototype of the CSC employed at the FRS Ion Catcher (FRC-IC) setup at GSI, and are part of this thesis.

The importance and potential of the system to improve our understanding of nuclear structure and reaction mechanism have been demonstrated in experiments conducted at the FRS-IC. There, the high-accuracy measurements of masses, isomer excitation energies and isomer-to-ground-state ratios were performed at the neutron-deficient and neutron-rich limits of the nuclide chart by the means of a multiple-reflection time-of-flight mass-spectrometry (MR-TOF-MS). The studies carried out in this work include the heaviest $N = Z$ nuclides as they provide an excellent opportunity to probe nuclear shell and mean-field models, the discovery of an isomeric state, and the lightest isotope measured so far at $N = 126$ as a milestone towards the third abundance peak of the r-process.

Chapter 1

From production to mass measurement

1.1 Production and separation of exotic nuclei

The access to exotic nuclei far from the valley of beta stability is complicated by their low production cross sections, short half-lives, and excessive background generated by unwanted products of the nuclear reaction.

Two techniques are commonly used nowadays: isotope separation online (ISOL) and in-flight separation. In both techniques, a mixture of exotic nuclei is produced in nuclear reactions between accelerated beam of projectile and a target. The reaction products are transported away from the high-background reaction site, and are purified and prepared to meet the requirements of the experimental setups downstream. The techniques are complimentary, and each has its advantages and drawbacks.

1.1.1 Isotope separation online technique

In the ISOL technique, the exotic nuclei are produced in target fragmentation (i.e. spallation or fission) reactions. Schematic outline of the technique is shown in Figure 1.1. A beam of protons of high energy of up to 4 GeV and high intensity of up to 100 μA impinges onto a thick target (areal density in the order of several 10 g/cm^2). The reaction products are stopped and thermalized in the target. They diffuse from the target and are transferred towards an ion source. The reaction products are ionized via various methods *e.g.*, electron impact, laser, surface ionization. Released from the ion source, singly-charged ions are accelerated to 10–60 keV, and mass separated by an electromagnetic separator. At this stage, the ions can be sent to low-energy experimental setups *e.g.*, for trapping and/or laser spectroscopy experiments, further separation or charge-breeding. Eventually, the ions can be post accelerated and sent to other experimental setups or for nuclear reactions in a secondary target.

Utilization of intense proton beams allows beams of exotic nuclei to be produced at exceptionally high rates. Another advantage is that the ions thermalized in the target are at rest and therefore are readily available for low-energy experiments and post acceleration. The major drawbacks of the ISOL technique are its

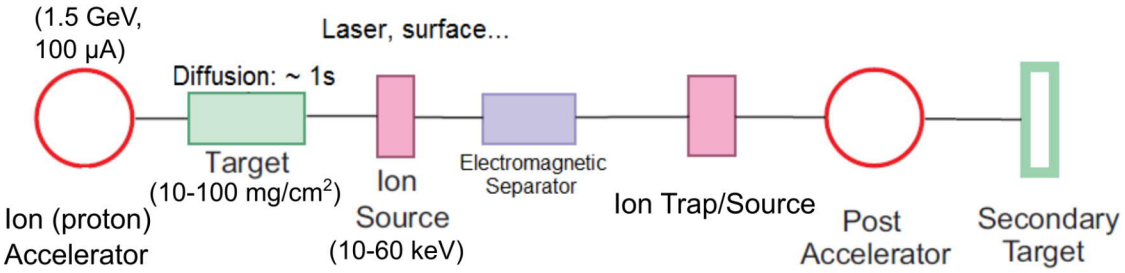

Figure 1.1: Schematic outline of the ISOL technique. See text for details. Adopted and modified from [Geissel et al., 1995].

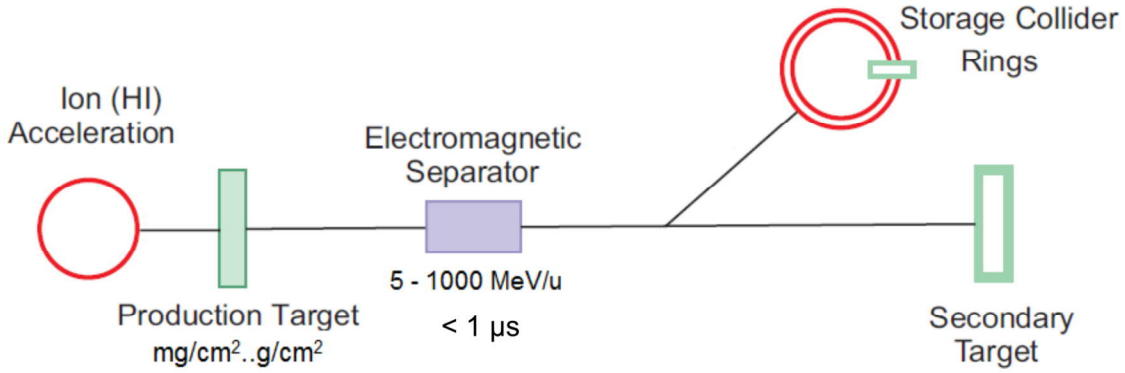

Figure 1.2: Schematic outline of the in-flight separation technique. See text for details. Adopted and modified from [Geissel et al., 1995].

slow ion extraction and element-dependence. The extraction time is in the best cases on the order of 0.1–10 s and is mainly limited by the diffusion and effusion (*i.e.*, release from the surface) of reaction products from the target. This imposes a limitation on half-life of isotopes of interest. The efficiency of these processes is strongly dependent on chemical properties of released elements, and is poor for refractory elements. This severely limits the production of isotopes of these elements. Another drawback is an isobaric contamination of secondary beams which cannot be suppressed by the electromagnetic separator. The issue is addressed by using multiple-reflection time-of-flight mass-spectrometers (MR-TOF-MS) as a high-resolution isobar separator *e.g.*, at TRIUMF's Ion Trap for Atomic and Nuclear sciences (TITAN) [Jesch et al., 2015, Dickel et al., 2019] and at Isotope Separator On Line DEvice (ISOLDE) [Wolf et al., 2013] facilities. Alternative approach is a selective laser ionization (see *e.g.*, [Raeder et al., 2014]).

1.1.2 In-flight separation technique

In the in-flight separation technique outlined in Figure 1.2, exotic nuclei are produced in nuclear reactions between heavy-ion primary beam and a production target (areal density of up to 10 g/cm^2). The primary beam is accelerated to energies near the Coulomb barrier for fusion or far above (in a GeV/u region) for projectile fragmentation and fission. Because of much higher energy and thus range of the reaction products compared to the ISOL technique, reaction prod-

ucts emerge ionized and with the velocity nearly equal to that of the projectile. Therefore, the delay between production and a final experiment setup is many orders of magnitude shorter giving access to even more exotic nuclei. The delay is determined by the flight time of the ions through the electromagnetic separator which is typically less than 1 μs. For the separation, Wien filters or gas-filled recoil separators are employed for fusion products (see *e.g.*, [Münzenberg et al., 1979], [M. Schädel, 2007]). In case of projectile fragmentation and fission, the so-called fragment separators are used. One particular example is the Fragment Separator FRS [Geissel et al., 1992] at GSI (see Section 2.1.1 for details).

Due to high energy of the fragments, it is possible to provide clean isotope beams even for heavy nuclei essentially free from isobaric contamination [Geissel et al., 1992]. The event-by-event identification allows to work with cocktail-beams.

Another distinctive advantage of the in-flight technique is its universality *i.e.*, it is independent of chemical properties of isotopes of interest.

After the separator, ions are relativistic and therefore can be sent to high-energy experiments or induce secondary reactions without additional acceleration stage. On the other hand, the ions have a broad angular and momentum spread, and therefore for the ISOL-type low-energy experiments they have to be slowed down and cooled *e.g.*, in a storage ring. The cooling time is in the order of few seconds [Geissel et al., 2004] which cancels the advantage of fast in-flight production and separation.

1.1.3 Hybrid technique

A hybrid technique bridges exotic nuclei produced at relativistic energies with low-energy experiments. The technique is outlined in Figure 1.3. Produced and separated in-flight, ions are thermalized in a gas-filled stopping cell *i.e.*, acquire the mean kinetic energy of the buffer gas atoms in the order of few tens of meV. Thermalized ions are extracted within 10–100 ms, and can be sent to ISOL-type low-energy experiments, post acceleration and secondary target.

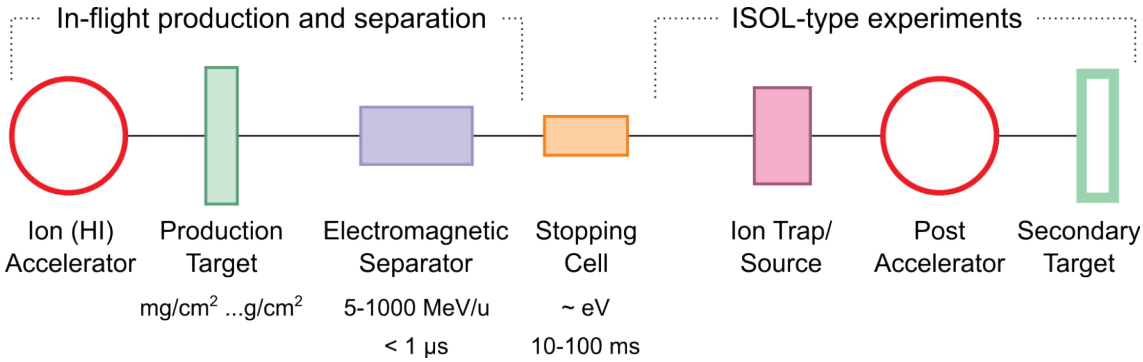

Figure 1.3: Schematic outline of the hybrid technique. See text for details. Adopted and modified from [Geissel et al., 1995].

The stopping cell is a key device to combine the advantages of in-flight and ISOL techniques. Not only it enables low-energy experiments previously non-

feasible at in-flight facilities, but it also extends the reach for such experiments to short-lived exotic nuclei of all elements inaccessible at ISOL facilities.

The performance of the stopping cell has to be carefully matched to the requirements of a particular facility, as it will be show in Section 1.2. The experimental results presented in this work have been obtained at the FRS Ion Catcher (FRS-IC) setup at GSI. The FRS-IC is a test bench for the hybrid technique and is described in Section 2.1. The stopping cell employed at the FRS-IC is a prototype of the future cryogenic stopping cell (CSC) for the Super-FRS at the Facility for Antiproton and Ion Research (FAIR). The development of the CSC is a part of this work and is presented in detail in Section 4.2.

1.1.4 Production using reactions in stopping cell

Nuclear reactions discussed so far produce fragments that are released at forward angles and at relativistic energies of >100 MeV/u. Stopping such energetic fragments *solely* in a gas-filled stopping cell is unfeasible, as explained in Section 1.2. In contrast, in reactions near Coulomb barrier energies and induced or spontaneous fission, the products emerge from the reaction target at energies of $\lesssim$3 MeV/u and are distributed over wide angles. Such kinematics is not optimal for conventional electromagnetic spectrometers because their angular acceptance is limited to few or few tens of mrad. Performing and studying such reactions directly inside a stopping cell *i.e.*, in-cell is advantageous because reaction products from a broad angular distribution can be effectively stopped in a buffer gas with an areal density of $\leqslant$5 mg/cm^2.

The multi-nucleon transfer (MNT) reactions are a promising tool which might provide a better access to neutron-rich heavy nuclei [Dasso et al., 1994, Watanabe et al., 2015]. Accessing these nuclei in post accelerator (ISOL) and in-flight facilities is a substantial challenge because the employed conventional nuclear reactions are not well-suited to populate the corresponding regions of the nuclide chart. Properties of these isotopes are essential for a better understanding of the stellar nucleosynthesis r-process and the mechanism of the MNT reaction itself. Although being known for decades, the reaction mechanism is still not well-understood. For instance, the production cross-sections predicted by state-of-the-art models for the same isotope differ by few orders of magnitude – from as low as 20 nb [Mun et al., 2014] to as high as 200 μb [Karpov and Saiko, 2017] for ^{204}Pt isotope. Studying the MNT reactions and measuring the cross-sections experimentally will provide an invaluable input to benchmark and improve the models.

Recent mass measurements of 19 neutron-rich isotopes of Pa–Pu at the limits of nuclide chart, and a discovery of a new isotope of ^{241}U [Niwase et al., 2023] at the KISS facility (RIKEN Nishina Center, Japan) is a remarkable demonstration of the potential of the MNT reactions.

Nuclear fission is one of the mechanisms that terminates the r-process cycle. Spontaneous fission is a primary decay mode of super-heavy nuclei. Technological applications of fission include nuclear energy production and monitoring, nuclear forensics, etc. Both fundamental and practical applications of fission show increased demand for high-quality data of fission observables including independent

isotopic fission yields (IIFY) and isomer yield ratios (IYR) [Dimitriou et al., 2016]. The available evaluations of fission data summarized in data libraries *e.g.*, ENDF [Brown et al., 2018] or JENDL [Shibata et al., 2011] are subject of discrepancies and errors. Measuring the IIFYs and IYRs directly *e.g.*, by ion counting is a reliable and straightforward way to resolve such discrepancies and to improve the underlying models.

At the FRS-IC at GSI, a novel technique to study the MNT reactions [Dickel et al., 2020] and spontaneous fission (SF) [Mardor et al., 2020] in-cell has been proposed. The technique includes (i) producing and thermalizing the MNT reaction or SF fragments in an ultra-clean and high-density environment of the cryogenic stopping cell, and (ii) identifying and counting the fragments in both ground and isomeric states with the multiple-reflection time-of-flight mass-spectrometer. A combination of performance characteristics of the FRS-IC offers a unique opportunity to carry out and study these reactions in a fast, sensitive, broadband, non-scanning, almost element-independent and efficient manner. Furthermore, unique to the FRS-IC is a possibility to utilize not only stable primary beams but also secondary radioactive beams of neutron-rich heavy nuclei available at the FRS (and at the Super-FRS in the future) to carry out the MNT reactions. This aspect is of great advantage since a larger neutron excess in the beam translates into a better production of even more neutron-rich isotopes.

The dedicated modifications and developments are part of this thesis and are described in Section 4.1.

1.2 Thermalization of radioactive isotope beams in stopping cells

A stopping cell is a chamber filled with a buffer gas and equipped with means for transporting and extracting stopped ions. Its primary function is a fast and universal conversion of high-energy and large-emittance beams into low-energy and low-emittance beams.

The stopping cell method has its origin in the ion guide isotope separator online (IGISOL) technique developed at University of Jyväskylä (JYFL, Finland) in 1980s [Ärje and Valli, 1981]. The IGISOL technique enabled low-energy beams of all elements including non-volatile refractory elements which could not be produced at conventional ISOL facilities (see Section 1.1.1).

The gas-filled stopping cells have become an integral part of radioactive isotope beam (RIB) facilities worldwide in the last few decades [Wada, 2013]. Their success is evidenced by an impressive variety of applications including and not limited to:

- direct mass measurements of nuclei
  - towards the N=Z line [Mardor et al., 2021]
  - relevant for rp-process [Savory et al., 2009]
  - beyond the proton drip line [Rauth et al., 2008]
  - of super-heavy elements [Block et al., 2010, Block et al., 2022]

- in-gas-jet laser spectroscopy [Ferrer et al., 2017]
- laser spectroscopy of halo nuclei [Takamine et al., 2014]
- measurements for neutrino physics [Lincoln et al., 2013]
- tests of standard model [Sternberg et al., 2015, Burkey et al., 2022]
- direct detection of the nuclear clock transition in ^{229}Th [von der Wense et al., 2016]
- direct determination of decay branching ratios [Miskun et al., 2019]

These applications have vastly different requirements and conditions, and it is clear that no stopping cell can satisfy all the requirements. The layout, operational parameters, dimensions and ion transport and extraction techniques of each such device are developed custom-tailored to the characteristics of a particular facility and envisioned physics program.

The stopping cells can be divided into two groups based on the ion transport technique they implement: (i) gas flow only, and (ii) electric fields and gas flow. Such grouping provides a convenient basis for an overview.

Gas flow only

Transport by gas flow is realized when the use of electric fields is unfeasible due to very high intensity of incoming beam. The plasma induced in the buffer gas contains both positive ions and free electrons, therefore a major challenge lies in the fact that the ions of IOI are neutralized via plasma recombination. Given the timescale of recombination process of $\sim$10 ms, one approach to minimize ion loss is a fast extraction. This is known as the IGISOL method. In an alternative approach, one forces the neutralization of ions and then re-ionizes the IOI. This is known as the IGLIS method.

Fast ion extraction – the IGISOL method

In order to reach short extraction time, the dimensions of the corresponding stopping cells have to be small because transport by the gas flow is slower than transport by electric fields. In the original IGISOL facility, a production target was placed inside a small gas cell (1–2 cm^3) filled with 100 mbar helium at room temperature and was bombarded by a 20 MeV proton beam of up to 100 nA ($\sim 10^{12}$ pps) intensity. The strength of the method was demonstrated by production and extraction of a ^{182}W^m isomer with a half-life of 5.5 ms [Ärje et al., 1985].

In the present version of the facility known as IGISOL-4 [Moore et al., 2013], several dedicated stopping cells (called ion guides) are in use, each adapted to increased intensities (up to 100 μA for protons) and variety of primary beams. These include proton-induced fission ion guide [Taskinen et al., 1989, Al-Adili et al., 2015] and HIGISOL ion guide for reactions induced by heavy-ion primary beams [Kessler, 2008]. The original IGISOL stopping cell has seen minor changes and is still employed for proton-induced fusion-evaporation reactions. Its layout is shown in Figure 1.4a.

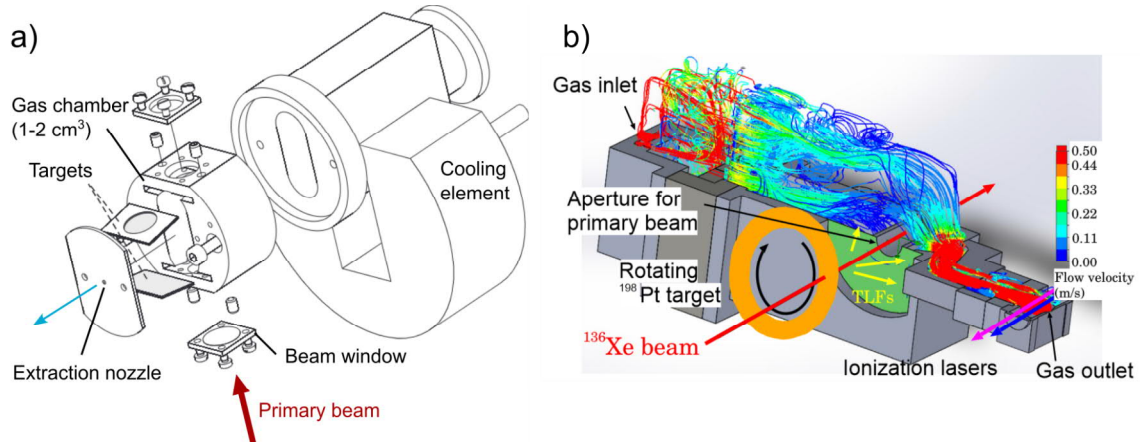

Figure 1.4: Examples of the gas-flow-only stopping cells: (a) the IGISOL gas cell [Elomaa, 2009], (b) the KISS gas cell [Hirayama et al., 2017] based on the IGLIS method [Kudryavtsev et al., 2013]. Gas-flow-only stopping cells are compact and well-suited for low-energy reaction fragments. Upsizing them for higher energies will result in pointlessly long ion extraction. See text for details.

Neutralization and re-ionization – the IGLIS method

At high intensity of primary beam, the strength of the IGISOL method – chemical non-selectivity – transforms into a weakness. A signal from very exotic IOI can be lost in a strong isobaric background. Therefore an alternative approach was developed for the Leuven isotope separator on-line (LISOL) [Vermeeren et al., 1994, Kudryavtsev et al., 1996], where all thermalized ions are neutralized in buffer gas, transported by the gas flow towards the nozzle, and shortly before leaving selectively ionized by lasers. This way a universal production is combined with high isobaric selectivity. By coupling it to a mass separation stage downstream, an isotopic selectivity is achieved.

High selectivity of the method allows to perform laser spectroscopy in the buffer gas (in-gas-cell) or in the supersonic gas jet emerging from the nozzle (in-gas-jet) [Kudryavtsev et al., 2013]) to measure *e.g.*, charge radii and nuclear magnetic moments [Cocolios et al., 2009, Ferrer et al., 2014, Ferrer et al., 2017]. This is a so-called in-gas laser ionization and spectroscopy (IGLIS) technique.

In order to force ion neutralization, argon buffer gas is preferred over helium as the former has higher plasma recombination rate. Note that the IGLIS method converts into the IGISOL if the helium is used as a buffer gas. The trade-off between the size of the stopping volume and the evacuation time is similar to the IGISOL method.

An example is a doughnut-shaped gas cell for KEK Isotope Separation System (KISS) facility at RIKEN Nishina Center, Japan (Fig 1.4b) [Hirayama et al., 2017]. It thermalizes target-like fragments (TLFs) produced in MNT reactions (see Section 1.1.4) between ^{136}Xe beam and ^{198}Pt target upstream. Since TLFs recoil at the energy of $\sim$1 MeV/u and are distributed over wide angles, the KISS gas cell has a relatively large stopping volume, however, at the expense of slower ion extraction. The mean extraction time of 500 ms at the pressure of 880 mbar in argon was

measured [Hirayama et al., 2017].

The in-cell technique for MNT reaction studies at the FRS-IC, GSI (see Section 1.1.4) will be complimentary to the KISS.

A curious application of the IGLIS method is a parasitic RIB production by laser ion-source (PALIS) under development at RIKEN, Japan [Sonoda et al., 2013]. It is located at the central focal plane of the BigRIPS fragment separator [Kubo, 2003], with the aim to thermalize an unused part of secondary beams which is otherwise lost in the slits. The availability of PALIS setup will result in a more efficient use of the precious beam time. First tests showed, however, that the plasma induced by a passage of high-energy and intense beam prevents proper extraction of stopped nuclides [Sonoda et al., 2020].

As a part of this thesis, an alternative approach has been developed. In this approach, the mean ranges of ions of all nuclides which compose the beam are aligned and bunched such that multiple nuclides can be stopped in the stopping cell simultaneously. The technique is described in Section 2.2.

Other examples of IGLIS-type stopping cells include a prototype of the future S^3–Low Energy Branch (LEB) facility at GANIL, France [Kudryavtsev et al., 2016, Ajayakumar et al., 2023] and a stopping cell for the MARA-LEB facility at JYFL, Finland [Papadakis et al., 2016].

Electric fields and gas flow

The stopping cells of IGISOL and IGLIS types are compact and well-suited for low-energy reaction fragments ($\sim$0.1 MeV/u). However, efficient stopping of fragments at higher energies requires a much larger stopping volume at a given areal density. The ion extraction solely by gas flow from a large volume is slow – it would take tens of minutes which is far from being useful. The large-volume stopping cells employ electric fields to overcome this limitation. The extraction time as low as few tens of milliseconds are achieved.

The following briefly describes how ion transport is organized in the stopping cells of present group. A detailed description can be found in Appendix A. The thermalized ions are guided towards extraction by a so-called pushing DC field. The ion motion occurs along the electric field lines superimposed on isotropic (*i.e.*, directionless) diffusion in gas (Section A.2). The guided ions will terminate on electrodes and therefore will be lost. In order to prevent this, a radio frequency (RF) electrode structure is placed in the path of the ions [Masuda et al., 1972, Wada et al., 2003]. It generates an effective RF field which counteracts the pushing field, and thus repels the ions allowing them to be stored above the surface (Section A.3). These structures are typically shaped as cones (RF funnel) or have a planar geometry (RF carpet). Several examples are shown in Fig. 1.7. Next, the stored ions are transported along the RF carpet (or funnel) surface towards an exit hole *i.e.*, an orifice or a *de Laval* nozzle where they are pushed through by the gas flow and are eventually extracted out of the stopping cell. The transport along the RF carpet can be realized by imposing a DC gradient which generates a focusing field or using a so-called “ion surfing” technique.

The stopping cells of present group are employed to thermalize low-energy

beams *e.g.*, ∼0.1 MeV/u recoils of fusion-evaporation reaction, as well as high-energy beams *e.g.*, ∼1 MeV/u spontaneous fission fragments, and relativistic secondary beams of exotic nuclei produced in-flight at several 100 MeV/u. The intensity of such beams is many orders of magnitude lower compared to that of primary beams in IGISOL or IGLIS methods. This makes the application of electric fields feasible.

The ions lose energy primarily via inelastic collisions with electrons of buffer gas atoms. The amount of energy transferred in a single collision between an ion and an electron fluctuates due to the statistical nature of the process. After multiple collisions the width of the initial energy distribution of ions broadens. Such broadening is referred to as energy-loss straggling. It also follows that the distance ions travel in matter before full thermalization is statistically distributed. The mean and standard deviation of this distribution are called range and range straggling (Section A.1).

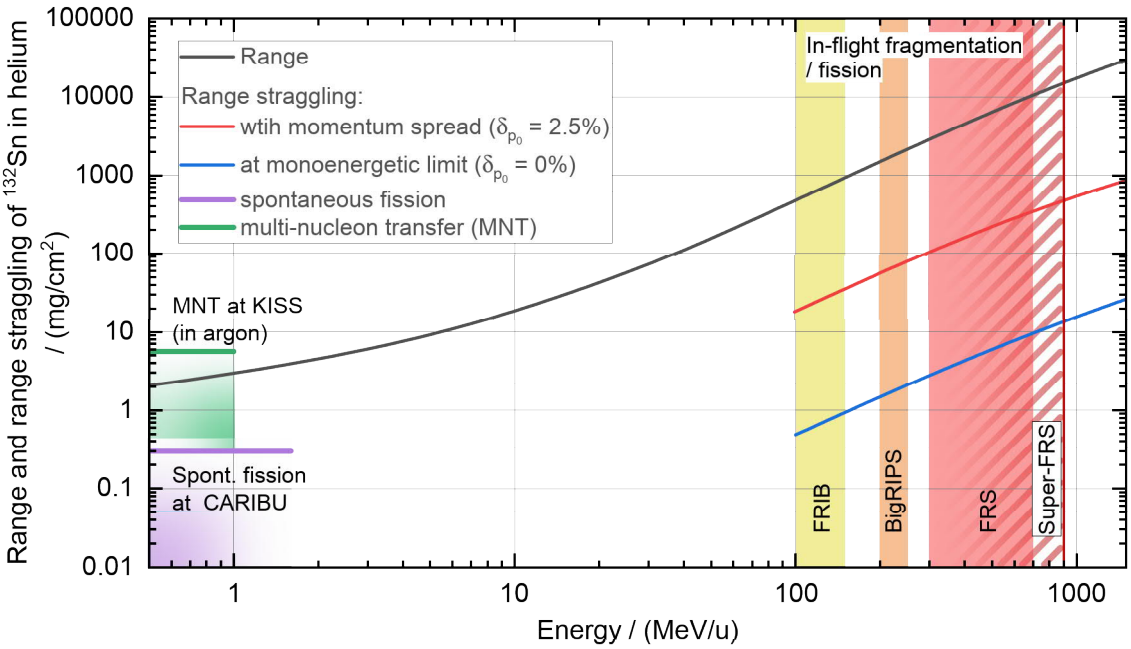

Figure 1.5: Range and range straggling of ^{132}Sn in helium as a function of energy. Boundaries of colored regions indicate the energy range of spontaneous fission fragments of ^{252}Cf (violet), energy range of recoils of multi-nucleon transfer (MNT) reactions at KISS facility (green), beam energies at the momentum compression stage at the FRIB (yellow), BigRIPS (orange), FRS (red) and Super-FRS (hashed red) fragment separators. The range (black curve) is absorbed in degraders upstream, leaving only the range straggling for the stopping cell to thermalize. The range straggling of a beam with a relative momentum spread of $\delta_{p0} = 2.5\%$ (red curve) is unbearable. The range straggling is the smallest at monoenergetic limit $\delta_{p0} = 0\%$ (blue curve). Range straggling for spontaneous fission and MNT is shown as violet and green lines correspondingly.

In order to ensure **efficient stopping**, the buffer gas needs to contain enough

atoms to absorb the energy and energy straggling of incident ions. This is achieved when the areal density of buffer gas is matched with the range or range straggling of incident ions. Figure 1.5 shows the calculated range and range straggling of ions of ^{132}Sn in helium as a function of energy. Colored rectangles mark the energy regions relevant for spontaneous fission (violet), multi-nucleon transfer (green), and in-flight fragmentation and fission (yellow, orange and red). The calculations were performed with ATomic Interactions in MAtter (ATIMA) code [Weick et al., 2018]. Proportionality relations in Eq. A.4–A.5 can be used to scale the values for other nuclei of interest. In all cases, the ions lose most of their energy (*i.e.*, spend their range) in solid degraders or reaction target located upstream. The stopping cell only needs to thermalize the remaining range straggling.

The californium rare isotope breeder upgrade (CARIBU) gas catcher at Argonne National Laboratory (ANL), shown in Fig. 1.6a, thermalizes spontaneous fission fragments of ^{252}Cf [Savard et al., 2016]. The fragments are emitted in the energy range of 0.2–1.6 MeV/u (shown by the boundaries of the violet region in Fig. 1.5). Each fragment has a fixed energy and a negligible energy spread. Before entering buffer gas, the fragments isotropically pass through a half-sphere degrader, where they lose ∼90% of their energy. The remaining energy translates into the range of $\leqslant$0.5 mg/cm^2. This is equivalent of $\leqslant$30 cm in helium at pressure of 100 mbar and temperature of 298 K. The range has to be accommodated both axially and radially because the fragments are distributed isotropically. With an areal density of 2 mg/cm^2 and diameter of 50 cm, the CARIBU gas catcher thermalizes most of the fragments. In Fig. 1.5, violet line indicates the range straggling of ^{132}Sn produced in spontaneous fission at CARIBU.

The in-cell technique at the FRS-IC (Section 1.1.4) and the related setup (Section 4.1) are also suited for spontaneous fission studies.

For the MNT reaction at the KISS gas cell mentioned earlier, the recoil energy of ∼1 MeV/u translates into the range of 5.6 mg/cm^2 in argon. This is equivalent of $\leqslant$7 cm at pressure of 500 mbar and temperature of 298 K. For both KISS and CARIBU, efficient stopping is not problematic, except for wide angular distribution of fragments. High beam intensity is what presents the key difficulty for these gas cells, as discussed later in this section.

Efficient stopping becomes significantly more challenging at the energies of in-flight fragmentation and fission of $\geqslant$100 MeV/u because the range (Fig. 1.5, black curve) grows rapidly with energy. This makes the momentum spread of the beam a major point of consideration. A non-zero width of the beam momentum distribution results in substantial increase in the range straggling. As shown in Fig. 1.5, the range straggling of ^{132}Sn ion beam with a relative momentum spread of $\delta_{p0} = 2.5\%$ (red curve) reaches few 100 mg/cm^2 in the most energetic cases. This is equivalent of >60 meters in helium (100 mbar, 298 K). Clearly, a stopping cell of such length is unfeasible. The range straggling is the smallest in case of a monoenergetic beam *i.e.*, $\delta_{p0} = 0\%$ (blue curve). Compressing momentum spread of the incident beam to its monoenergetic limit is therefore a prerequisite for efficient stopping within a gas cell of a feasible length. This compression can be elegantly performed by dispersing the beam across a wedge-shaped degrader in an ion-optical electromagnetic separator such as the FRS at GSI [Geissel et al., 1989]. The energy of the ion beam at this stage is what defines the range straggling that the stopping

cell needs to handle. In Fig. 1.5, the boundaries of the yellow, orange, red and hashed red regions indicate such energies at the FRIB [Hausmann et al., 2013], BigRIPS, FRS and future Super-FRS fragment separators correspondingly.

At the FRS, even at monoenergetic limit the range straggling still reaches 10 mg/cm^2, equivalent to >6 m helium (100 mbar, 298 K). More realistic dimensions of a stopping cell of 1–2 m requires a corresponding increase in buffer gas density ρ. The density cannot be elevated to an arbitrarily high level as it negatively impacts the effective field of an RF carpet/funnel as $E_{\text{eff}} \propto (1/\rho)^2$ (see Eq. A.17). Keeping gas density below the RF carpet/funnel limit has to be compensated by an increase in the length of the stopping volume d, which however translates into slower ion extraction as $t \propto d^2$ (see Eq. A.13). Therefore, trade offs are made between stopping efficiency, extraction efficiency and extraction time.

The cryogenic stopping cell (CSC) at the FRS-IC, shown in Fig. 1.6b, handles relativistic ion beams produced at the FRS at unprecedented energies. Its state-of-the-art performance has been demonstrated in a series of experiments at GSI as well as under challenging conditions of FAIR Phase-0. Two such experiments exploring the regions of the heaviest $N = Z$ nuclei and the lightest $N = 126$ nuclei are subject of this thesis (see Section 2.3 and Chapter 3). After recent technical upgrades, the CSC features an areal density of 9 mg/cm^2 [Miskun, 2019] which is about a factor of two higher compared to what has been achieved worldwide so far. A detailed description can be found in Section 2.1.2.

The CSC at the FRS-IC also serves as a prototype of a cryogenic stopping cell for the Super-FRS at FAIR. Throughout this work, the CSC at the FRS-IC is referred to as “the prototype CSC”, and the CSC for the Super-FRS – as “the CSC”. Development of the CSC for the Super-FRS is a subject of this thesis and is described in Chapter 4.2.

In the stopping cells of the present group, **high extraction efficiency** is achieved because the electric fields separate stopped ions from free electrons, generated during the stopping process, which results in significantly lower ion recombination compared to that of the IGISOL technique.

Electric fields also speed up ion extraction, which reduces losses due to diffusion (Section A.2) and is of great importance for avoiding chemical reactions between IOI and impurity molecules in buffer gas. As explained in Section A.5, a concentration of impurity below 1 ppb level is required. No commercially available gas meets this requirement, therefore various active and passive gas purification systems are used in all stopping cells. Examples of such systems can be found in [Sonoda et al., 2016, Pohjalainen, 2018, Mollaebrahimi, 2021]. In addition, other components of the stopping cells are built to ultra-high-vacuum standards. Further, gas purification can be achieved by operating stopping cell at cryogenic temperatures [Dendooven et al., 2006]. In addition, a so-called collision induced dissociation (CID) technique can be used to partly recover IOI from its molecular ion form. This applies both to gas-flow-only and electric-fields stopping cells [Schury et al., 2006, Raeder et al., 2016, Greiner et al., 2020, Jacobs et al., 2022].

At high rates of incoming ions, the efficiency of ion extraction from a stopping cell decreases. This phenomenon is known as space-charge effect [Takamine et al., 2005, Savard, 2011]. Several approaches to handle high-

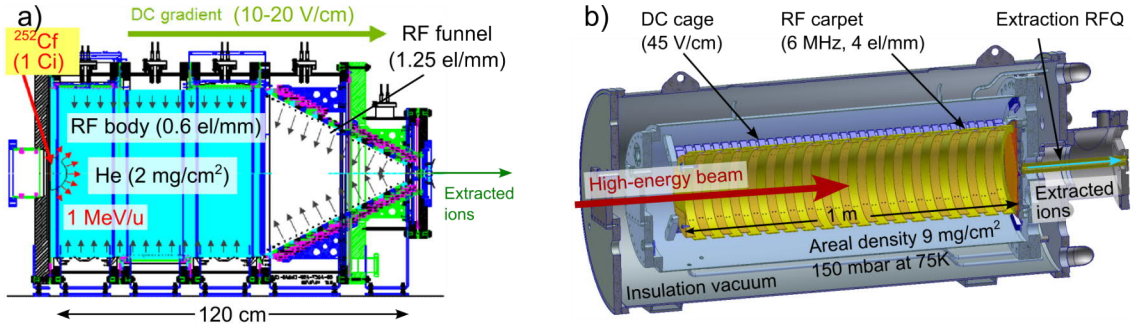

Figure 1.6: Examples of electric-fields stopping cells: (a) CARIBU gas catcher, (b) cryogenic stopping cell at the FRS Ion Catcher. Please see text for details

intensity beams exist. As explained in Section A.4, these approaches are based on (i) dumping the charge carriers with low m/q at the RF carpet or funnel while transporting the IOI with higher m/q ($E_{\mathrm{RF}} \propto m/q$, see Eq. A.17), and (ii) on maximizing the electric field in the bulk of the stopping volume. The examples of (i) are:

- In CARIBU gas catcher, mentioned earlier, the source of ^{252}Cf has an activity of more than 1 Ci. It generates extreme ionization current of about 0.1 mA, considering a spontaneous fission branch of 3.1%, mass and energy distribution of fission fragments, and a comparable contribution from the remaining alpha-decay branch. In order to tolerate such a high ionization rate, the RF structures cover the entire inner surface of the stopping volume of CARIBU, not the RF funnel alone (Fig. 1.6a). The downside of this solution is increased amount of heat deposited from RF which is of the order of 250 Watts [Savard et al., 2016].

- In Advanced Cryogenic Gas Stopper (ACGS) [Lund et al., 2020] at FRIB, an RF wire-carpet is located at mid-plane of the stopping volume. This configuration helps removing the excessive charge density. Handling intense beam rates of up to 10^7 ions/s is reported [Lund et al., 2020], however without indicating the extraction efficiency behavior.

The CSC for the Super-FRS is required to handle ion beams with the rates of $\geqslant 10^7$ ions/s, which is 3 orders of magnitude larger than what has been achieved [Reiter et al., 2016] with its prototype at the FRS-IC. For this, several new concepts based on (i) and (ii) will be implemented. Within the context of this thesis, a concept of orthogonal extraction (an example of (ii)) has been tested, as presented in Section 4.1.3. The orthogonal extraction is being tested independently at the SLOWRI prototype gas cell at BigRIPS [Takamine et al., 2019].

As mentioned earlier, the stopping cells of this group are equipped with **RF funnel** or **RF carpet** (see Figure 1.7 and Section A.3). The RF funnels can be made of ultra-high-vacuum compatible materials which is beneficial for the gas cleanliness. A strong side of the RF carpets is that it can be manufactured with higher electrode density – up to 5 electrodes/mm compared to 1 electrode/mm of the RF funnels – and therefore can produce more than a factor of 125 stronger

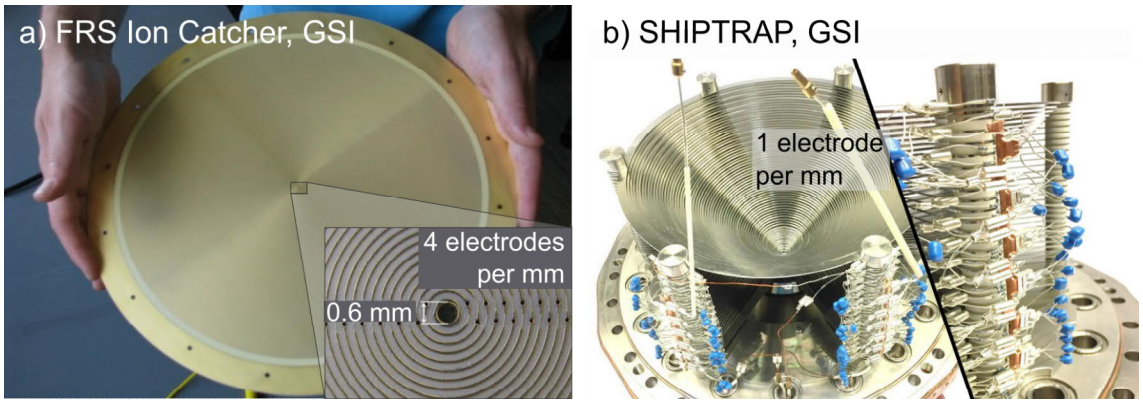

Figure 1.7: Examples of an RF carpet and an RF funnel: (a) PCB-based multi-layered RF carpet in the cryogenic stopping cell at the FRS Ion Catcher, GSI [Ranjan, 2012]; (b) RF funnel in a cryogenic gas cell at SHIPTRAP, GSI [Droese et al., 2014]. Higher electrode density translates into stronger effective repelling field which makes RF carpets better-suited for a high gas density and a strong pushing field conditions.

effective repelling RF field as it follows from Eq.A.17. Therefore, the RF carpets are better suited for high gas density and strong pushing field conditions. In addition, both RF funnels and carpets are able to separate atomic and molecular ions by their ion mobility [Miskun et al., 2021].

Other stopping cells exist *e.g.*, SHIPTRAP cryogenic gas cell (GSI, Germany) [Droese et al., 2014, Kaleja, 2020], GARIS-II gas cell (RIKEN Nishina Center, Japan) [Schury et al., 2016, Shikegava et al., 2021], MLL-IonCatcher gas cell (Maier-Leibnitz Laboratory, Germany) [Neumayr et al., 2006]. In addition, the gas-flow-only concepts of large-volume stopping cells are proposed *e.g.*, UniCell [Varentsov and Yakushev, 2019] and FAIR-wind gas cell [Varentsov and Yakushev, 2021]. These examples, while occasionally omitted from the discussion above, share a common ground and are subject to the same principles and considerations presented in this section.

This section shows that no single stopping cell can meet the diverse requirements across all applications. Each application pushes the boundaries of what is possible, presenting its distinct set of challenges that demand tailored solutions. Gas-filled stopping cells through their inventive design variations offer ways to address these challenges, highlighting their significant scientific potential.

1.3 Techniques for high-accuracy mass measurements

The methods of nuclear mass measurements can be divided in two groups: indirect and direct. The indirect method is based on measuring Q-value of a nuclear reaction. In case of radioactive decay, the kinetic energy of the emitted particles is measured. The unknown mass is deduced if the masses of other reaction products are known. Among the strengths, the knowledge of one mass can anchor calculations of all unknown masses in a decay chain [Dworschak et al., 2010].

The major drawback is related to the fact that correct determination of Q-value often requires spectroscopic information which is scarce, especially for exotic nuclei [Roeckl, 2001]. This might result in substantial systematic deviations of indirectly measured masses from the true mass surface.

The direct methods are based on interaction of ions with external electromagnetic fields. The mass is determined by measuring the oscillation frequency of an ion or its time of flight, and comparing it to that of nuclides with well-known masses. Three high-precision techniques employed nowadays are Penning trap, storage ring, and multiple-reflection time-of-flight mass spectrometry. With unstable nuclei these techniques achieve relative mass uncertainty of $\delta m/m = 10^{-7}$ routinely and down to $\delta m/m = 10^{-8}$ state-of-the-art which is sufficient to address the physics questions in the fields of nuclear fine structure, astrophysics, weak interaction and to test nuclear mass models [Blaum, 2006]. Each technique has its strengths in terms of precision, resolution, measurement time, sensitivity and mass range, and is briefly introduced below.

In **Penning traps**, the ions are trapped radially in a homogeneous magnetic field and are confined axially in a quadrupole electric field. The ion motion is described by one axial ω_z, and two radial – modified cyclotron ω_+ and magnetron ω_- – independent harmonic motions. The ion mass is determined from the true cyclotron frequency $\omega_c = qB/m$, which is related to the radial components as [Gabrielse, 2009]:

$$\omega_c = \omega_- + \omega_+. \tag{1.1}$$

It follows that ω_+ and ω_- motions can be converted into each other. This property is utilized in two measurement techniques – a conventional time-of-flight ion cyclotron resonance (TOF–ICR) and a more recent phase-image ion cyclotron resonance (PI–ICR).

In TOF–ICR, the ions start with the slow magnetron motion ω_- which is then converted into the fast modified cyclotron motion ω_+ by applying an RF pulse [Gräff et al., 1980]. The frequency of the pulse is scanned and, when matches ω_c of an ion, a complete conversion is achieved resonantly. Ejected from the trap, the ions are accelerated towards a detector where their time-of-flight (TOF) is recorded. The resonantly excited ones will have the shortest TOF. Mass resolving power R_M of $\sim 10^6$ and a relative uncertainty $\delta m/m$ of high 10^{-8} can be achieved within a measurement time of $\sim$1 second [Huang et al., 2021].

In PI–ICR, ω_- and ω_+ are determined separately by measuring the corresponding phases ions accumulated in the trap after a given time [Eliseev et al., 2013]. The ions start at the center of the trap, and their motion is converted into pure magnetron or modified cyclotron motion by an RF pulse at a corresponding frequency. The accumulated phase is determined from the coordinates of ejected ions on a position-sensitive detector. In comparison to TOF–ICR, this technique offers a significant boost in performance with the highest $R_M > 10^7$, $\delta m/m$ of 10^{-9} and a measurement time of $\sim$0.3–1 seconds [Kaleja et al., 2022].

The strongest point of the method is the unprecedented mass resolving power. The major drawback in TOF–ICR lies in the need to scan the frequencies of excitation pulses which therefore requires $\sim$100 ions to measure TOF–resonance. PI–ICR requires less ions (about 10) but the measurement takes longer because the ions

have to be cooled. This limits the measurement cycle to ∼200 ms. Overall, this limits the reach to short-lived exotic nuclei which are often produced at low rates. In addition, a narrow mass range makes the techniques ineffective for large-scale mapping of mass surface. Both techniques are reviewed in [Dilling et al., 2018].

In an **ion storage ring**, the high-energy ions are confined in magnetic fields created by sets of bending and focusing stages, and circulate in closed orbits. The revolution frequency ν is related to the mass and velocity v as:

$$\frac{\Delta\nu}{\nu} = -\frac{1}{\gamma_t^2}\frac{\Delta(m/q)}{(m/q)} + \left(1 - \frac{\gamma^2}{\gamma_t^2}\right)\frac{\Delta v}{v}, \tag{1.2}$$

where γ is the Lorentz factor, and γ_t is an ion-optical parameter called a transition point. The mass can be unambiguously determined from measured frequency if the velocity term is minimized or canceled. This is achieved in two complimentary techniques – Schottky mass spectrometry (SMS) and isochronous mass spectrometry (IMS).

In SMS, the beam cooling techniques are utilized to minimize the relative velocity spread $\Delta v/v$ [Franzke et al., 1995]. The major disadvantage lies in the duration of the cooling process of few seconds which limits the access to very short-lived nuclei. Typically, R_M of $7.5 \cdot 10^5$ and $\delta m/m$ of low 10^{-7} are achieved. The strong point is a very large mass range – about one hundred nuclides can be measured simultaneously [Litvinov et al., 2005]. Moreover, due to a non-destructive nature of the Schottky-noise frequency measurement [Borer et al., 1974], a single ion can be probed multiple times and yield a mass measurement [Chen et al., 2009].

In IMS, the energy of injected beam is tuned such that $\gamma = \gamma_t$, *i.e.*, the velocity term in Eq. 1.2 is canceled without the need to minimize the velocity spread. Under this condition, the ion-optics of a storage ring is such that ions having the same m/q but different velocities hit the detector at the same time, hence the term "isochronous" [Wollnik, 1987, Hausmann et al., 2000]. The frequency is determined from the measured TOF. The major strength of the technique is that no beam cooling is required, and thus the measurement time of 10–100 μs is possible. However, the mass range is narrow because the isochronicity is strictly realized only for a single m/q value. The methods to relax this limitation are reported in [Geissel et al., 2006, Zhang et al., 2023]. The mass resolving power R_M of $\sim 2 \cdot 10^5$ and $\delta m/m$ of 10^{-7} are typically achieved [Huang et al., 2021]. A recent review of heavy-ion storage rings can be found in [Steck and Litvinov, 2020].

In a **multiple-reflection time-of-flight mass-spectrometer (MR-TOF-MS)**, a low-energy ion bunch is injected in a drift tube (TOF analyzer) where it travels back and forth between two symmetric electrostatic mirrors [Wollnik and Przewloka, 1990]. By tuning the mirrors properly the isochronicity is achieved. The ions of different m/q accelerated by the same effective voltage U_{eff} have different velocity, and thus are separated in TOF t_{TOF} after a distance l:

$$t_{\text{TOF}} = l \cdot \sqrt{\frac{m}{q}} \cdot \sqrt{\frac{1}{2U_{\text{eff}}}}. \tag{1.3}$$

After a desired separation is achieved, the ions are ejected from the analyzer to the TOF detector.

While the Penning trap and the storage ring IMS techniques are either precise or fast, the MR-TOF-MS technique is both at the same time. With a measurement cycle in the order of 10 milliseconds, the resolving power R_M of 10^5 and relative uncertainty $\delta m/m$ of 10^{-7} are achieved routinely [Huang et al., 2021]. The advanced MR-TOF-MS systems *e.g.*, the FRS Ion Catcher at GSI (see Section 2.1.2) and at ZeroDegree spectrometer at RIKEN demonstrated R_M of 10^6 and $\delta m/m$ of low 10^{-8} in under 20 ms [Mardor et al., 2021, Rosenbusch et al., 2023].

The effect of multiple reflections on a mass resolving power R_M can be seen from [Dickel et al., 2015b]:

$$R_M = \frac{(m/q)}{\Delta(m/q)} = \frac{t_{\mathrm{TOF}}}{2\Delta t_{\mathrm{TOF}}} = \\ = \frac{t_{pt} + N \cdot t_a}{2 \cdot \sqrt{(\Delta t_{pt})^2 + (N \cdot \Delta t_a)^2}} = \frac{t_{pt}/N + t_a}{2 \cdot \sqrt{(\Delta t_{pt}/N)^2 + (\Delta t_a)^2}} \quad (1.4)$$

where N is a number of reflections, t_{pt} and Δt_{pt} is the time from injection to detection without any reflections (pass-through) and a corresponding uncertainty, t_a and Δt_a is the time-of-flight for a single turn in the TOF analyzer and a corresponding uncertainty. The uncertainty Δt_{pt} is due to spread in initial conditions of ions prior to injection. It is a dominant contribution to the spread in total TOF in case ions make no reflections ($N = 0$), and limits the R_M in pass-through TOF–MS systems to ∼1000. As ions undergo N turns, the contribution Δt_{pt} becomes N times reduced, and vanishes in the $N \to \infty$ limit. The resolving power R_M becomes limited by Δt_a which is defined by an ion-optical quality of the TOF analyzer. This contribution can be made few orders of magnitude smaller than Δt_{pt}, hence the high resolving power.

In real systems, the number of turns N is of several 100, therefore both contributions (Δt_{pt}) and $(N \cdot \Delta t_a)$ are of similar magnitude. Thus, it is of equal importance to ensure an effective preparation and cooling of ion bunch in a trap system before the injection, a fast and high quality extraction from the trap, and to achieve a high ion-optical quality of the TOF analyzer.

Moreover, the MR-TOF-MS technique is sensitive (less than 10 ions per nuclide are sufficient for a precise mass measurement), non-scanning and has a moderate mass range. Thus it is well-suited for systematic large-scale mass measurements of short-lived exotic nuclei far from β-stability and explorations of long-lived or unknown isomeric states.

Chapter 2

Experiments with the prototype cryogenic stopping cell at GSI

This chapter describes the experiments performed at the FRS Ion Catcher (FRS-IC) setup at GSI Helmholtz Center for Heavy Ion Research (Darmstadt, Germany) within the scope of this thesis. Description of the FRS-IC setup is followed by the description of developments and conditions of the relevant experiments.

2.1 Experimental setup

At GSI Helmholtz Center for Heavy Ion Research (Darmstadt, Germany), a primary beam of stable ions is first produced and accelerated to energies of up to ∼11.4 MeV/u by the universal linear accelerator (UNILAC) [Angert and Schmelzer, 1969]. Next, ions are further accelerated to relativistic energies in heavy-ion synchrotron (SIS-18) [Blasche and Franczak, 1992] up to a magnetic rigidity of 18 Tm which corresponds to energies of about 4.5 GeV/u for $^{1}H^{+}$ and 1 GeV/u for $^{238}U^{73+}$. The relativistic beam is then directed to the Fragment Separator FRS [Geissel et al., 1992] where secondary ion beams of exotic nuclei are produced via in-flight technique (see Section 1.1.2). The isotopes of interest are delivered to the experimental stations downstream *e.g.*, the FRS Ion Catcher [Plaß et al., 2013a, Plaß et al., 2019], the experimental storage ring ESR [Franzke, 1987], the decay spectroscopy DESPEC [Rubio, 2006], the reactions with relativistic radioactive beams $R^{3}B$ [Aumann, 2007].

The following subsections describe in detail the FRS and the FRS Ion Catcher (FRS-IC) shown schematically in Figure 2.1.

2.1.1 The fragment separator FRS

The fragment separator FRS is an in-flight separator and a high-resolution spectrometer. It has two symmetric separation stages. Each stage consists of two 30° dipole magnets for magnetic rigidity analysis, and a set of quadrupole and hexapole magnets for ion focusing and correction of ion-optical aberrations. A profiled aluminum degrader is located at the mid-focal plane between the two separation stages. The slits downstream each stage control the variety of selected ions.

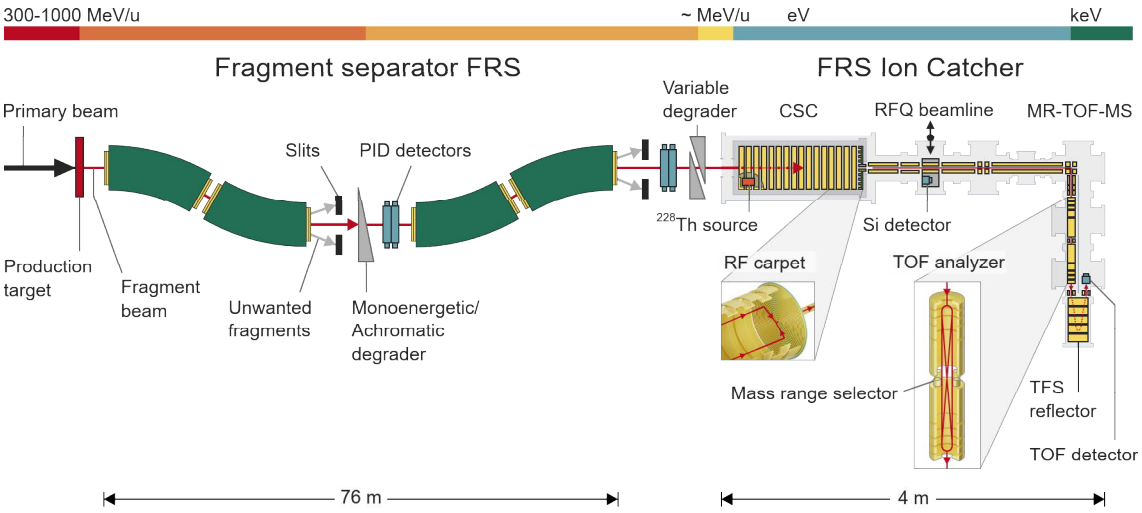

Figure 2.1: Schematic figure of the experimental setup showing the Fragment Separator (FRS) and the FRS Ion Catcher (FRS-IC) at GSI. Please see the corresponding subsections for details.

Ions of exotic nuclei are produced via projectile fragmentation and/or fission reactions between the primary beam and a production target at the energies of 300–1000 MeV/u. Reaction products – fragments – emerge from the target typically fully-stripped and at a velocity of the primary beam. The fragments are separated from the primary beam and other unwanted products using a Bρ-ΔE-Bρ method. At the first magnetic stage, fragments are separated by their magnetic rigidity Bρ. This is equivalent to separating ions according to their mass-over-charge ratio A/Z. Next, the selected ions pass through a wedge-shaped degrader at mid-focal plane where they loose part of their energy. The energy loss is proportional to the atomic number as $\Delta E \propto Z^2$ (see Eq. A.1). As a result, the magnetic rigidity becomes isotope-specific, and therefore the isotope separation is achieved after passing the second magnetic stage. The fragment beams are then sent to the FRS Ion Catcher setup (Section 2.1.2).

By tuning the angle of the wedge-shaped degrader at mid-focal plane, the FRS can be operated in achromatic (standard) mode or monoenergetic modes [Geissel et al., 1989]. The achromatic mode is optimal for the isotopic separation. However, the resulting range straggling of the separated ions is large (Fig. 1.5). In the monoenergetic mode, the degrader is optimized to compress the range straggling of the separated ions. This mode is especially beneficial for the experiments with the prototype cryogenic stopping cell (prototype CSC) at the FRS Ion Catcher – smaller range straggling translates into a larger number of stopped ions of interest. Other operation modes of the FRS are possible *e.g.*, energy-loss spectrometer [Weick et al., 2000], separator-spectrometer [Kostyleva, 2020], and high-resolution and high-transmission modes [Haettner et al., 2020].

A particle identification (PID) detector system of the FRS enables clean and complete isotope identification on event-by-event basis. A secondary electron transmission monitor (SEETRAM) measures the intensity of the primary beam in the target area [Jurado et al., 2002]. It provides information about the spill struc-

ture. A set of plastic scintillators (SCI) measures time-of-flight and intensity of the fragments [Voss et al., 1995]. The time-projection chambers (TPC) measure position and angle of the fragments [Janik et al., 2011]. A combination of SCI and TPC detectors at the middle and final focal planes of the FRS provides information on mass-over-charge ratio A/Z. An information on the atomic number Z is obtained from a multiple sampling ionization chamber (MUSIC) detector by measuring the energy deposition of ions in gas [Pfützner et al., 1994, Stolz et al., 1999]. Recently, the FRS Ion Catcher has been coupled to the PID of the FRS for the first time [Spătaru et al., 2022].

2.1.2 The FRS Ion Catcher

The FRS Ion Catcher (FRS-IC) setup slows down and thermalizes relativistic exotic nuclei to perform high-accuracy direct mass measurements by the means of a multiple-reflection time-of-flight mass spectrometry. The mass measurements with a resolving power of 1 000 000 can be carried out on exotic nuclei ∼50 ms after they are delivered from the FRS. Its world-class performance characteristics provide exceptional opportunities for nuclear structure studies of short-lived exotic nuclei with an uncertainty of down to few keV. Moreover, reaction and decay studies can be performed at the FRS-IC [Miskun et al., 2019, Mardor et al., 2020]. Its results obtained in a series of experiments at GSI contributed to a better understanding of a nuclear structure, *e.g.*, towards the N=Z line in the regions of A=100 [Hornung et al., 2020, Mollaebrahimi et al., 2023] and A=70 [Mardor et al., 2021], in the vicinity of doubly-magic ^{208}Pb [Ayet San Andrés et al., 2019], etc.

Clearly, the FRS-IC is an essential testing ground for a hybrid technique (Section 1.1.3) and future experiments at FAIR.

The following describes the components of the FRS-IC in detail.

Prototype cryogenic stopping cell

The beam of fragments from the FRS is thermalized in a gas-filled cryogenic stopping cell. This stopping cell is a prototype of the cryogenic stopping cell (CSC) for the Super-FRS at FAIR described in Section 4.2. Throughout this thesis, the stopping cell of the FRS-IC is referred to as the "prototype CSC". This is the first stopping cell designed to thermalize ions produced at unprecedented energy of 1000 MeV/u. After a successful commissioning [Purushothaman et al., 2013, Reiter, 2015] the prototype CSC has been employed in a series of experiments at GSI. Numerous technical improvements have been introduced along the way [Miskun, 2019].

In its current state, the prototype CSC demonstrates an areal density of up to 9 mg/cm^2, an extraction efficiency of ∼60% measured online [Plaß et al., 2019], a mean extraction time of about 25 ms, and a rate capability of 10^4 ions/s [Reiter et al., 2016].

The prototype CSC is shown schematically in Figure 2.2. An outer chamber provides thermal insulation vacuum for an inner chamber. The inner chamber is filled with helium buffer gas and is operated at cryogenic temperature of ∼70–

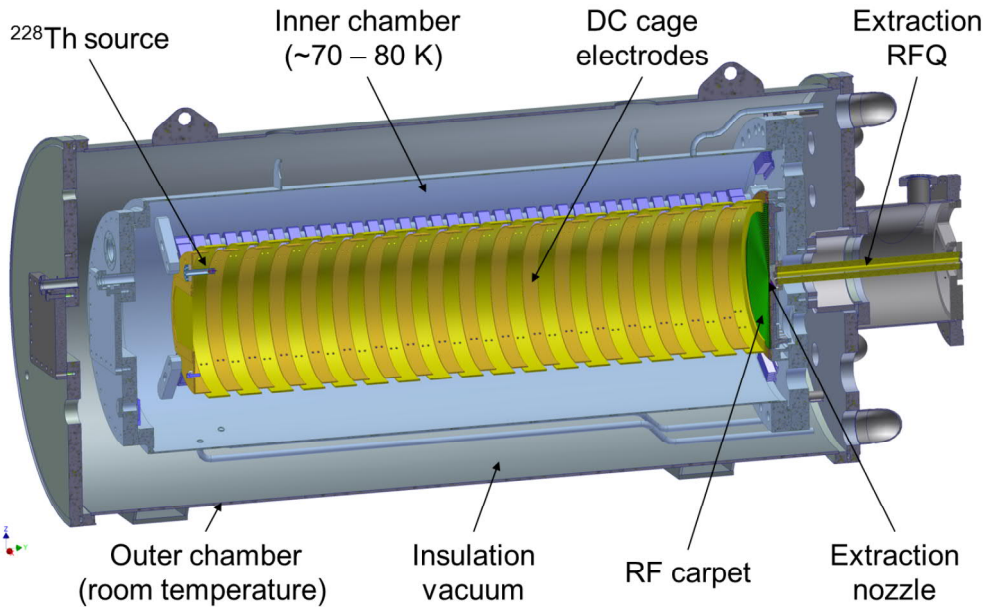

Figure 2.2: Schematic figure of the prototype gas-filled cryogenic stopping cell.

80 K. The chambers are equipped with thin metal foils though which a high-energy beam enters the stopping volume. Ions are thermalized and stopped via collisions with the buffer gas atoms. In order to optimize the range of stopped ions, a variable homogeneous degrader and a MUSIC detector are placed in front of the prototype CSC. Electric fields generated by a DC cage (yellow) and an RF carpet (green) guide the stopped ions towards an extraction nozzle. Once at the nozzle, the ions are extracted by gas flow.

The DC cage consists of 36 overlapping concentric ring electrodes with inner diameters of 25 cm and 26.7 cm. The total length is 105.4 cm. The dimensions of the DC cage define the effective stopping volume. The DC cage accommodates ^{228}Th α-recoil and electric discharge sources for characterization, diagnostics and calibration purposes.

As a part of this thesis, a dedicated DC cage electrode system has been developed and commissioned (see Section 4.1) to enable spontaneous fission studies (offline), and multi-nucleon transfer reaction studies (online). The DC cage generates a DC pushing field that guides ions onto an RF carpet.

The RF carpet is a PCB-based radio-frequency (RF) ion guide (see Fig. 1.7a). It counteracts DC pushing field, and thus repels ions preventing them from hitting the surface. The RF carpet is of a disk shape with a diameter of 25 cm, and has a 5-layer design [Reiter, 2015]. The first layer contains 500 concentric ring electrodes which generate the repulsive RF field. The electrode density is 4 electrodes/mm. Further, there are two inner layers that control field penetration, a layer that accommodates electric component, and a shielding layer behind the extraction nozzle. An additional DC field is superimposed on the electrodes of the first layer, which focuses ions towards the extraction nozzle. The extraction nozzle has a simple cylinder hole geometry with a diameter of 0.6 mm. A potential of the nozzle electrode can be adjusted separately, *e.g.*, in order to optimize ion extraction, block ion extraction or to bunch the ions. The ions extracted through the nozzle

are captured and separated from the gas jet by a radio-frequency quadrupole ion guide called extraction RFQ. The extraction RFQ is the beginning of the radio-frequency quadrupole beamline.

Radio-frequency quadrupole beamline

A radio-frequency quadrupole (RFQ) beamline transports ions extracted from the prototype CSC to a multiple-reflection time-of-flight mass spectrometer (MR-TOF-MS, see next) within a millisecond. It is a multi-purpose RFQ ion-guide system where ions are separated from buffer gas jet, cooled and bunched [Plaß et al., 2007, Haettner et al., 2018]. Moreover, the RFQ beamline is equipped with various means that enable its low-energy beam diagnostic, identification and cleaning capabilities. This includes a pair of mass-filters [Miskun et al., 2015, Hornung et al., 2018], a set of channeltron and silicon surface barrier detectors, and a set of ion sources such as thermal cesium source and a laser ablation carbon cluster ion source (LACCI) [Hornung et al., 2018].

The following use cases illustrate the versatility of the RFQ beamline: (i) a combination of a mass-filter and a channeltron detector was used to study cleanliness of the buffer gas in the prototype CSC [Mollaebrahimi, 2021]; (ii) in an isolation-dissociation-isolation (IDI) technique, a pair of mass filters with a collision-induced dissociation (CID) step in between suppressed molecular contaminants by 4 orders of magnitude [Greiner et al., 2020].

Furthermore, the RFQ beamline provides additional differential pumping stage between the prototype CSC and the MR-TOF-MS. This allows the MR-TOF-MS to operate at low pressure while the prototype CSC operates at its highest areal density.

Multiple-reflection time-of-flight mass spectrometer

After the RFQ beamline, ions enter into the multiple-reflection time-of-flight mass spectrometer (MR-TOF-MS). The MR-TOF-MS is a versatile and powerful tool for precision experiments with exotic nuclei. It is employed at the FRS-IC for (i) ultra-high resolution direct mass measurements, (ii) characterization of the prototype CSC, and (iii) mass tagging for the FRS PID. At FAIR it will be used in experiments of the Super-FRS experiment collaboration, and will deliver isobarically [Plaß et al., 2008a] and even isomerically clean [Dickel et al., 2015a] beams of exotic nuclei to the MATS and LaSpec experiments (Section 4.2.1). Note that the ability to perform isomeric separation in a mass spectrometer of this type has been demonstrated for the first time.

The MR-TOF-MS is explicitly described in [Dickel, 2010, Plaß et al., 2015, Yavor et al., 2015], and its numerous hardware and software improvements are presented in [Ayet San Andrés, 2018, Beck, 2023]. In its present state, the MR-TOF-MS features a high resolving power of 1 000 000 that can be achieved within a short measurement cycle of ∼20 ms and is sensitive to a single ion. This allows studying very exotic nuclei that are short-lived and produced in low quantities. An exemplary case was demonstrated in [Mardor et al., 2021] where a relative accuracy of $\delta m/m = 4 \cdot 10^{-8}$ was achieved in a mass measurement of ^{70}Se

with only 256 events. Such a high accuracy allowed to explore trends in proton-neutron interaction strength in a region of N=Z nuclei. Moreover, the MR-TOF-MS is non-scanning and broadband which makes it very effective for acquisition of data for several ions at the same time and searching for unknown, e.g., new isomeric states. A discovery of an isomeric state in ^{97}Ag for the first time by the means of MR-TOF mass spectrometry is a subject of this thesis (see Section 3.2 and [Hornung et al., 2020]).

The MR-TOF-MS is schematically shown in Figure 2.3. It is coupled to the RFQ beamline via an RFQ ion guide and an RFQ switchyard [Greiner, 2013, Plaß et al., 2015]. The latter mixes ions from the prototype CSC and RFQ beamline with ions from internal sources – electron impact ion source or thermal cesium source – and guides them to an injection trap or various detectors for beam diagnostics. In the injection trap system ions are accumulated, cooled, and bunched. The bunched ions are injected into a time-of-flight (TOF) analyzer. The TOF analyzer is a symmetrical cylindrical electrode system which consists of reflecting mirror electrodes on both ends and a field-free drift region between them. The ion bunch trapped between the two mirror electrodes makes in the analyzer multiple turns, thus achieving separation of the ions by the time of flight in accordance with their mass-over-charge ratio (see Section 1.3). A mass range selector (MRS) in the center of the TOF analyzer selectively narrows the range of transmitted ions to 1 u/e or larger, depending on the specific requirements. This helps to eliminate contaminant ions and/or to disentangle a complex folded TOF spectrum. Next, ions are ejected towards a time-focus shift (TFS) reflector which focuses ions on a detector's plane isochronously *i.e.*, the time-of-flight of ions of the same mass-over-charge ratio is independent of initial spread in kinetic energy and angle. An isochronous secondary electron multiplier (ETP MagneTOF™) detector is primarily used for the mass measurements. Alternatively, a silicon surface barrier detector (Ortec Ultra BU-016-150-100) can be used for decay spectroscopy or beam diagnostics. The detectors can be selected by moving a dedicated motorized sled. A Bradbury–Nielsen gate (BNG) upstream the detectors enables additional post-analyzer TOF separation.

The MR-TOF-MS can be operated in several modes including:

- Time-focus shift (TFS) mode – ions do not undergo any reflections in the TOF analyzer, but fly through. This yields a broad spectrum at the cost of a lower mass resolving power of ∼2000.
- High-resolution mass measurement mode – ions undergo multiple reflections in the TOF analyzer, and are extracted to the TOF detector. As a result, a better ion separation in TOF, and thus, in mass-over-charge is achieved. A mass resolving power of ∼1 000 000 was demonstrated in [Will, 2019] and [Mardor et al., 2021].
- Isobar or isomer separation mode – after a sufficient separation has been achieved in the TOF analyzer, extracted ions pass through the Bradbury–Nielsen gate (BNG). The BNG selectively transmits an isobar or an isomeric state of interest while suppressing the others.

A photograph of the FRS Ion Catcher setup is shown in Figure 2.4.

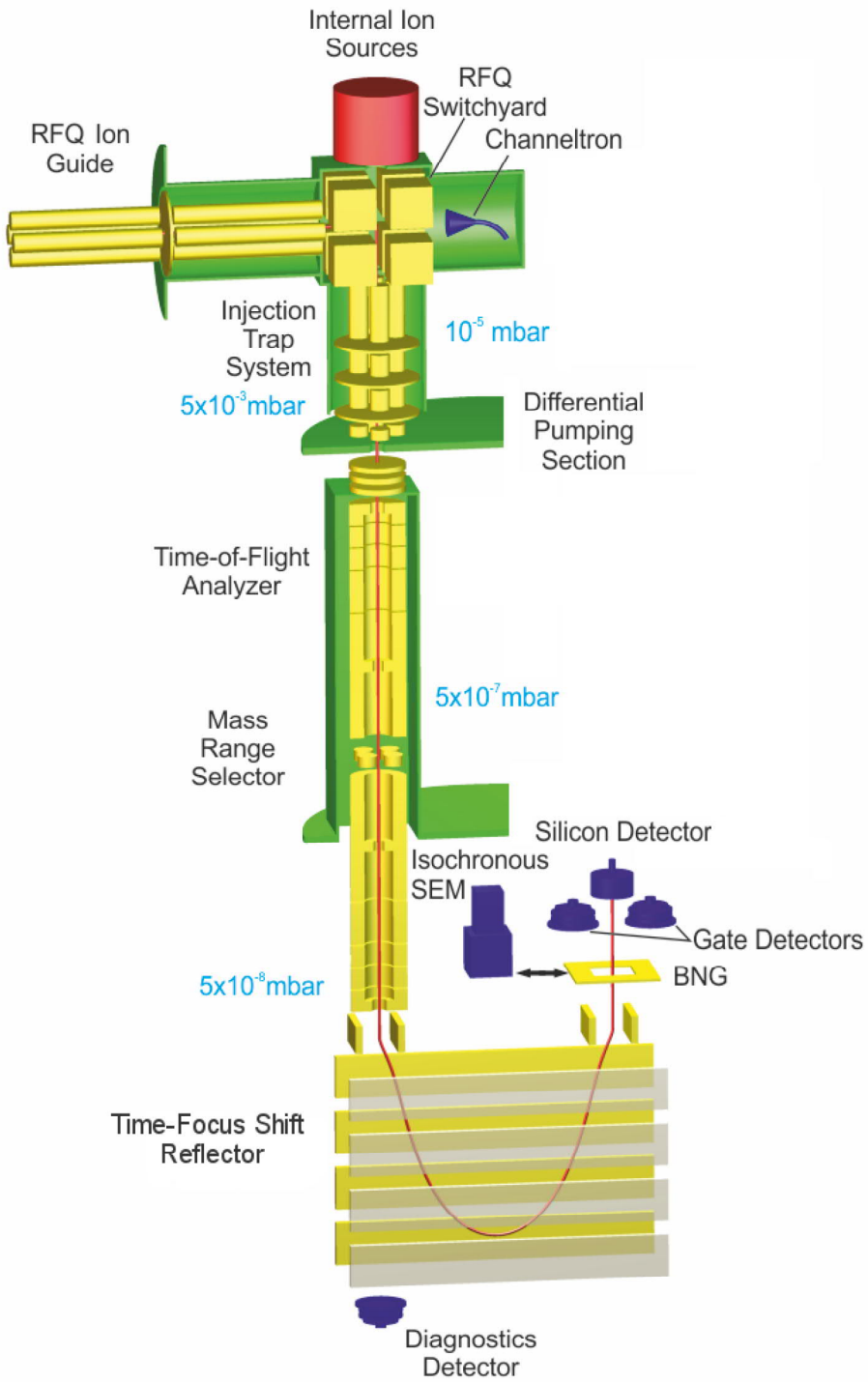

Figure 2.3: Schematic figure of the multiple-reflection time-of-flight mass spectrometer (MR-TOF-MS). Adopted and modified from [Plaß et al., 2013b]

.

2.2 Mean range bunching

As it has been mentioned in Section 2.1.1, experiments which require slowing down ions in the stopping cell benefit from the FRS operated in the monoenergetic

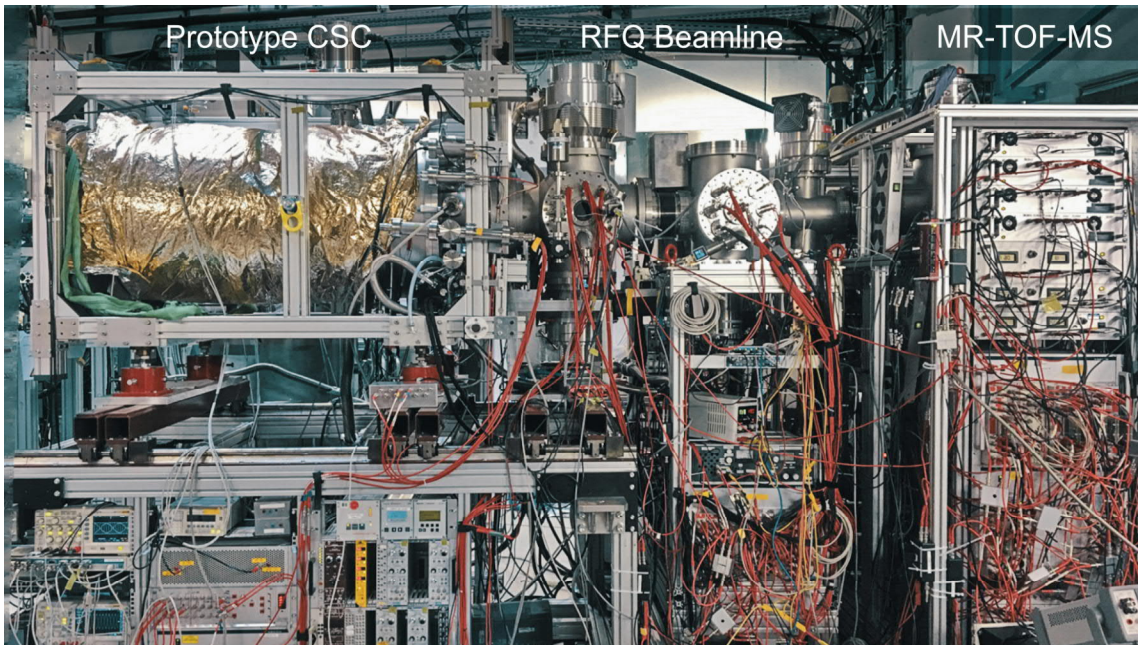

Figure 2.4: A photograph of the FRS Ion Catcher setup.

mode. In this mode, the range straggling of ions of the same nuclide is minimized hence maximizing the number of stopped ions of one species. However, ions of only 1–3 nuclei can be stopped simultaneously since the nuclei are separated in range. This separation in range exceeds the areal density of a stopping cell by two orders of magnitude. Thus, studying larger regions of the nuclide chart is time-consuming and requires a lot of precious beam time. The mean range bunching (MRB) technique has been developed [Dickel et al., 2023] to address this issue.

The MRB setup is schematically shown in Figure 2.5a. When the FRS is operated in achromatic mode, in contrast to the earlier explained monoenergetic mode, the range straggling of ions of the same nuclide is not minimized at the final focal plane (F4). But in the achromatic ion optic, the ions of a particular nuclide are focused on a narrow spot at F4 and thus penetrate through approximately the same amount of matter even when a wedge-shaped degraded is used. In this mode, the range of ions of different nuclides at the F4 linearly depends on their lateral (x) position in the dispersive plane (Fig. 2.5b):

$$\left(\frac{dR}{dx}\right)_i = \text{const}, \tag{2.1}$$

where i indicates that the dependence is material-specific. Passing the beams through an additional wedge-shaped degrader system at F4 (variable angle disk degrader and fixed angle degrader) allows for canceling this dependence. The degrader is oriented, so that nuclei with a larger range penetrate through thicker layers of matter. If the opening angle α of the degrader fulfills the condition:

$$\tan(\alpha) = \frac{1}{\rho_i} \cdot \left(\frac{dR}{dx}\right)_i, \tag{2.2}$$

where ρ_i is a volumetric density of the degrader material, the means of the ranges of all nuclei become aligned and equal to the nuclide at the central optical axis

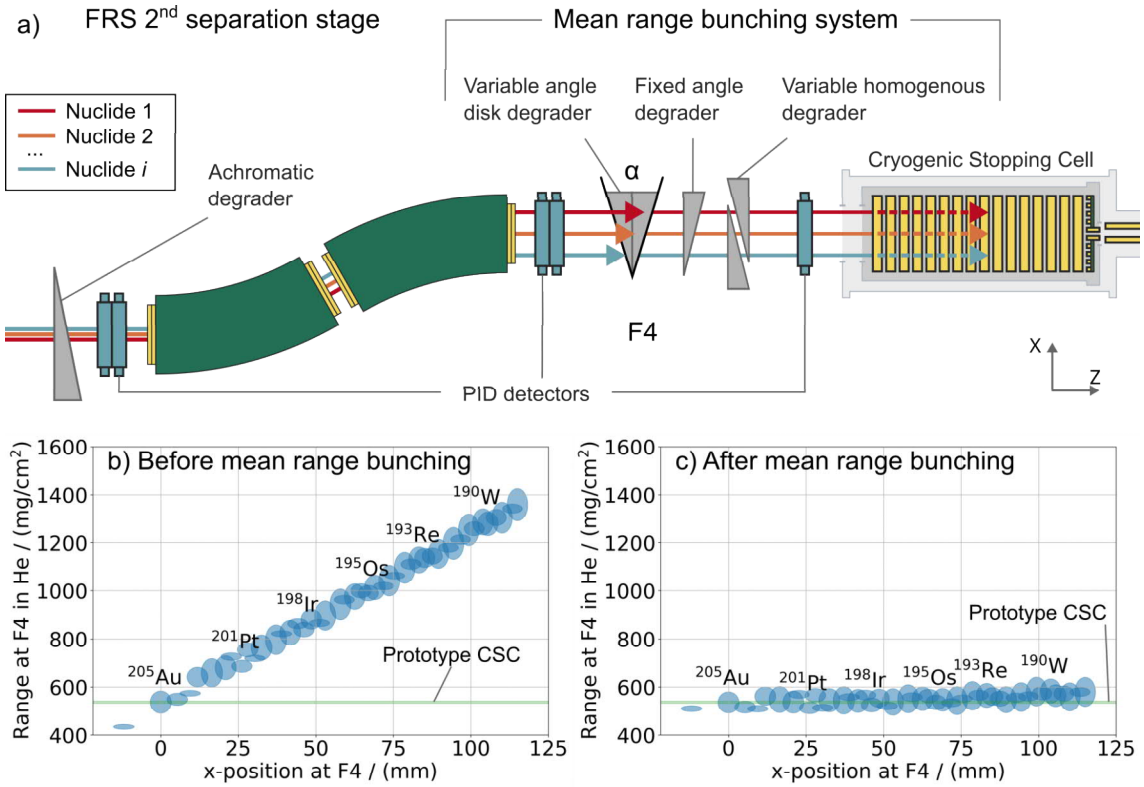

Figure 2.5: Illustration of the mean range bunching (MRB) concept. (a) After separation at the FRS, ions of different nuclides (red, blue) have ranges different than that of the reference nuclide (orange). Passing through a set of MRB degraders with the optimized angle α allows for aligning the range distributions of all nuclides and stopping all simultaneously in the stopping cell. The simulated range distributions before and after the MRB are shown in (b) and (c) correspondingly. The reference nuclide is ^{205}Au. Green rectangle marks the areal density of the prototype CSC. The range axis is offset arbitrarily to illustrate the principle.

$(x = 0)$ (Fig. 2.5c). Next, the variable homogeneous degrader adjusts the mean range and, thus, the stopping position to the goal value. Due to the same mean range of all nuclides, they are now stopped simultaneously, rather than one at a time, in a stopping cell. It is worth noting that the stopping efficiency per individual isotope in the stopping cell is lower than in the standard monoenergetic mode. In the same way, the method is applicable for broadband measurements of stopped cocktail beams *e.g.*, in a thin surface barrier detector.

A degrader system that enables MRB was installed at the final focal plane of the FRS. It has similarities to the system at the mid-focal plane of the FRS [Geissel et al., 1992]. Two wedge-shaped aluminum disks are rotated in opposite directions, and thus the wedge angle α along the x-direction can be adjusted. Two ladders are equipped with aluminum and tantalum homogeneous plates, and a fixed-angle aluminum wedge. The latter allow extending the angle α beyond the limits of the rotating disks. The tantalum plates are used to reduce nuclear reaction losses during the slowdown, compared to lighter-Z stopping materials [Gröf, 2023]. Two wedges form a homogeneous variable degrader.

The MRB has large implications for all experiments with stopped beams at GSI and FAIR as it reduces a required beam time for a large-scale mapping of nuclear properties and searching for the new isotopes and isomeric states. It has been used in online experiments with the FRS-IC since 2020, including the experiment S468 described in this work in Section 2.3.2.

2.3 Experimental conditions and operating parameters

2.3.1 Experiment S411: fragments of Xe beam at 600 MeV/u

The experiment described in this section took place at GSI in a beam time of 2016. It was a part of the S411 experiment. This work presents selected results of mass measurements in a region of $N = Z$ nuclei approaching ^{100}Sn.

The exotic nuclei were produced via projectile fragmentation of a ^{124}Xe primary beam at relativistic energy of 600 MeV/u on a pure Be target with an areal density of 1.622 g/cm^2. The primary beam intensity was $3 \cdot 10^8$ ions per spill with the typical spill length of 0.5 s.

The produced fragments were separated and identified at the FRS via the $B\rho - \Delta E - B\rho$ method and its PID system. The PID was complicated by the fact that at lower energies of the primary beam the fragments were distributed over several charge states.

Given a low energy of the primary beam, the amount of matter in the path of the secondary beam was minimized. At the mid-focal plane, the x- and y-slits were followed by a scintillator detector (SCI) and a degrader system. The latter consisted only from a pair of rotating wedge-shaped disks with an areal density of 737.1 mg/cm^2 on the central axis. The degrader was set to run in the monoenergetic mode. At the final focal plane, a combination of TPC–GEM-TPC [Garcia et al., 2017]/MUSIC–TPC–MUSIC detectors was followed by an x-slit, SCI, a variable homogeneous degrader, and MUSIC as a last detector upstream the prototype CSC.

The prototype CSC was operated at a pressure of 75 mbar and a temperature of 99 K corresponding to an areal density of 3.8 mg/cm^2 which is close to its limit at the time of experiment. Note that certain technical improvements which enabled performance of the FRS-IC described in Section 2.1.2 were not present in 2016.

The mean extraction time of $\sim$200 ms was measured. It was about a factor of 5 larger than expected. The reason was a broken connector related to a DC focusing field along the RF carpet. Nevertheless the increased extraction time had no impact on the results presented in this work.

The RFQ beamline was operated at a pressure of $1.0 \cdot 10^{-2}$ mbar; the IDI technique was employed. The MR-TOF-MS was set to a repetition rate of 50 Hz. The thickness of variable homogeneous degrader was adjusted to stop isotope of interest (IOI) in the CSC. Various calibrant ions were provided by ^{228}Th source (^{224}Ra^{2+}), and electron impact ion source (CxFy$^+$). In addition, ionized impurities of CSC buffer gas (Kr gas) were utilized. The mass range of 1u was selected by the MRS to reduce the background, and was periodically broadened to transport

calibrant ions.

The results of the experiment are discussed in Section 3.2, and have been published in [Hornung et al., 2020].

2.3.2 Experiment S468: fragments of Pb beam at 1050 MeV/u

This section describes conditions of a "Search for new neutron-rich isotopes and exploratory studies in the element range from terbium to rhenium" experiment labeled S468 [Pietri et al., 2018]. The experiment took place at GSI in a beam time of 2020 as a part of the FAIR Phase-0. It was focused on the region along the $N = 126$ line below ^{208}Pb. In the experiment, several detector setups were jointly used to measure nuclear masses, half-lives and production cross sections. The mass measurements were performed at the FRS-IC under the conditions described below.

The exotic nuclei were produced via projectile fragmentation of a ^{208}Pb primary beam at relativistic energy of 1050 MeV/u on a Be target with an areal density of 4.0 g/cm^2 followed by a Nb stripper foil with an areal density of 0.225 g/cm^2. The primary beam intensity was $4 \cdot 10^8$ ions per spill with the typical spill length of 1 s.

The produced fragments were separated and identified at the FRS via the $B\rho - \Delta E - B\rho$ method and its PID system. The FRS was centered on ^{205}Au isotope which corresponds to the magnetic rigidity $B\rho$ of the first and the second stages of 12.5380 Tm and 10.7348 Tm accordingly, and an achromatic Al degrader with an areal density of 2.0 g/cm^2 at the central focal plane. The use of achromatic mode although not typical for experiments with stopped beams was required for the mean range bunching (MRB) technique. The MRB enables stopping of tens of nuclei simultaneously (see Section 2.2) and was experimentally tested for the first time in this beam time.

At the mid-focal plane of the FRS, the degrader system was followed by a scintillator detector (SCI) and a set of two TPC. At the final focal plane, a combination of TPC–MUSIC–MUSIC–TPC detectors was followed by x- and y-slits, SCI, homogeneous Al degrader, SCI, the FRS-IC degrader system, an active stopper [Kumar et al., 2009], SCI, and MUSIC as a last detector upstream the prototype CSC.

The prototype CSC was operated at a pressure of 75 mbar and a temperature of 85 K corresponding to an areal density of 4.2 mg/cm^2. The mean extraction time of 70±40 ms was measured. The areal density and the ion extraction time were limited due to technical issues with the RF carpet. The RFQ beamline was operated at a pressure of $1.2 \cdot 10^{-2}$ mbar; the IDI technique was employed. The MR-TOF-MS was set to a repetition rate of 25 Hz.

The results of the experiment are discussed in Section 3.3.

Chapter 3

Data analysis and results of the experiments

3.1 Data analysis procedure

The analysis of the data collected during the experiments presented in Sections 2.3.1 and 2.3.2 is based on a procedure extensively described in [Ebert, 2016, Ayet San Andrés, 2018, Ayet San Andrés et al., 2019]. This procedure has been developed to achieve the highest accuracy possible when the measured spectra are complicated by overlapping peaks with very low number of events. The major steps of the procedure are schematically shown in Figure 3.1 and include the following:

1. A time-of-flight (TOF) spectrum recorded by the MR-TOF-MS data acquisition system is converted into a mass-over-charge spectrum according to:

$$\frac{m}{q} = \frac{c \cdot (t_{\mathrm{exp}} - t_0)^2}{(1 + IT \cdot b)^2}, \tag{3.1}$$

   where t_{exp} is a measured TOF, IT is a number of isochronous turns in the analyzer, t_0, c and b are the calibration parameters. The calibration is performed using abundant calibrant ions with a well-known mass.

   Long-term measurements are subject of TOF drifts caused by fluctuations of the power supplies voltages and of the analyzer dimensions induced by temperature. In order to correct for these drifts, the value of b is adjusted in time in a so-called time-resolved calibration (TRC) step.

   The steps described above are performed using TofControl software [Bergmann, 2023]. The calibrated mass-over-charge spectrum is exported as unbinned data for further processing.

2. A peak shape is determined from a high-statistics calibrant ion, measured simultaneously with IOI. It is fitted with a hyper-EMG function [Purushothaman et al., 2017], *i.e.*, a Gaussian distribution convoluted with multiple exponential functions with different weights at one or both sides. For this, the data is binned according to Freedman-Diaconis rule [Freedman and Diaconis, 1981] and fitted by a least squares (LS)

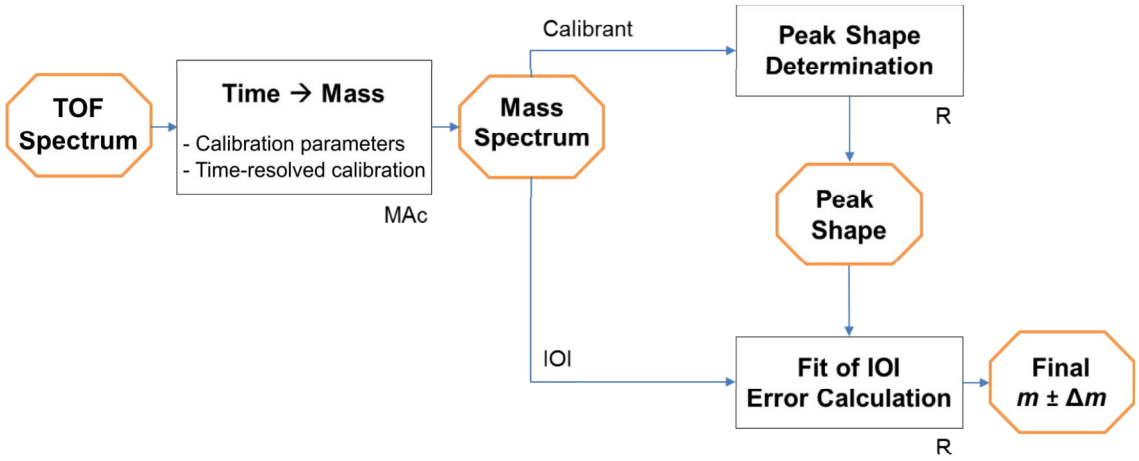

Figure 3.1: Schematic overview of the major steps of the data analysis procedure.

method. The goodness of the fit is validated in a reduced χ^2 test and a Kolmogorov–Smirnov (KS) test [Massey Jr, 1951]. Once the parameters of the hyper-EMG are determined, the calibrant data is fitted by a weighted maximum likelihood estimation (wMLE) method [Hu and Zidek, 2002], where the only free parameter is a peak centroid. This step is required in order to unify fitting methods used in treatment of calibrant ion and IOI data. Compared to the LS method, the wMLE is more robust in treatment of low-statistics data. Furthermore, it does not require data binning, and thus avoids associated errors. The weighting by truncated logarithm of the hyper-EMG function itself is performed in order to minimize the influence of the outliers [Ebert, 2016].

3. In TOF mass spectrometry it is known that all ions with the same charge state have the same peak shape. Therefore, the peak shape parameters determined at the previous step with calibrant ion can be scaled and fitted to the IOI. The wMLE method is used for that. The resulting fits for calibrant ion and IOI alike are corrected for the effects caused by the operation of MRS (see Section 2.1.2) and relativistic effects. In case of fitting overlapping peaks, a so-called bias correction has to be applied in addition.

   Finally, a precision calibration is performed to re-establish the mass-over-charge scale after the wMLE fitting.

4. The uncertainty of the mass value is calculated by adding in quadrature individual components. The components relevant for this work are the statistical uncertainties of IOI and calibrant ions, the uncertainty due to operation of MRS, the uncertainty due to unknown unresolved peak (contaminant), and the peak-shape uncertainty.

   Uncertainty due to operation of MRS: the MRS (Sec. 2.1.2) is switched on with proper timing *e.g.*, to eliminate contaminant ions. Each switching causes a small change in the applied voltages, and thus shifts the TOF of the transmitted ions. This shift is corrected for IOI and calibrants in all mass measurements based on a characterization measurement performed

with reference ions. The corresponding uncertainty is assumed to be 50% of this correction.

Uncertainty due to unknown unresolved peak (contaminant): the peak of IOI might contain events from contaminant ions. To estimate their influence on $(m/q)_{\mathrm{IOI}}$, a synthetic data is generated containing two peaks which represent IOI and potential contaminant. The contaminant peak is moved over the IOI peak, and for each position a shift in $(m/q)_{\mathrm{IOI}}$ is calculated with a respective KS test. The corresponding uncertainty is defined as the strongest shift multiplied by the result of the respective KS test. Note that this procedure has been changed after 2020, and therefore is only relevant for presented in Sec. 3.2. The new procedure is described in [Kripko-Koncz, 2023]. It is omitted here because the corresponding uncertainty is insignificant in the results of Sec. 3.3.

The peak-shape uncertainty: each parameter of the Hyper-EMG function is altered by its individual uncertainty while keeping the others constant, and the peak is fitted again with the wMLE method. A deviation in the obtained m/q is calculated for the peak-shape calibrant and the IOI. The deviations calculated for all parameters are added in quadrature to obtain the peak-shape uncertainty.

A comprehensive list of uncertainty components and their definitions can be found in [Ayet San Andrés et al., 2019].

5. The final atomic mass value of IOI m_{IOI} and its uncertainty σ_{IOI} are obtained as:

$$m_{\mathrm{IOI}} = \left(\frac{m}{q}\right)_{\mathrm{IOI}} \cdot q_{\mathrm{IOI}} + m_e \cdot \frac{q_{\mathrm{IOI}}}{e} \tag{3.2}$$

$$\sigma_{\mathrm{IOI}} = \sigma_{\mathrm{IOI,ionic}} \cdot q_{\mathrm{IOI}}, \tag{3.3}$$

where $(m/q)_{\mathrm{IOI}}$ and σ_{IOI} are the mass-over-charge and uncertainty values obtained in the analysis above, q_{IOI}/e is a charge state of IOI, and m_e is a mass of electron. The measurement is usually performed with singly- or doubly-charged ions, therefore the electron binding energy of few eV can be neglected.

Isomer excitation energy is calculated as a difference between masses of corresponding states. Its uncertainty does not consider components that influence both states in the same way. The considered components are statistical uncertainties, peak-shape uncertainties, bias correction and uncertainty due to contamination.

Steps 2–5 are implemented in R programming language [R Core Team, 2021]. It should be noted that the steps above provide a general description of the mass-fitting procedure. The exact analysis procedure always depends on the case and is adapted accordingly. The details of the data analysis of the experiments presented in this thesis are given in the corresponding sections below.

3.2 Results on nuclei near N=Z line approaching ^{100}Sn

This section presents details of data analysis and discussion of the results of the S411 experiment (Section 2.3.1).

3.2.1 Data analysis

The analysis of data was performed according to procedure described in Section 3.1 and [Ayet San Andrés et al., 2019]. In Eq.3.1, t_0 of (201 ± 11) ns was determined offline. The peak shape of an IOI was best described with the Hyper-EMG with one exponential tail on each side unless stated otherwise. Detailed information is presented below.

Two independent analyzes of the same data were carried out, and are referred to in this section as (I) and (II) unless stated otherwise. The analysis (I) was conducted with a focus on the calibration and peak identification stages. The analysis (II) focuses on optimizing the peak fitting parameters. The mass values and uncertainties of two analyzes were combined as described in [Ayet San Andrés et al., 2019]. Mass values were weighted by their uncertainties. The uncertainties were divided into dependent and independent components. Weighted mean was used to combine dependent components; variance of the weighted mean – to combine independent components. The combined dependent components and combined independent components were added in quadrature to obtain total uncertainty. The results can be found in Tables 3.1 and 3.2, and in Figure 3.5.

The mass and isomer excitation energy of ^{109}In^{g,m,n}

Ions of ^{109}In^{g,m,n} performed 580 IT with a total TOF of about 18.8 ms. Calibration parameters b and c were determined with ions ^{224}Ra^{2+} and ^{82,83,86}Kr^{+}. In addition, in (I) ions ^{84}Kr^{+} were utilized. TRC and peak shape were obtained with IOI. Precision calibration was performed with ions ^{84}Kr^{+} in (I), and ^{224}Ra^{2+} in (II). Results of fitting the data are shown in Fig. 3.3d and 3.3e.

The mass excess value of ^{109}In is in agreement with the AME2016 within 1.0σ *i.e.*, (−32 ± 34) keV/c^2. For the ground state, total relative uncertainty of $3.4 \cdot 10^{-7}$ which corresponds to 34 keV/c^2 is dominated by uncertainty due to operation of the MRS (see Table 3.1). FWHM of 242 keV/c^2 renders mass resolving power of 420 000.

The ground and two isomeric states were measured. Their spin-parity J^π is $9/2^+$, $1/2^-$ and $(19/2^+)$ according to NUBASE2016 [Audi et al., 2017]. For the $1/2^-$ isomeric state, the excitation energy E_x of (651 ± 27) keV/c^2 was obtained. Its uncertainty is dominated by the uncertainty due to unknown unresolved peak *i.e.*, contaminant. Isomer-to-ground ratio of 0.042 ± 0.004 with total number of counts of 2281 was determined. For the $(19/2^+)$ isomeric state, E_x of (2098 ± 11) keV/c^2 was obtained. Its uncertainty is dominated by the uncertainty due to contaminant. Isomer-to-ground ratio of 0.19 ± 0.01 with total number of counts of 2605 was determined (see Table 3.2).

The mass and isomer excitation energy of ^{107}In^{g,m}

Ions of ^{107}In^{g,m} performed 590 IT with a total TOF of about 18.9 ms. In (I) and (II), ions $C_2F_4^+$, $C_3F_3^+$, $C_2F_5^+$ and $^{86}Kr^+$ were used to determine b and c. Additionally, ions $^{12}C^{13}CF_4^+$ were used in (I) and $^{82,83,86}KrN^+$ in (II). TRC and precision calibration were performed with ions $C_2F_4^+$. Peak shape was obtained with IOI. Hyper-EMG with two exponential tails on the left and one tail on the right was found to describe the data best. Results of fitting the data are shown in Fig. 3.3c.

The mass excess value of ^{107}In is in agreement with the AME2016 within 0.7σ *i.e.*, (-19 ± 29) keV/c^2. Total relative uncertainty of $2.7 \cdot 10^{-7}$ which corresponds to 27 keV/c^2 is dominated by uncertainty due to operation of the MRS (see Table 3.1). FWHM of 257 keV/c^2 renders mass resolving power of 390 000.

For ^{107}In^m, the isomer excitation energy E_x of (663 ± 22) keV/c^2 was determined. Its uncertainty is dominated by the uncertainty of peak shape. Isomer-to-ground ratio of 0.025 ± 0.001 with total number of counts of 17458 was determined (see Table 3.2). The spin-parity J^π of ground and isomeric states were taken from NUBASE2016 [Audi et al., 2017] as $9/2^+$ and $1/2^-$ accordingly.

The mass and isomer excitation energy of ^{105}In^{g,m}

Ions of ^{105}In^{g,m} performed 590 IT with a total TOF of about 18.7 ms. Ions $C_2F_4^+$, $C_2F_5^+$, $^{83,84,86}Kr^+$ in (I), and $^{83,86}Kr^+$ in (II) were used to determine b and c. To perform TRC and determine peak shape, ions of $^{105}In^+$ *i.e.*, the isotope of interest (IOI) were used. Calibrant ions for precision calibration were $^{86}Kr^+$ in (I) and $C_2F_5^+$ in (II). Results of fitting the data are shown in Fig. 3.3b.

The mass excess value of ^{105}In is in agreement with the AME2016 within 1.1σ *i.e.*, (-36 ± 33) keV/c^2. For the ground state, total relative uncertainty of $3.2 \cdot 10^{-7}$ which corresponds to 31 keV/c^2 is dominated by uncertainty due to operation of the MRS (see Table 3.1). FWHM of 216 keV/c^2 renders mass resolving power of 450 000.

For ^{105}In^m, the isomer excitation energy E_x of (702 ± 27) keV/c^2 was determined. Its uncertainty is dominated by the uncertainty due to unknown unresolved peak *i.e.*, contaminant. Isomer-to-ground ratio of 0.02 ± 0.01 with total number of counts of 891 was determined (see Table 3.2). The spin-parity J^π of ground and isomeric states were taken from NUBASE2016 [Audi et al., 2017], as $9/2^+$ and $(1/2^-)$ accordingly.

The mass and isomer excitation energy of ^{103}In^{g,m}

Ions of ^{103}In^{g,m} performed 600 IT with a total TOF of about 18.9 ms. Calibration parameters b and c were determined with ions $C_2F_4^+$, $^{12}C^{13}CF_4^+$, $C_3F_3^+$, $C_2F_5^+$, $^{86}Kr^+$. In (II), ions $C_2OF_3^+$ were used in addition. TRC was performed with $C_2F_4^+$ in (I) and $C_2F_5^+$ in (II). Calibrant ions for peak shape determination and precision calibration were $C_2F_5^+$ in (I) and $^{12}C^{13}CF_4^+$ in (II). Results of fitting the data are shown in Fig. 3.3a.

The mass excess value of ^{103}In is in agreement with the AME2016 within 0.1σ *i.e.*, (2 ± 27) keV/c^2. Total relative uncertainty of $2.7 \cdot 10^{-7}$ which corresponds to

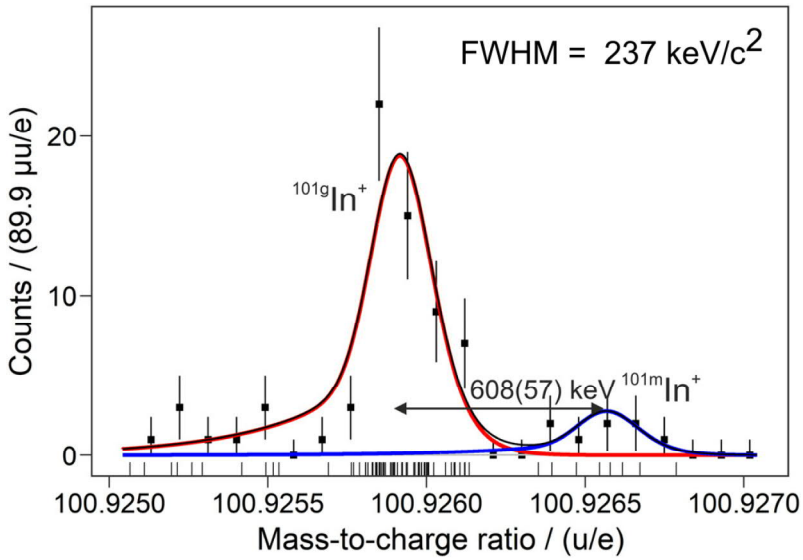

Figure 3.2: Measured mass-over-charge spectrum of ^{101}In nuclide. Square points represent the histogram of unbinned data which is shown as a rug plot below the histogram. Fits to unbinned data of ground and isomeric states are shown as red and blue curves correspondingly. The sum of the fits is shown as black curve. Isomer excitation energy of 608(57) keV was measured. A FWHM of 237 keV/c^2 renders mass resolving power of 400 000. Adopted and modified from [Hornung et al., 2020].

25 keV/c^2 is dominated by uncertainty due to operation of the MRS (see Table 3.1). FWHM of 190 keV/c^2 renders mass resolving power of 500 000.

For ^{103}In^m, the isomer excitation energy E_x of (689 ± 77) keV/c^2 was determined. Its uncertainty is dominated by the uncertainty due to unknown unresolved peak *i.e.*, contaminant. The spin-parity J^π of ground and isomeric states were taken from NUBASE2016 [Audi et al., 2017], where they are estimated to be $(9/2^+)$ and $(1/2^-)$ accordingly. Isomer-to-ground ratio of 0.03 ± 0.01 with total number of counts of 929 was determined (see Table 3.2).

The mass and isomer excitation energy of ^{101}In^{g,m}

Ions of ^{101}In^{g,m} performed 600 IT with a total TOF of about 18.7 ms. The TRC, peak shape and final mass value were obtained with an isobaric calibrant ion ^{12}C^{13}CF$_4$$^+$ in (I) and (II). Isobaric calibration reduces the total uncertainty because the error of c and components associated with non-perfect injection, operation of the MRS (see Section 2.1.2) and ion phase-space are neglected. Results of fitting the data are shown in Figure 3.2. A full width at half maximum (FWHM) of 237 keV/c^2 renders mass resolving power of 400 000. For the ground state, total relative uncertainty of $2.1 \cdot 10^{-7}$ which corresponds to 20 keV/c^2 is dominated by statistical uncertainty.

At the time of experiment, relevant version of atomic mass evaluation was AME2016 [Wang et al., 2017]. Mass value and uncertainty of ^{101}In in AME2016 were based on extrapolation of mass surface. The mass excess of ^{101}In presented

in this work is in agreement with the AME2016 extrapolation within 0.4σ which corresponds to (75 ± 201) keV/c^2 (see Table 3.1).

For ^{101}In^m, the isomer excitation energy of (608 ± 57) keV/c^2 was measured. The uncertainty was dominated by statistical component. The isomer-to-ground ratio of 0.14 ± 0.03 with total number of counts of 70 was determined (see Table 3.2). The spin-parity J^π of ground and isomeric states were taken from NUBASE2016 [Audi et al., 2017], where they are estimated to be $(9/2^+)$ and $(1/2^-)$ accordingly.

Masses of ground and isomeric states of ^{101}In presented in this work and in [Hornung et al., 2020] confirms the mass measurement performed at the Cooler Storage Ring (CSR) accelerator complex of the Heavy Ion Research Facility in Lanzhou [Xu et al., 2019]. The weighted average of both results is recommended by the recent atomic mass evaluation AME2020 [Wang et al., 2021]. Recent measurement performed at the ISOLTRAP at CERN [Mougeot et al., 2021] agrees with both previous results.

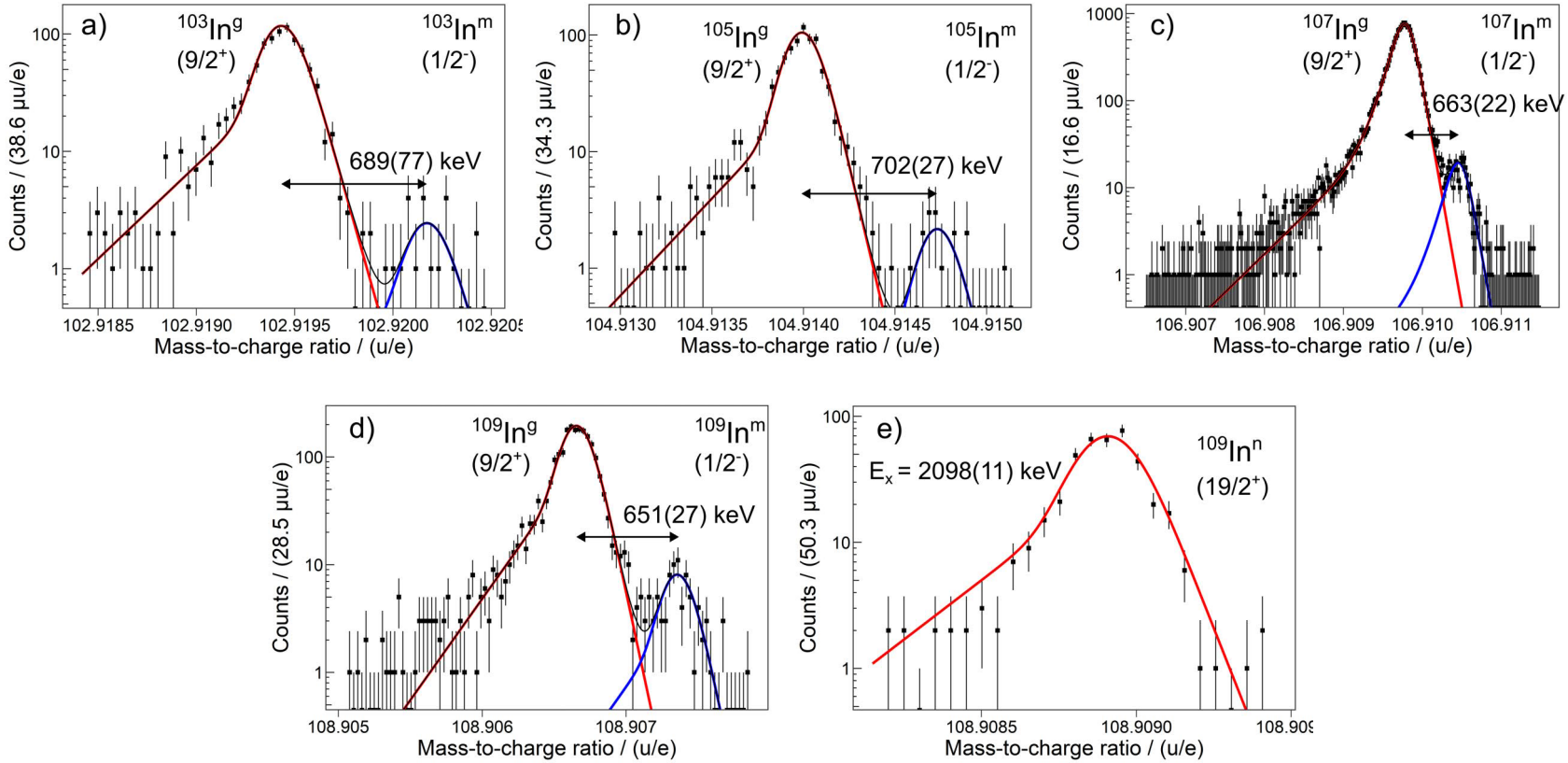

Figure 3.3: Measured mass-over-charge spectra of odd-A isotopes of $^{103-109}$In. In (a)–(d), fits to unbinned data of $(9/2^{+})$ ground and $(1/2^{-})$ isomeric states are shown as red and blue curves correspondingly. Black curve shows the sum of the fits. In (e), single-peak fit is shown as a red curve. Square points represent the histogram of unbinned data (not shown). Isomer excitation energies are shown. Mass resolving power of up to 500 000 has been achieved. Please see text for details.

The mass and isomer excitation energy of ^{97}Ag^{g,m}

This work presents an independent analysis of ^{97}Au^{g,m} data. Details of the previous analysis can be found in [Hornung, 2018]. Result of the two analyzes were combined and published in [Hornung et al., 2020].

Two sets of measurements were performed under different conditions in order to unambiguously identify ^{97}Ag isotope: (a) three measurements at different thickness of variable homogeneous degrader upstream the prototype CSC; (b) one measurement at different IT in the MR-TOF-MS.

In (a), ions of IOI performed 612 IT with a total TOF of about 18.7 ms. TRC was performed with ions $C_2F_4^+$. Ions of isobaric calibrant $C_2OF_3^+$ were used to obtain peak shape and precision calibration. In (b), ions of IOI performed 613 IT with a total TOF of ∼18.7 ms. Calibration parameters b and c were obtained with ions $C_2F_4^+$, $^{84}KrO^+$, $^{96}Pd^+$. TRC, peak shape and precision calibration were obtained with ions $C_2F_4^+$. Results of fitting the data are shown in Fig. 3.4.

The final mass value and total uncertainty were obtained as a weighted mean of averaged results of data sets (a) and (b), and are shown in Table 3.1. The mass excess value of ^{97}Ag is in agreement with the AME2016 within 0.7σ *i.e.*, (-76 ± 111) keV/c^2. The AME2016 recommended mass value that was measured indirectly by γ-spectroscopy [Hu et al., 1999]. Therefore the mass of ^{97}Ag presented in this work has been measured directly for the first time. The uncertainty was reduced by an order of magnitude. FWHM of 199 keV/c^2 renders mass resolving power of 450 000.

Remarkably, for ^{97}Ag^m this is the first discovery of a nuclear isomeric state by the means of multiple-reflection time-of-flight mass spectrometry. The isomer excitation energy E_x of (601 ± 47) keV/c^2 was determined. Its uncertainty is dominated by the uncertainty due to contaminant. In NUBASE2016 [Audi et al., 2017], the ground and isomeric states are assigned to J^π of $(9/2^+)$ and $(1/2^-)$ correspondingly. The half-life of the $(1/2^-)$ isomeric state of 100 ms is predicted [Kondev et al., 2021]. This is in agreement with our expectations because the isomeric state survived the extraction from the stopping cell and transport to the MR-TOF-MS of approx. 200 ms. Therefore for the measured isomer-to-ground-state ratio only a lower limit of 0.08 ± 0.03 can be given with the total of 306 events (Tab. 3.2).

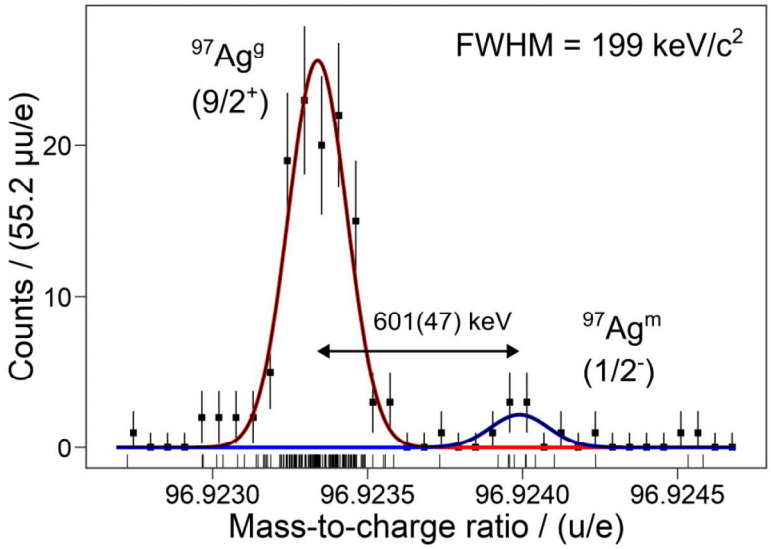

Figure 3.4: Measured mass-over-charge spectrum of ^{97}Ag^{g,m} nuclide. Square points represent the histogram of unbinned data which is shown as a rug plot below the histogram. Fits to the unbinned data of $(9/2^{+})$ ground and $(1/2^{-})$ isomeric states are shown as red and blue curves correspondingly. Black curve shows the sum of all fits. Isomer excitation energy of 601(47) keV was measured. A FWHM of 199 keV/c^2 renders mass resolving power of 450 000. Please see text for details.

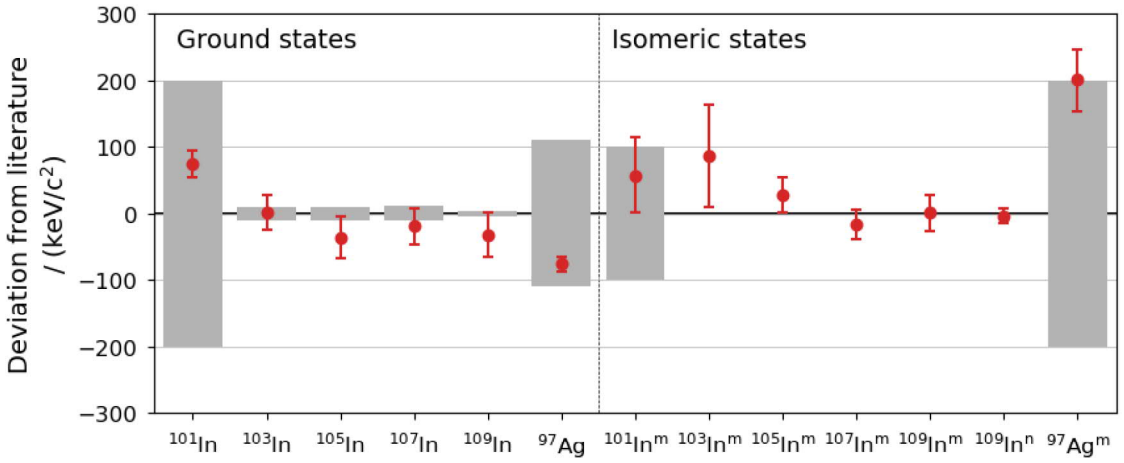

Figure 3.5: Deviation of masses and isomer excitation energies of odd-A $^{101-109}$In^{g,m} isotopes and ^{97}Ag^{g,m} nuclide presented in this work (see Tables 3.1 and 3.2) from literature values taken from atomic mass evaluation 2016 (AME2016) [Wang et al., 2017]. The error bars represent total experimental uncertainty. The gray band around the horizontal axis represents the AME2016 uncertainty.

Table 3.1: Mass excess and uncertainty of odd-A $^{101-109}$In isotopes and ^{97}Ag nuclide measured at the FRS-IC. The results of two independent analyzes labeled as (I) and (II) are combined according to [Ayet San Andrés et al., 2019]. The uncertainties of the measured values are the total experimental uncertainties. The measured mass excess values are compared with the literature values from AME2016 [Wang et al., 2017].

Nuclide	Calibrant (Analysis)	$ME_{FRS\text{-}IC}$ /(keV/c^2)	$ME_{AME2016}$ /(keV/c^2)	$ME_{FRS\text{-}IC} - ME_{AME2016}$ /(keV/c^2)
^{101}In	$^{12}C^{13}CF_4$	−68 535 ± 20	−68 610 ± 200#	75 ± 201
^{103}In	C_2F_5 (I); $^{12}C^{13}CF_4$ (II)	−74 631 ± 25	−74 633 ± 10	2 ± 27
^{105}In	^{86}Kr (I); C_2F_5 (II)	−79 677 ± 31	−79 641 ± 10	−36 ± 33
^{107}In	C_2F_4	−83 583 ± 27	−83 564 ± 11	−19 ± 29
^{109}In	^{84}Kr (I); ^{224}Ra (II)	−86 522 ± 34	−86 490 ± 4	−32 ± 34
^{97}Ag	C_2OF_3	−70 906 ± 11	−70 830 ± 110	−76 ± 111

value and uncertainty derived not from experimental data, but based on trends from the mass surface.

Table 3.2: Isomer excitation energy E_x and isomer-to-ground ratios of odd-A $^{101-109}$In and ^{97}Ag nuclei measured at the FRS-IC. The uncertainties of the measured values are the total experimental uncertainties. The measured E_x are compared with the literature values taken from [Jain et al., 2015].

Isomer	Half-life	J^π	$E_{x,\,\text{FRS-IC}}$ /(keV/c^2)	$E_{x,\,\text{lit}}$ /(keV/c^2)	$E_{x,\,\text{FRS-IC}} - E_{x,\,\text{lit}}$ /(keV/c^2)	Isomer-to-ground-state ratio
^{101}In^m	10 s#	$(1/2^-)$	608 ± 57	550 ± 100#	58 ± 115	0.14 ± 0.03
^{103}In^m	(34 ± 2) s	$(1/2^-)$	689 ± 77	631.7 ± 0.1	57 ± 77	0.03 ± 0.01
^{105}In^m	(48 ± 6) s	$(1/2^-)$	702 ± 27	674.08 ± 0.25	28 ± 27	0.02 ± 0.01
^{107}In^m	(50.4 ± 0.6) s	$(1/2^-)$	663 ± 22	678.5 ± 0.3	−16 ± 22	0.025 ± 0.001
^{109}In^m	(1.34 ± 0.07) m	$(1/2^-)$	651 ± 27	650.1 ± 0.3	1 ± 27	0.042 ± 0.004
^{109}In^n	(209 ± 6) ms	$(19/2^+)$	2098 ± 11	2101.8 ± 0.2	−4 ± 11	0.19 ± 0.01
^{97}Ag^m	100 ms#	$(1/2^-)$	601 ± 47	400 ± 200#	201 ± 205	0.08 ± 0.03*

value and uncertainty derived not from experimental data, but based on trends.
* only a lower limit could be derived.

3.2.2 Probing the sharp cutoff model of isomer population

The detected abundances of ground and isomeric states reflect the processes of angular momentum population in the reaction. The measured isomer-to-ground-state ratios of $1/2^-$ isomeric states of odd-A isotopes of $^{101-109}$In were compared to the theoretical predictions. The systematics for five isotopes with the same spin assignment in ground and isomeric states and very similar isomer excitation energy present an ideal test case to see if the details of the nuclear structure of these nuclei are relevant.

An isomeric ratio is defined as a probability that in the reaction a nucleus is produced in an isomeric state, relative to the total production of that nucleus. The isomeric ratios were estimated using the sharp cutoff model (SCM) of projectile fragmentation reaction [de Jong et al., 1997]. According to the SCM, the theoretical isomeric ratio R_{theor} can be obtained by integrating the total angular momentum distribution of the fragments P_J from the total angular momentum of the isomer J_m up to infinity:

$$R_{\mathrm{theor}} = \int_{J_m}^{\infty} P_J dJ. \tag{3.4}$$

The analytical form of P_J is based on the statistical abrasion-ablation model [Gaimard and Schmidt, 1991], and can be expressed as:

$$P_J = \frac{2J+1}{2\sigma_f^2} \exp\left(-\frac{J(J+1)}{2\sigma_f^2}\right). \tag{3.5}$$

The width of the distribution σ_f, also called the spin-cutoff parameter of the final fragment, is given by:

$$\sigma_f^2 = \left\langle j_z^2 \right\rangle \frac{(A_p - A_f)(\nu A_p + A_f)}{(\nu+1)^2(A_p - 1)}, \tag{3.6}$$

where A_p and A_f are the mass numbers of projectile and fragment accordingly, $\langle j_z^2 \rangle$ is the average square of the angular momentum projection calculated as:

$$\left\langle j_z^2 \right\rangle = 0.16 A_p^{2/3} \big(1 - (2/3)\beta_2\big), \tag{3.7}$$

with β_2 being the quadrupole deformation parameter of the fragmented nucleus. In the vicinity of the doubly magic ^{100}Sn negligible deformations are expected, therefore $\beta_2 = 0$ can be assumed.

In Eq. 3.6, the parameter ν is the mean number of ablated nucleon per abrasion of one nucleon. Its value depends on the projectile nuclei and the primary beam energy. In [Gladnishki et al., 2004], $\nu = 2$ was assumed for ^{238}U beam at 750 MeV/u; in [Park et al., 2019], $\nu = 1$ was assumed for ^{124}Xe beam at 345 MeV/u. In this work, a ^{124}Xe beam at 600 MeV/u was used, therefore an intermediate value of $\nu = 1.5$ was considered. The calculations for $\nu = 1$ and $\nu = 2$ have been performed as well.

The extreme simplifying assumption of the SCM is that all states with $J > J_m$, and only those, decay to the isomer of interest. In this work, the total angular

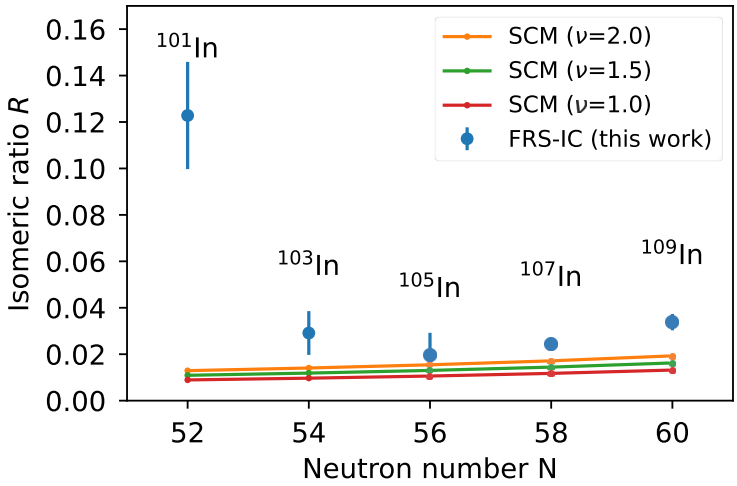

Figure 3.6: Isomeric ratios R of $1/2^-$ isomeric states of odd-A isotopes of $^{101-109}$In as a function of neutron number. Experimental values obtained in this work (blue circles) are compared to the predictions of the sharp cutoff model (SCM). Calculations for different values of ν of (1.0, 1.5, 2.0) are shown in yellow, green and red correspondingly. The lines are guides to the eye. Please see text for details.

momentum of the isomers $J_m = 1/2$ is smaller than that of the corresponding ground states $J_{g.s.} = 9/2$. The mentioned SCM assumption means that the isomer population pathways occur through the ground state, which is clearly not the case. Following the treatment of such cases suggested in [Häfner et al., 2019], the limits of integration in Eq. 3.4 are changed to be taken from zero up to the J_m. Combining it with Eq. 3.5, one obtains the formula to estimate the isomeric ratio R'_{theor} as:

$$R'_{\text{theor}} = \int_0^{J_m} P_J dJ = 1 - \exp\left(-\frac{J_m(J_m+1)}{2\sigma_f^2}\right). \tag{3.8}$$

Eq. 3.8 describes the assumption that all states with $J < J_m$, and only those, populate the isomeric state via spin-increasing transitions.

From experimental perspective, the isomeric ratio is a ratio of a signal from the isomeric state to the combined signal from the ground and all isomeric states. Therefore, the isomer-to-ground-state ratios r, listed in Table 3.2, were converted into isomeric ratios as $R_{\text{exp}} = r/(r+1)$ in order to provide a clear comparison with R'_{theor}. Note that for ^{109}In, both isomeric states $(1/2^-)$ and $(19/2^+)$ were taken into account as $R_{\text{exp}} = r_{1/2^-}/(r_{1/2^-} + r_{19/2^+} + 1)$.

The comparison between experimental isomeric ratios and theoretical predictions of the SCM for $1/2^-$ isomeric states of odd-A isotopes of $^{101-109}$In is shown in Fig. 3.6 as a function of neutron number. It can be seen that the SCM predictions underestimate the experimental values. This contradicts an often-made statement that the SCM predictions of R give an upper limit (see *e.g.*, [Podolyák, 2005, Park et al., 2019, Häfner et al., 2019]). On one hand, contrary to the assumptions of the SCM (Eq. 3.8), not all levels below J_m feed the isomeric state, which should further decrease the R'_{theor}. On the other hand, the assumption that the states with $J < J_m$ are the only ones that feed the isomer is also crude

and offsets R'_{theor} in the opposite direction.

The most striking observation is the discrepancy in the trend towards the $N = 50$ shell closure. As the number of neutrons decreases from $N = 60$, the SCM shows a continuous, almost linear decrease, whereas for the experimental isomeric ratios, the smooth non-linear trend changes from descending to ascending at $N = 56$. The discrepancy is the strongest at $N = 52$ where it reaches about a factor of 10. Such a large discrepancy cannot be attributed solely to the assumptions discussed above, and suggests that feeding of an isomeric state strongly depends on the structure of the final nucleus. In order to achieve a better agreement, more sophisticated considerations regarding the de-excitation process are needed.

3.2.3 Impact of core excitations in $1/2^-$ isomeric states of In

Excitation energies of isomeric states in ^{97}Ag and odd-A isotopes of $^{101-109}$In measured at the FRS-IC allowed to study the evolution of $p_{1/2}$ proton and $g_{9/2}$ single-hole energies towards ^{99}In – one-proton hole of ^{100}Sn – using various shell model (SM) approaches (Figure 3.7). The SM calculations were performed by Magdalena Górska, Hubert Grawe and Andrey Blazhev. The LSSM–V_{MU} calculations (see below) were performed by Noritaka Shimizu, Yusuke Tsunoda and Takaharu Otsuka. The results were published in [Hornung et al., 2020].

For the N=50 odd-Z isotones, a shell model with an isospin-asymmetric interaction (SM–GF) [Gross and Frenkel, 1976] was used in a $\pi\nu(p_{1/2}, g_{9/2})$ model space, above a hypothetical ^{76}Sr core. The single particle energies (SPE) and two-body matrix elements (TBME) were fitted to binding energies and energy spectra of N,Z$\leqslant$50 nuclei.

The output of SM–GF model is in agreement with experimental data as can be seen in Figure 3.7a. Excitation energy of $1/2^-$ isomeric state previously known until ^{95}Rh [Jain et al., 2015] could be extended to ^{97}Ag with the measurement presented in this work, thus enabling a reliable extrapolation towards ^{99}In. The extrapolation anchored further calculations along the In isotopic chain.

For the odd-A In isotopes at N$\geqslant$50, a $\pi(p_{1/2}, g_{9/2}), \nu(g_{7/2}, d_{3/2}, d_{5/2}, s_{1/2}, h_{11/2})$ model space above a hypothetical ^{88}Sr core was selected using a realistic G-matrix based interaction described in [Hjorth-Jensen et al., 1995], and labeled SM–MHJM in this work. The monopole was adjusted to reproduce single particle/hole energies of ^{100}Sn [Kavatsyuk et al., 2007]. The $\pi\pi$ and $\nu\nu$ TBME were monopole corrected to account for the collective motion of the nucleons such that the binding energies of N>50 isotopes are estimated correctly.

Results presented in Figure 3.7b show a general agreement between the output of SM–MHJM model and experimental data for all isotopes except ^{101}In. A downward kink in ^{101}In may be due to overestimated $\pi\nu$ interaction in N>50 isotopes. An inspection of wave functions indicated that the $1/2^-$ (isomeric) state was coupled to a 0^+ state of Sn isotone, while for the $9/2^+$ (ground) state, a coupling to 2^+–8^+ states was allowed. The influence of the latter states could give rise to an increased excitation energy via the core excitations effect, known *e.g.*, from ^{98}Cd [Blazhev et al., 2004] and ^{102}Sn [Nowacki, 2002] – two-proton and two-neutron holes of ^{100}Sn.

The effect of core excitations was considered in an alternative approach,

where the monopole based universal interaction V_{MU} [Otsuka et al., 2010] (labeled here as LSSM–V_{MU}) was used in the same model space as SM–MHJM, and was from [Togashi et al., 2018]. A quenching factor of 0.75 was applied in the central force channel where the total isospin T=1. The SPE were selected to reproduce present interaction and are from [Togashi et al., 2018]. In ^{99}In, the $p_{1/2}$ SPE were tuned to reproduce the general trend. Up to 3p3h excitations across Z, N=50, and 1p1h from $(g_{7/2}, d_{5/2})$ to $(d_{3/2}, s_{1/2}, h_{11/2})$ were allowed by applying a truncation.

As can be seen in Fig. 3.7b, the output of LSSM–V_{MU} model is in a excellent agreement with experimental data. In particular, the kink in ^{101}In is reduced, which demonstrates the impact of core excitations in low-lying, dominantly single hole states.

It is noteworthy that 3 years later after the publication in [Hornung et al., 2020], the excitation energy of ^{99}In^{m} isomer was measured at ISOLTRAP group by [Nies et al., 2023]. The reported value of $E_x = (671 \pm 37)\,\mathrm{keV/c^2}$ is in perfect agreement with the SM-GF and the LSSM-V_{MU} extrapolations.

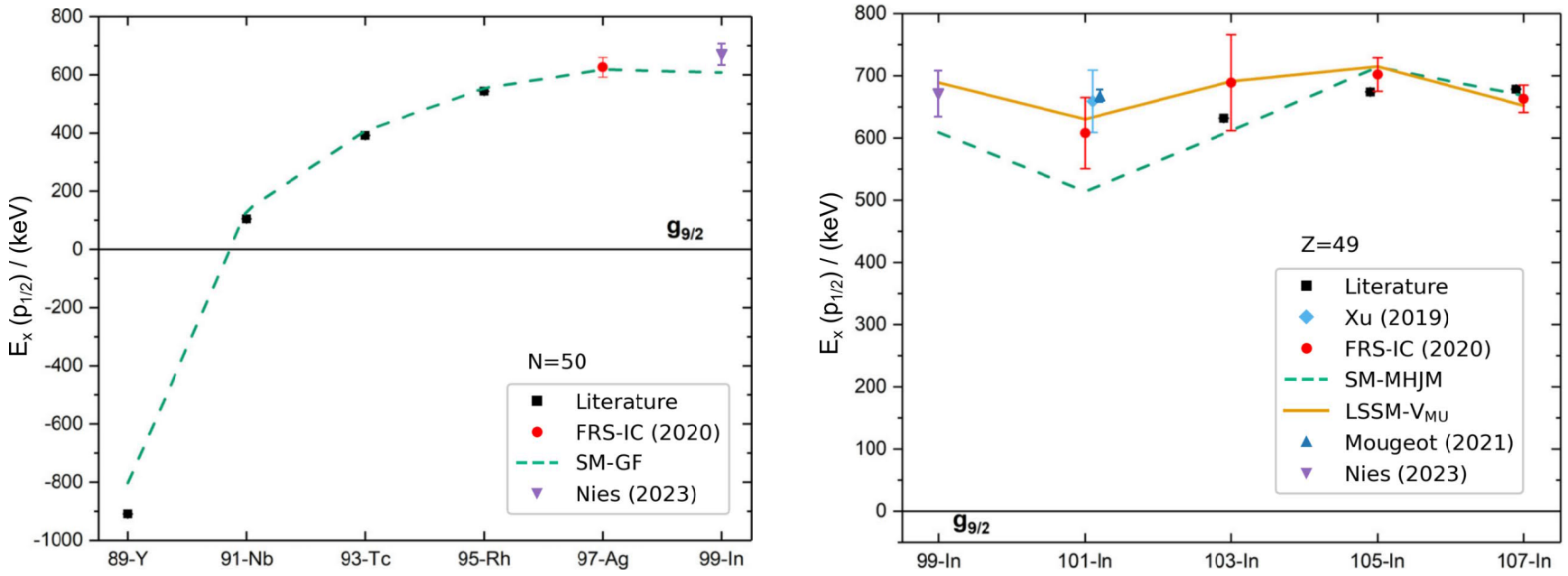

(a) N=50 odd-Z isotones

(b) odd-N isotopes of indium Z = 49

Figure 3.7: Evolution of $p_{1/2}$ proton and $g_{9/2}$ single-hole energies $\mathrm{E_x(p_{1/2})}$ towards ^{99}In along (a) N=50 odd-Z isotones, and (b) odd-N isotopes of indium Z = 49. Literature values (black squares) are from [Jain et al., 2015]. In (a), measurement presented in this work (red circles) extends $\mathrm{E_x(p_{1/2})}$ values until ^{97}Ag. A reliable extrapolation towards ^{99}In became possible. It was performed with SM-GF shell model (dashed green line) and anchored calculations shown in (b). The excitation energy of $^{99}\mathrm{In}^m$ (purple triangle) measured 3 years later by [Nies et al., 2023] is in perfect agreement with the SM-GF extrapolation. In (b), a comparison of excitation energies presented in this work (red circles) to the literature (black square) shows a good agreement where available. For ^{101}In, a discrepancy between experimental data and an SM-MHJM model (green dashed line) could be resolved after considering core excitations within an alternative LSSM-V_{mu} approach (yellow solid line). Mass and excitation energy of ^{101}In presented in this work are second to and in agreement with the values reported by [Xu et al., 2019] (cyan diamond). A value reported a year later by [Mougeot et al., 2021] (blue triangle) confirms previous measurements. Again, the recent (2023) measurement of $^{99}\mathrm{In}^m$ by [Nies et al., 2023] (purple triangle) is in perfect agreement with the LSSM-V_{MU} extrapolation. Adopted and modified from [Hornung et al., 2020].

3.2.4 Supporting the discovery of a $(1/2^-)$ isomeric state in ^{97}Ag

The experimental findings in ^{97}Ag presented in this work – a long-lived $(1/2^-)$ isomeric state with an excitation energy of (618 ± 38) keV/c^2 – were studied from theoretical perspective. The large-scale nuclear mean-field calculations were performed in the region of interest by Irene Dedes and Jerzy Dudek, and were published in [Hornung et al., 2020].

As discussed in [De Voigt et al., 1983], a predominant mechanism responsible for building up high angular momentum in a spherical or oblate symmetrical nucleus is an alignment of angular momenta of individual nucleons. It is sufficient for only a few valence nucleons to align their angular momenta with the symmetry axis of the nucleus in order to achieve a high angular momentum. The nuclear angular momentum is the highest when projections of individual nucleonic angular momenta on the symmetry axis are the largest. One can study filling up the nucleonic orbitals in a given nucleus by minimizing the sum of single-particle energies (SPE) e_ν,

$$\min \sum_{\nu_{\mathrm{occ}}} e_\nu, \tag{3.9}$$

for a given angular momentum J,

$$J \approx J_x = \sum_{\nu_{\mathrm{occ}}} m_\nu. \tag{3.10}$$

The Eq. 3.10 implies that "rotation" happens almost around the symmetry axis, and therefore the total angular momentum J is approximately equal to its projection on the symmetry axis J_x, and is constructed from projections of angular momentum of individual nucleons m_ν. The minimization is limited to occupied states ν_{occ}.

The resulting sets of e_ν and m_ν can be visualized as points in an energy-momentum plane (e, m) for qualitative and quantitative interpretations, prediction of possible isomeric states and other applications that are beyond the scope of this work. This method is also known as "tilted Fermi surface".

In this work, the mean-field calculations of ^{97}Ag nucleus involved the minimization individually, over the axial quadrupole β_2 and hexadecapole β_4 deformations of each particle-hole excited-state energy. The phenomenological Woods-Saxon Hamiltonian was chosen, with the universal parameterization of its potential [Dudek et al., 1981]. A single set of parameters describes, on average, all the individual nucleonic energy levels in nuclei throughout the chart of nuclides. The relevant information is summarized in [Cwiok et al., 1987]. No readjustments related to the isomers and/or the excitation spectra have been performed.

The "tilted Fermi surface" results shown in Figure 3.8 display a series of proton configurations in a deformed ($\beta_2 = -0.09, \beta_4 = +0.02$) mean-field of ^{97}Ag nucleus. The figure is limited to 13 valence protons which occupy the $1g_{9/2}, 2p_{1/2}$ and $2p_{3/2}$ orbitals. All other orbitals down to the bottom of the potential well are considered occupied. Out of 13 protons, 6 protons occupy $2p_{1/2}$ and $2p_{3/2}$ orbitals with their angular momentum projections m_j being pairwise anti-parallel. According to Eq. 3.10, their contributions to the total angular momentum J are mutually

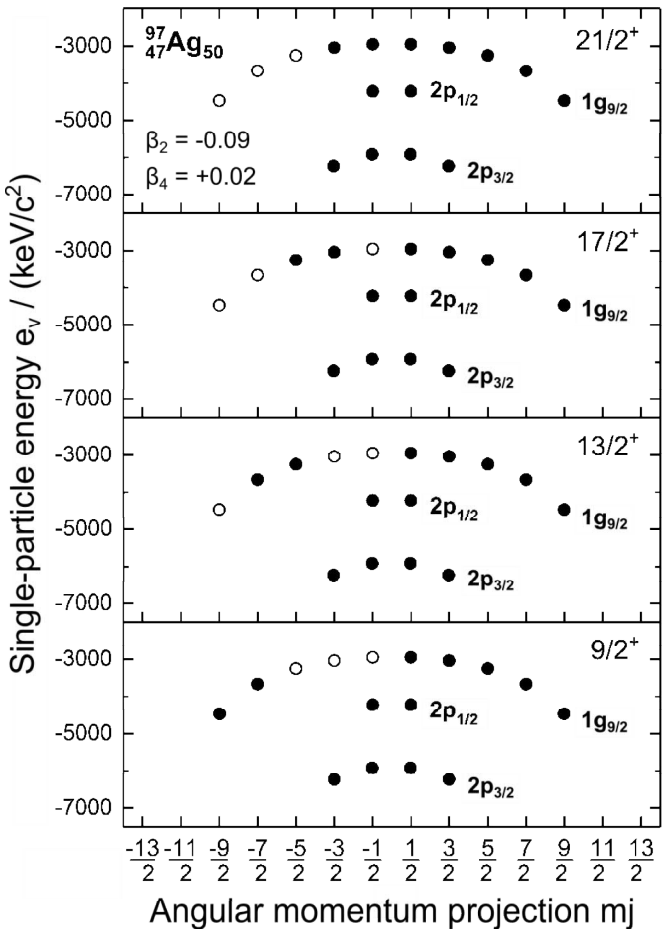

Figure 3.8: Valence proton configurations (single-particle energy vs angular momentum projection m_j) in a deformed ($\beta_2 = -0.09, \beta_4 = +0.02$) mean-field of ^{97}Ag nucleus. Ground state with spin-parity $J^\pi = 9/2^+$, higher-spin $13/2^+$, $17/2^+$, and the maximum alignment $21/2^+$ configurations are shown. The occupied and vacant states are shown as filled and open symbols accordingly. The $1/2^-$ state can be constructed by promoting one proton from $2p_{1/2}$ orbital to one of the three vacant states in $1g_{9/2}$ orbital. This supports the discovery of $(1/2^-)$ isomeric state in ^{97}Ag presented in this work (see text for details). Adopted from [Hornung et al., 2020].

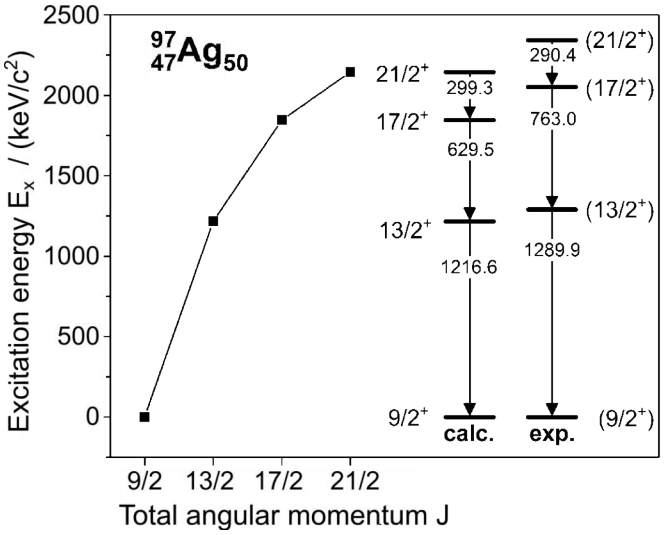

Figure 3.9: Comparison of calculated excitation energy E_x of the $9/2^+$, $13/2^+$, $17/2^+$ and $21/2^+$ sequence of ^{97}Ag to the experimental data from ENSDF [ENSDF, 2020]. E_x were calculated as a difference of the SPE e_ν of protons which do not occupy the same states in the neighboring configurations shown in Fig. 3.8. The satisfactory agreement can be seen. Adopted from [Hornung et al., 2020].

canceled. The remaining protons 7 to 13 occupy $1g_{9/2}$ orbital. The following observations are in agreement with the data and systematics known from literature, and thus provide confidence in the underlying method:

1. The highest occupied proton state is in the $1g_{9/2}$ orbital *i.e.*, this orbital is the closest to the Fermi level, therefore a ground state of ^{97}Ag must have spin-parity of $J^\pi = 9/2^+$.

2. Higher J^π states $13/2^+, 17/2^+$ and $21/2^+$ might emerge from aligning proton angular momenta. $J^\pi = 21/2^+$ is the maximum alignment configuration possible before breaking the Z = 50 core. The corresponding proton distributions are shown in the panels of Fig. 3.8.

3. As pairs of protons are removed, the ground state of odd-A, N=50 isotones below ^{97}Ag (Z=47) must remain $9/2^+$ until ^{91}Nb (Z=41) because the $1g_{9/2}$ orbital remains occupied. Removing next pair of protons makes $2p_{1/2}$ closest to the Fermi surface, therefore ground state of ^{89}Y must be $1/2^-$. The same is true for ^{87}Rb with $3/2^-$ ground state.

For $9/2^+$, $13/2^+$, $17/2^+$ and $21/2^+$ sequence, the excitation energies E_x can be calculated. For this, the SPE e_ν of all protons of one configuration $(J^\pi)_i$ are summed up, and the sum is subtracted from that of the configuration above $(J^\pi)_{i+1}$:

$$E_\mathrm{x} = \sum_{m_j} e_\nu \Big|_{(J^\pi)_{i+1}} - \sum_{m_j} e_\nu \Big|_{(J^\pi)_i} . \tag{3.11}$$

In Fig. 3.8 it can be seen that most of the protons occupy the same states, and thus cancel each other in Eq. 3.11. Therefore, it is sufficient to take the difference of the e_ν of the protons which occupy different states. For example, in the $13/2^+$ and $9/2^+$ configurations, such protons occupy states with $m_j = -5/2$ and $m_j = -9/2$ correspondingly. The excitation energy of $13/2^+$ configuration is therefore $E_x = e_\nu(-5/2) - e_\nu(-9/2) = 1216.6\,\mathrm{keV/c^2}$. The excitation energies of other configurations were calculated in the same way. As shown in Figure 3.9, theoretical results are in satisfactory agreement with the experimental data taken from ENSDF [ENSDF, 2020], especially given that no parameter adjustment of the employed Woods-Saxon potential has been performed.

Furthermore, the method enables formulating certain predictions about the nature of $(1/2^-)$ isomeric state. The $1/2^-$ state can be constructed by promoting one proton from $2p_{1/2}$ orbital to one of the three "vacant" states in $1g_{9/2}$ orbital. The total angular momentum J is defined by the remaining proton in $2p_{1/2}$, while 8 protons in $1g_{9/2}$ are in pairwise anti-parallel configuration, and thus are canceled in Eq. 3.10. Depending on which state in $1g_{9/2}$ became occupied, several proton configurations corresponding to $1/2^-$ are possible. The excitation energies of such configurations are centered around $E_\mathrm{exc} \approx (600 \pm 400)\,\mathrm{keV/c^2}$. Decay of $1/2^-$ state to $9/2^+$ state can be hindered because it requires a change of spin of $\Delta J = 4$ and a change of parity. Therefore it is expected that $1/2^-$ state will form a long-lived isomer.

The predictions formulated above support the discovery of $(1/2^-)$ isomeric state in ^{97}Ag, and the experimental results presented in this work.

3.3 Results on the lightest neutron-rich nuclei at N=126

In the S468 experiment (see Section 2.3.2), masses of many exotic nuclei in the region of $N = 126$ below ^{208}Pb have been measured, as can be seen in Figure 3.10.

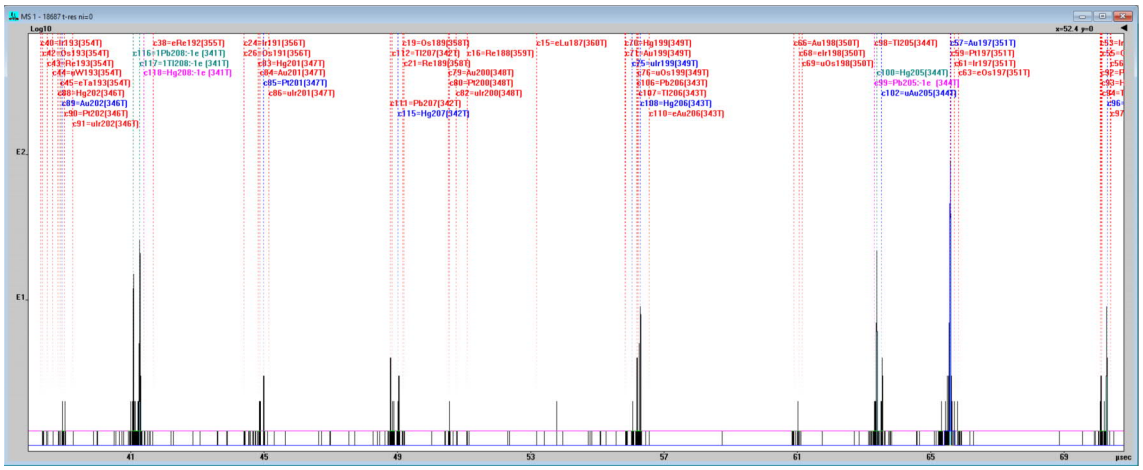

Figure 3.10: Screenshot of TOF spectrum of exotic nuclei collected during the S468 experiment with the FRS-IC. The colored vertical lines and labels mark positions of potential ions of interest. The ordinate is in logarithmic scale.

The data analysis is in progress. This work features the results of mass measurements of $^{203-205}$Au isotopes. The details of data analysis and discussion are presented in this section.

3.3.1 Data analysis

Two data sets were analyzed according to procedure described in Section 3.1. In a data set I, the reference ion undergoes 300 isochronous turns (IT) in the MR-TOF-MS analyzer. The data were collected over 2.5 hours during setup of the MRB (see Section 2.2), while all other parameters of the FRS and the FRS-IC remained fixed. The changes in the MRB only affected the number of ions stopped in the prototype CSC and had no effect on measured TOF values. In a data set II, the reference ion undergoes 351 IT. The data were collected over 5.2 hours under stable and unchanged conditions after setting up the MRB.

For both data sets, TOF spectra were converted to mass-over-charge spectra according to Eq. 3.1, where t_0 of (274 ± 2) ns was determined offline, and b and c were obtained using calibrant ions ^{197}Au and ^{208}Tl – stable isotopes with a well-known mass measured together with the ions of interest. The time-resolved calibration and the peak shape were obtained from ^{197}Au – ions with the highest count rate. The Hyper-EMG function with one exponential tail on each side has been found to describe the peak shape best in both data sets. The results from two data sets were averaged when possible according to procedure described in [Ayet San Andrés et al., 2019]. Results of the mass measurements are summarized in Tables 3.3 and 3.4, and Figure 3.14.

The mass of ^{203}Au

The mass of ^{203}Au nuclide has been previously determined only indirectly via Q-value of a ^{204}Hg(d,^{3}He)^{203}Au reaction. This reaction was per-

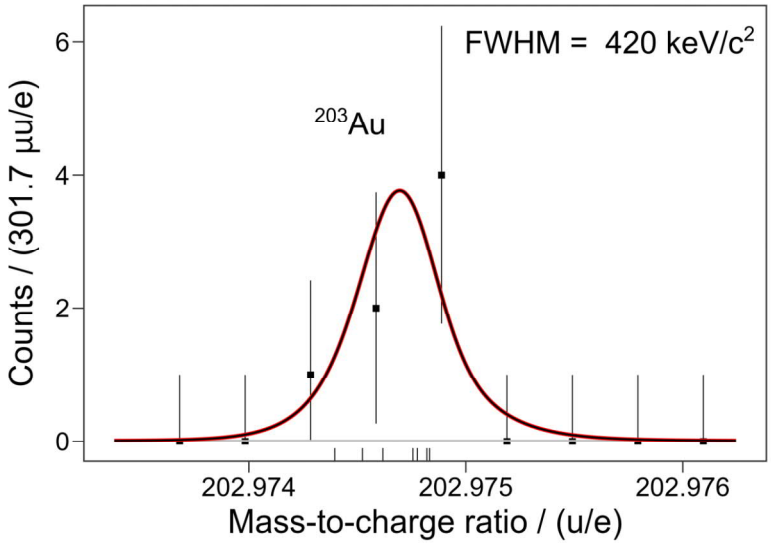

Figure 3.11: Measured mass-over-charge spectrum of ^{203}Au nuclide. The spectrum features first direct mass measurement of ^{203}Au. Square points represent the histogram of unbinned data which is shown as a rug plot below the histogram. The red curve represents fit to the unbinned data. The ions performed 297 IT with a total TOF of about 13.1 ms. A FWHM of 420 keV/c^2 renders mass resolving power of 450 000.

formed simultaneously with a ^{206}Pb(d,^{3}He)^{205}Tl reaction which Q-value is known [Grabmayr et al., 1994]. The derived mass value is recommended by the atomic mass evaluation 2020 (AME2020) [Wang et al., 2021].

This work presents the first direct mass measurement of ^{203}Au nuclide (Figure 3.11). In data set I, 7 events were collected. Ions of ^{203}Au performed 297 IT with a total TOF of about 13.1 ms. A full width at half maximum (FWHM) of 420 keV/c^2 renders mass resolving power of 450 000. A total relative uncertainty of $5.1 \cdot 10^{-7}$ which corresponds to 96 keV/c^2 is dominated by statistical uncertainty. In data set II, 203 u isobars were filtered out from the MR-TOF-MS analyzer by the MRS (see Section 2.1.2). As expected, no events of ^{203}Au were registered.

The measured mass excess and uncertainty values of ^{203}Au nuclide are given in Table 3.3, and are compared to the AME2020 value. The comparison is also demonstrated in Figure 3.14. The measured mass excess deviates from previous indirect mass measurement recommended by AME2020 by 1.5σ.

The mass of ^{204}Au

The mass excess value and uncertainty provided by AME2020 are derived not from experimental data, but based on trends from the mass surface. The only prior indirect mass measurement of ^{204}Au has been performed via the endpoint energy of its $\beta-$ decay by [Ward et al., 1967]. This result, however, has been invalidated because the activity with a half-life of 4 s assigned to ^{204}Au in [Ward et al., 1967] has not been observed in a much more detailed study by [Pakkanen et al., 1972].

This work features mass of ^{204}Au nuclide measured for the first time

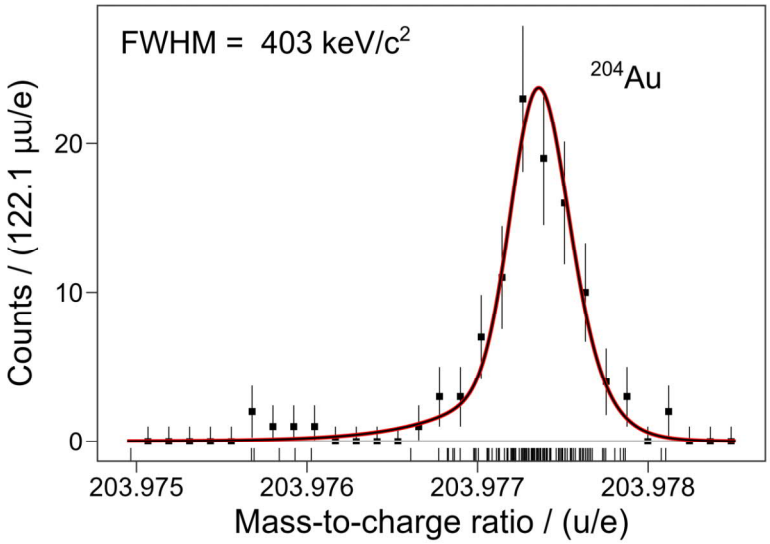

Figure 3.12: Mass-over-charge spectrum of ^{204}Au nuclide measured for the first time. Results from data set II are plotted. Square points represent the histogram of unbinned data which is shown as a rug plot below the histogram. The red curve represents fit to the unbinned data. The ions performed 345 IT with a total TOF of about 15.3 ms. A FWHM of 403 keV/c^2 renders mass resolving power of 470 000. Five events around m/q = 203.976 u/e are of an unidentified origin. Including or rejecting these events only changes the mass excess value of ^{204}Au by 2 keV/c^2, which is not a significant change of the result.

(Figure 3.12). In data set I, 77 events were collected. The ions performed 296 IT with a total TOF of about 13.1 ms. A FWHM of 423 keV/c^2 renders mass resolving power of 450 000. A total relative uncertainty of $1.8 \cdot 10^{-7}$ which corresponds to 35 keV/c^2 is dominated by statistical uncertainty. In data set II, 108 events were collected. The ions performed 345 IT with a total TOF of about 15.3 ms. A FWHM of 403 keV/c^2 renders mass resolving power of 470 000. A total relative uncertainty of $1.5 \cdot 10^{-7}$ which corresponds to 28 keV/c^2 is dominated by statistical uncertainty.

As can be seen from Table 3.3, the individual mass excess values obtained from data sets I and II are in good agreement with each other. Combining and averaging the results improved the total relative uncertainty to $1.3 \cdot 10^{-7}$ which corresponds to 24 keV/c^2. As can be seen in Fig. 3.12, in data set II, five events around m/q = 203.976 u/e are present. These events are not part of the ^{204}Au peak, and are not random background. Their origin has not been identified. Including or rejecting these events in the fitting procedure only changes the mass excess value of ^{204}Au by 2 keV/c^2, which is not a significant change of the result.

The measured averaged mass excess value of ^{204}Au deviates from the mass surface extrapolation of AME2020 by (-258 ± 201) keV/c^2. Interestingly, in an earlier edition of atomic mass evaluation 2016 (AME2016) [Wang et al., 2017], the extrapolated mass excess value was in an excellent agreement with the measurement, deviating by (2 ± 201) keV/c^2.

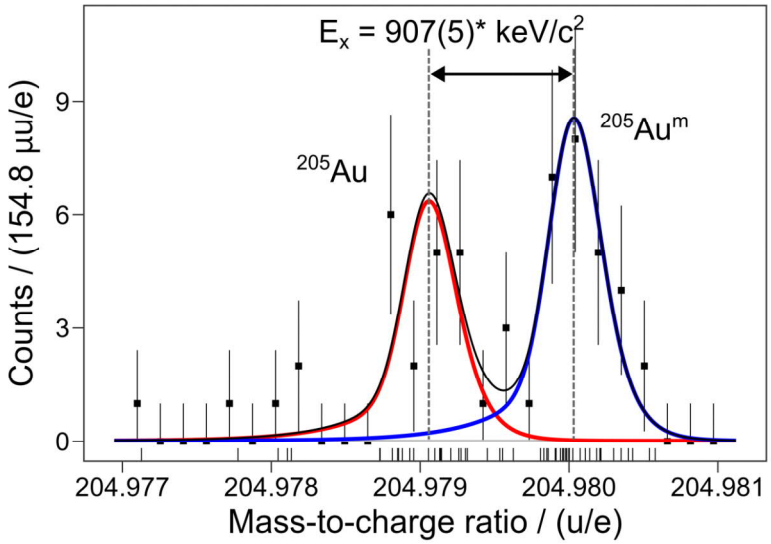

Figure 3.13: Mass-over-charge spectrum of ^{205}Au ground state (g.s.) measured for the first time and its $J^\pi = 11/2^-$ isomeric state (i.s.). Results from data set II are plotted. Square points represent the histogram of unbinned data which is shown as a rug plot below the histogram. The red, blue and black curves are fits to the unbinned data of g.s., i.s., and their sum correspondingly. *The isomer excitation energy E_x adopted from [Podolyák et al., 2009]. Please see text for details.

The mass and isomer excitation energy of ^{205}Au, ^{205}Au^m

No prior mass measurement of ^{205}Au nuclide exists. The mass excess value and uncertainty of AME2020 are derived from the mass surface trends.

This work features first mass measurement of the heaviest isotope of gold ^{205}Au. Additionally, a $J^\pi = 11/2^-$ isomeric state of ^{205}Au^m was detected and its excitation energy measured (Figure 3.13). The isomer has been measured at GSI earlier by [Podolyák et al., 2009].

In both data sets, the ground state (g.s.) and isomeric state (i.s.) were overlapping within 2 FWHM, and therefore were fitted together as a double-peak. In data set I, 38 events for g.s. and i.s. combined were collected. The ions performed 295 IT with a total TOF of about 13.1 ms. A FWHM of 426 keV/c^2 for both peaks renders mass resolving power of 450 000. A total relative uncertainty of $2.4 \cdot 10^{-7}$ which corresponds to 46 keV/c^2 is dominated by statistical uncertainty. In data set II, 53 events for g.s. and i.s. combined were collected. The ions performed 344 IT with a total TOF of about 15.3 ms. A FWHM of 406 keV/c^2 renders mass resolving power of 470 000. A total relative uncertainty of $2.0 \cdot 10^{-7}$ which corresponds to 38 keV/c^2 is dominated by statistical uncertainty. Combining and averaging the results improved the total relative uncertainty to $1.6 \cdot 10^{-7}$ which corresponds to 31 keV/c^2.

The measured averaged mass excess value of ^{205}Au strongly deviates from the mass surface extrapolation of AME2020 by (-497 ± 202) keV/c^2.

For ^{205}Au^m, the isomer excitation energy E_x of (907 ± 5) keV/c^2 measured earlier by [Podolyák et al., 2009] was used in this work to fix the distance between

centroids of Gaussian components of the overlapping peaks of ^{205}Au and ^{205}Au^{m} in the mass fitting procedure. This allowed to eliminate an uncertainty from the correction for overlapping peaks which would otherwise increase the total uncertainty by ∼50%. The details about the "fixed-distance" mass fitting can be found in [Kripko-Koncz, 2023]. The results were cross-checked by keeping the distance between the peaks as a free parameter. The excitation energies from both data sets are in 0.9σ agreement with the literature value, as can be seen from Table 3.4. Furthermore, an isomer-to-ground state ratio of 1.4 ± 0.1 with total number of 91 counts in two data sets was determined. The spin-parity of $J^{\pi} = (11/2^{-})$ was taken from NUBASE2020 [Kondev et al., 2021].

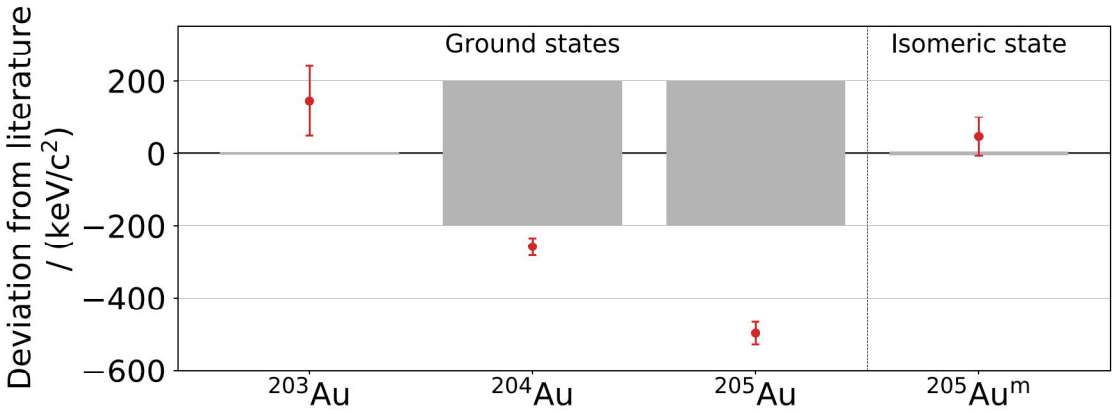

Figure 3.14: Deviation of masses of $^{203-205}$Au and excitation energy of ^{205}Au^{m} measured in this work (see Tables 3.3 and 3.4) from literature values taken from atomic mass evaluation 2020 (AME2020) [Wang et al., 2021]. The error bars represent total experimental uncertainty. The gray band around the horizontal axis represents the AME2020 uncertainty.

Table 3.3: Mass excess and uncertainty of $^{203-205}$Au isotopes measured at the FRS-IC during the S468 experiment. Two data sets were analyzed and averaged when possible according to [Ayet San Andrés et al., 2019]. The uncertainties of the measured values are the total experimental uncertainties. The measured mass excess values are compared with the literature values from AME2020 [Wang et al., 2021]. Masses of ^{204}Au and ^{205}Au were measured for the first time. In case of ^{203}Au, it is the first direct mass measurement.

Nuclide	Calibrant	Data set	Number of events	$ME_{FRS\text{-}IC}$ /(keV/c^2)	$ME_{AME2020}$ /(keV/c^2)	$ME_{FRS\text{-}IC} - ME_{AME2020}$ /(keV/c^2)
^{203}Au	^{197}Au	I	7	−22 998 ± 96	−23 143 ± 3	145 ± 96
		II	0*	–		
		avg.	–	–		
^{204}Au	^{197}Au	I	77	−20 632 ± 35		
		II	108	−20 658 ± 28		
		avg.		−20 648 ± 24	−20 390 ± 200#	−258 ± 201
^{205}Au	^{197}Au	I	15	−19 057 ± 46		
		II	23	−19 074 ± 38		
		avg.		−19 067 ± 31	−18 570 ± 200#	−497 ± 202

* the isotope was filtered out from the MR-TOF-MS analyzer by the MRS.
# value and uncertainty derived not from experimental data, but based on trends from the mass surface.

Table 3.4: Excitation energy and isomer-to-ground-state ratio of $^{205}Au^{m}$ $(11/2^{-})$ isomeric state measured at the FRS-IC. Two data sets were analyzed and averaged according to [Ayet San Andrés et al., 2019]. The literature value is taken from [Podolyák et al., 2009] adopted by the NUBASE2020 [Kondev et al., 2021].

Isomer	Half-life	J^{π}	Data set	$E_{x,\,\text{FRS-IC}}$ /(keV/c^2)	$E_{x,\,\text{lit}}$ /(keV/c^2)	$E_{x,\,\text{FRS-IC}} - E_{x,\,\text{lit}}$ /(keV/c^2)	Isomer-to-ground-state ratio
$^{205}Au^{m}$	(6 ± 2) s	$11/2^{-}$	I	980 ± 82			1.5 ± 0.2
			II	934 ± 69			1.3 ± 0.1
			avg.	953 ± 53	907 ± 5	46 ± 54	1.4 ± 0.1

3.3.2 Trends along the N=126 shell closure below ^{208}Pb

The newly measured masses of isotopes of gold $^{203-205}$Au can be used to examine the N=126 shell closure below ^{208}Pb via a two-neutron separation energy S_{2n} defined as:

$$\begin{aligned} S_{2n}(N,Z) &= \mathrm{BE}(N,Z) - \mathrm{BE}(N-2,Z) \\ &= \mathrm{ME}(N-2,Z) + 2\mathrm{ME}_n - \mathrm{ME}(N,Z), \end{aligned} \tag{3.12}$$

where $\mathrm{BE}(N,Z)$ and $\mathrm{ME}(N,Z)$ are binding energy and mass excess of a nuclide correspondingly, and $\mathrm{ME_n}$ is the mass excess of the neutron. In general, as the number of neutrons increases, the S_{2n} is expected to decrease steadily indicating that the pair of neutrons becomes less bound to the nucleus; at the neutron shell closures the S_{2n} decreases rapidly.

Figure 3.15 shows two-neutron separation energies S_{2n} plotted for neutron-rich isotopes of elements from Pt to Pb around the N=126 shell closure. In case of Au, S_{2n} values previously known until N=124 could be extended until N=126 with the new mass measurements presented in this work. It can be seen that the new S_{2n} values deviate significantly from AME2020 and do not support local trends, especially ^{205}Au (N=126).

New S_{2n} values were compared to predictions of the following mass models: DZ31 [Duflo and Zuker, 1995], WS3+RBF [Wang and Liu, 2011], FRDM12 [Möller et al., 2016] and HFB21 [Goriely et al., 2010]. The mass models were selected based on study of [Sobiczewski and Litvinov, 2014] who showed that for medium-heavy nuclei the models DZ31, FRDM12 and WS3+RBF reproduce experimentally measured masses best, and the latter demonstrated the strongest predictive power. The HFB21 model was included for completeness because it represents purely microscopic (self-consistent) mass models *i.e.*, of a completely different nature. Further, these mass models are commonly used in r-process calculations (see *e.g.*, [Mendoza-Temis et al., 2015]).

The best agreement with the new experimental data is achieved with DZ31. However, this fact is insufficient to prefer this model to others. It is known that DZ31 outputs a rather smooth mass surface, and therefore has poor descriptive and predictive power in terms of nuclear structure effects. For instance, in Fig. 3.15 it can be seen that DZ31 does not reproduce S_{2n} kink at N=125 for Pb isotopes. The FRDM12 shows a good agreement at N=125, however predicts smaller binding energy of ^{205}Au, hence too strong decrease of S_{2n} at N=126. WS3+RBF follows the AME2020 extrapolated values exactly. HFB21 disagrees with data the most, especially approaching the N=126 shell closure. Its predicted trend of increasing S_{2n} from N=123 to N=125 is not confirmed.

Diverging predictions of mass models impact applications which rely on them. One clear instance is the r-process nucleosynthesis calculations. Such studies involve properties of nuclei which are presently out of reach at RIB facilities. Therefore they rely on theoretical models, including mass models. It has been shown in [Mendoza-Temis et al., 2015] that the position of the third peak (A$\sim$195 or A$\sim$205) in the calculated r-process abundance distribution is sensitive to mass model output. Our new results emphasize the importance of collecting accurate experimental data on nuclear masses of medium-heavy neutron-rich nuclei. Ex-

tensive mass measurements in the region of N=126 are essential to distinguish and improve diverging theoretical models.

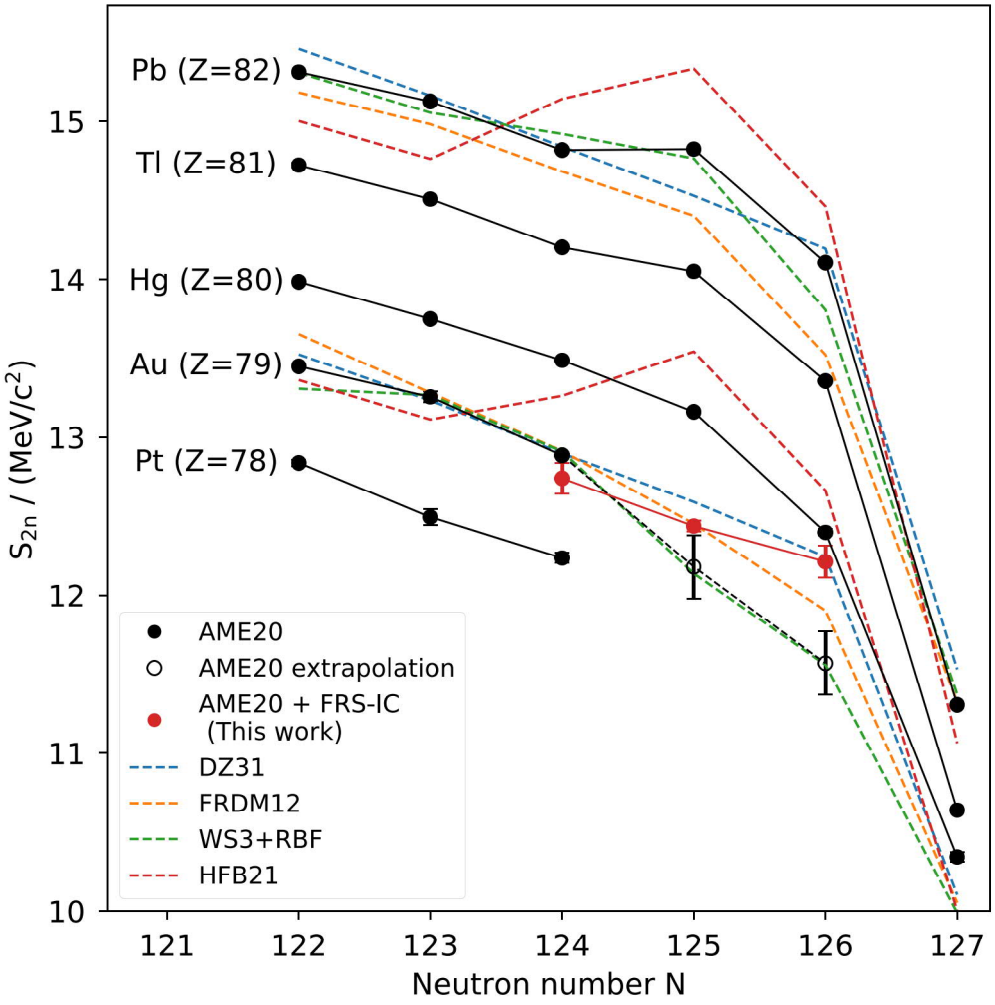

Figure 3.15: Two-neutron separation energies S_{2n} around the N=126 shell closure for elements from Pt to Pb. Experimental values from literature (AME2020) [Wang et al., 2021] (black filled circles) are compared with new values deduced from mass measurements presented in this work (red circles). Extrapolated AME2020 values for Au are given for reference (black empty circles). Predictions of mass models DZ31 [Duflo and Zuker, 1995], FRDM12 [Möller et al., 2016], WS3+RBF [Wang and Liu, 2011], and HFB21 [Goriely et al., 2010] are shown for Au and Pb isotopes (dashed lines).

Chapter 4

Developments beyond mass measurements at the Super-FRS

4.1 INCREASE: in-cell reaction and decay studies system

As mentioned in Section 1.1.4, there is a search for new reaction methods which provide a better access to the $N = 126$, beyond what is technically possible with in-flight fragmentation of stable beams. The multi-nucleon transfer (MNT) reactions are a promising candidate for that role, especially MNT reactions with neutron-rich RIB. At the FRS-IC at GSI, a novel technique to study the MNT reactions [Dickel et al., 2020] and spontaneous fission (SF) [Mardor et al., 2020] in-cell has been proposed. In this work, the instrumentation to conduct proof-of-concept experiments at the FRS-IC has been developed, built and commissioned. It has been optimized for the in-cell MNT reaction and SF studies, and is described in this section.

4.1.1 Requirements and design goals

The MNT reactions will occur between an ion beam and a reaction target installed inside the prototype CSC. In order to ensure efficient use of the beam time, the developed electrode structure design has to accommodate several reaction targets and provide short switching time between them.

The incident ion beam will have a mean energy of $\sim$10 MeV/u and intensity of $\sim 10^7$ ions/s *i.e.*, 3 orders of magnitude larger than the rate capability of the prototype CSC in standard configuration. The developed system must operate at such high beam intensities without experiencing significant efficiency losses.

The system geometry has to be optimized for effective stopping of MNT reaction products with a large angular distribution. Meeting this requirement will also be beneficial for stopping spontaneous fission (SF) fragments that are distributed isotropically. Stopping efficiency of SF fragments at large angles is limited by radial dimensions of the DC cage. In order to minimize the losses at the DC cage electrodes, a beam of SF fragments has to be collimated. Minimizing such losses can be beneficial for IIFY measurements. In case a maximum ion transmission

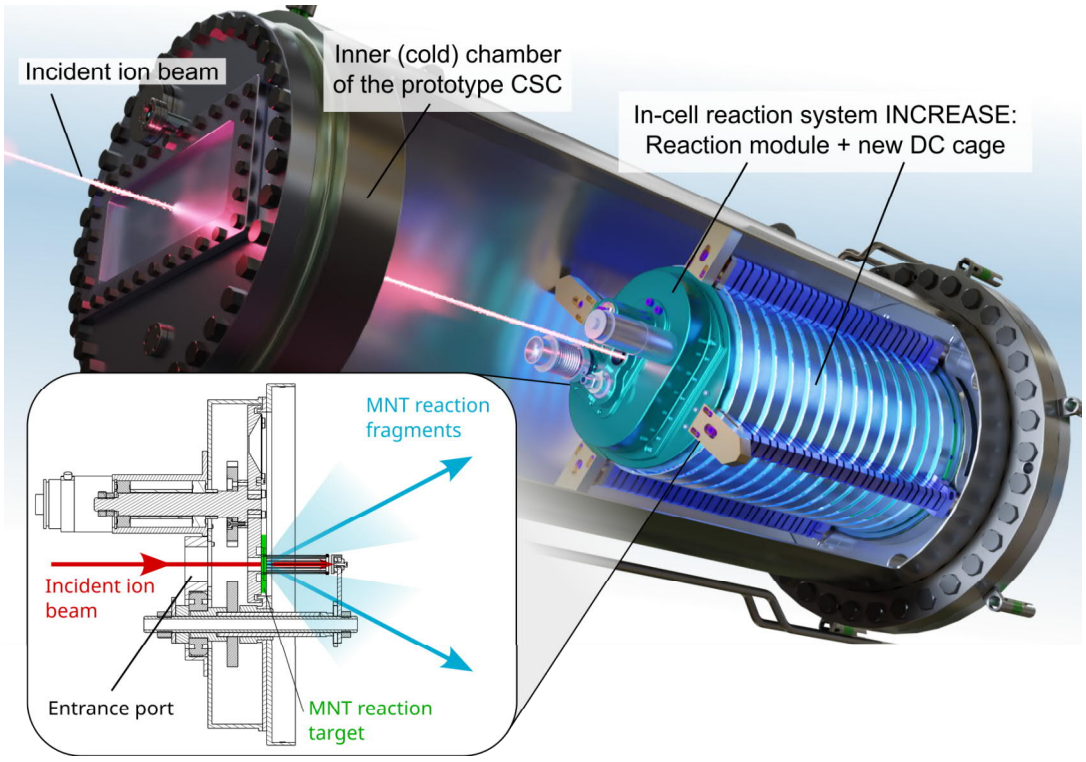

Figure 4.1: Render of an in-cell reaction system (INCREASE) installed inside the inner (cold) chamber of the prototype CSC. The INCREASE consists of a reaction module and a new DC cage. Inset shows a working principle of the reaction module. Please see text for details.

is required *e.g.*, for high-precision mass measurements, an option to switch to a larger aperture has to be available.

Several SF sources will be studied. One SF source can be installed at a time in order not to cross-contaminate sensitive IIFY measurements. In order to ensure quick switching between the sources, they have to be (dis-)mountable through the beam window of the inner chamber. For radiation safety purposes, the part where the SF source is installed has to be enclosed and isolated from the bulk of the prototype CSC.

The new electrode system has to accommodate existing α-recoil source similarly to the standard configuration.

The new system has to be compatible with UHV-conditions and cryogenic temperatures.

4.1.2 Technical design

A newly developed electrode system named “INCREASE” – an in-cell reaction system – consists of two parts: a reaction module and a new (short) DC cage. Figure 4.1 shows a render of the INCREASE installed inside the inner (cold) chamber of the prototype CSC, and its working principle. In the reaction module, an MNT reaction between a ion beam (red) and a target (green) takes place. Alternatively, an SF source (not shown) can be installed at the entrance port. The MNT reaction fragments (or SF fragments) with broad angular distribution are released and

thermalized inside the new DC cage. A DC push field generated by the DC cage electrodes guides ions towards the RF carpet for extraction.

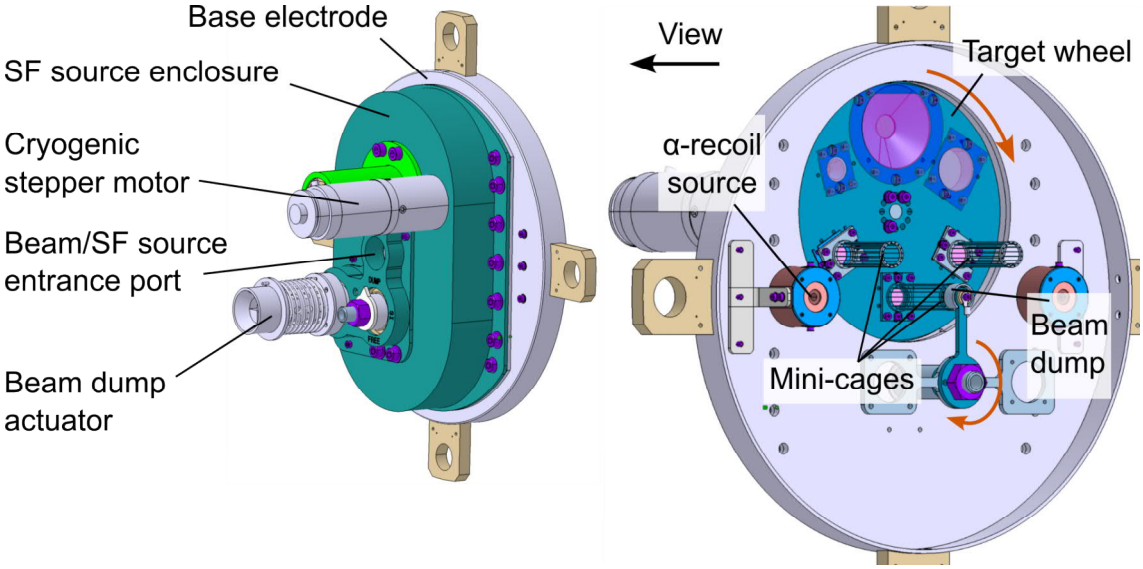

Figure 4.2: A CAD-drawing of the reaction module of the INCREASE. Its major components are a motor-driven target wheel, the mini-cages and a beam dump. The beam dump can be rotated out of the beam axis for the experiments with SF source. Please see text for details.

The reaction module is shown in Figure 4.2. Its major components are a motor-driven target wheel, the mini-cages and a beam dump.

The target wheel accommodates four MNT reaction targets. One target with a diameter of 22 mm is intended for initial tuning, and three other targets with a diameter of 10 mm each are for the dedicated measurements. In addition, two cone apertures with different opening angles in the target wheel collimate SF fragments. A smaller cone aperture with an opening angle of 15° minimizes the transmission of ions which would be lost on the DC cage electrodes; a larger cone aperture with an opening angle of 60° maximizes ion transmission. Both cone apertures are covered with titanium foil with a thickness of 4 μm to optimize stopping of SF fragments. The foil thickness has been selected based on optimization study performed using SRIM [Ziegler et al., 2010] and reported in [Cuillerier and Stanić, 2019]. The study predicts an improvement in stopping efficiency by a factor of $\sim$5 for the standard (long) DC cage of the prototype CSC, and has been experimentally verified [Wasserheß, 2020]. Ti foils on both cone apertures may be replaced by another MNT reaction targets. Thus, up to six MNT targets can be accommodated in the reaction module.

The targets are placed into the path of the primary beam one at a time by rotating the target wheel. The target wheel is actuated by a stepper motor Phytron VSS 43.200.1.2 with a VGPL 42 planetary gear. The motor can be operated remotely via an MCC-2 controller. It is radiation-resistant, and is graded for UHV-conditions and cryogenic temperatures. Also, it is equipped with an optical encoder for a position readout with an accuracy of $\pm$1%. This makes it possible to operate the motor under harsh conditions inside the prototype CSC and thus to ensure a short switching time between the reaction targets of few seconds.

The MNT reaction targets are followed by the so-called mini-cages. A mini-cage is a cylindrical wireframe electrode made of thin wires. It is 95% transparent for the MNT reaction products, and its dimensions are matched to the beam dump (see below). Its function is to contain the space-charge. For the experiments with SF, in order not to obstruct path of the fragments, the beam dump can be rotated out of the beam axis. It is actuated manually through the beam window.

The beam dump is a cylindrical electrode with a diameter of 14 mm aligned with the beam axis and offset from a reaction target by 52 mm. Its function is two-fold. First, it stops the unreacted incident ion beam which would otherwise generate excessive ionization within the bulk of the stopping volume. Although it also blocks the reaction products emitted below 8°, the fraction of these products is minor compared to the total angular distribution, as shown in the simulations of the reaction kinematics [Spătaru et al., 2020, Dickel et al., 2017]. In fact, the result of these simulations were also used to optimize the geometry of the reaction module. Second, it pulls and neutralizes the ionization produced within the mini-cage. Otherwise, the charge will "leak" past the mini-cage into the stopping volume and will induce the space-charge effect (Section A.4). For this, a negative DC offset is applied to the beam dump relative to the mini-cage.

The rate capability of the INCREASE has been studied in simulations [Rotaru et al., 2022]. Geant4 [Agostinelli et al., 2003] has been used to calculate distribution of the charge in the system generated by the $^{238}U^{72+}$ primary beam with a Gaussian energy profile centered at $E_m = 12$ MeV/A with an RMS of $\sigma_E = 4$ MeV/A. The output of these calculations was used as an input for ion trajectories simulations in SIMION 8.1 where the leaked ions were counted as well as their neutralization time as a function of the generated space-charge density. The results of the simulations showed that a rate of primary beam of up to $9 \cdot 10^7$ ions/s can be tolerated assuming a standard rate capability of the prototype CSC.

The rate capability can be further improved by utilizing a shorter DC cage. The interplay between shorter distances, stronger electric fields and faster charge depletion has been explained in Section 4.2.2. The new DC cage has a length of ∼50 cm that is twice as short as the standard one. Although it reduces the maximum areal density to 4.5 mg/cm^2, it is sufficient to stop MNT reaction and SF fragments with energies of up to ∼1-2 MeV/u with high efficiency. Moreover, a shorter mean extraction time of <10 ms is expected.

The ring electrodes of the new DC cage have a 7% larger diameter and 40% finer length-to-diameter aspect ratio (pitch). The latter enables the transport of ions that are stopped closer to the DC cage rings by reducing the near-field distortions. Combined, these changes result in an increase of stopping efficiency by up to 30%.

From the radiation safety perspective, there exists a risk of contaminating the inside of the cold vacuum chamber. The worst-case contaminants are the fissioning nuclides that have self-sputtered from the source (e.g., a half-life of ^{248}Cm is $T_{1/2} = (348 \pm 6) \cdot 10^3$ years [Kondev et al., 2021]). In order to minimize this risk, an SF source is enclosed in the reaction module. In addition, it is made difficult for a contaminant to diffuse into the stopping volume: (i) the target wheel openings are blocked by reaction targets and Ti foils, and (ii) a groove at the edge of the

target wheel (Fig. 4.3b) and a matching tenon at the base electrode form a maze-like path which complicates the diffusion while still allowing for the rotation of the target wheel.

In addition, the reaction module accommodates two α-recoil sources. The sources are offset from the beam axis by 8.1 cm. The source holders are made backward-compatible with the standard DC cage.

Figure 4.3: Photographs of the INCREASE project at its various milestones. Please see text for details.

All components of the INCREASE have been selected to meet UHV- and cryogenic requirements. The constructing materials are 304L stainless steel and PPS. Special care has been taken when selecting bearings to support rotating parts. The INCREASE is equipped with xiros® A500 bearings by igus® inc. that are lubricant-free, bakeable and made of glass balls and a PEEK cage. A technical design of the INCREASE is described in more detail in [Rotaru et al., 2022].

The INCREASE has been developed in collaboration between:

- Justus-Liebig-Universität Gießen (JLU Gießen, Germany)
- Extreme Light Infrastructure – Nuclear Physics facility (ELI-NP, Romania)
- Tel Aviv University (TAU, Israel).

An initial technical design and production blueprints of the reaction module were developed at ELI-NP, and its components were manufactured at TAU. At JLU Gießen, (i) the new DC cage was designed and manufactured and (ii) all components of the INCREASE were cleaned, troubleshooted and assembled. During an initial assembly several critical issues were identified. The issues were troubleshooted, and the corresponding technical modifications were implemented in the first half of 2020 with interruptions caused by the COVID–19 pandemic. The modifications are documented in detail in [Gröf, 2020]. Additionally, the target wheel was equipped with the mini-cages, ball bearings and the cryogenic motor. The motor was characterized and programmed to switch remotely between the target positions. The complete reaction module was successfully tested in liquid nitrogen.

Various milestones of the project are shown in Figure 4.3: (a) the INCREASE assembled in JLU Gießen was transported to GSI where (b) the MNT reaction targets, produced by the GSI Target Laboratory and a ^{252}Cf SF source were installed; (c) the complete system was mounted inside the prototype CSC in place of the standard DC cage; (d) the (dis-)mounting of the SF source through the beam window was tested successfully; (e) A proper alignment with the beam axis was verified.

The INCREASE system is complete and ready to take the beam when the opportunity arises. A potential success of the MNT reaction studies with stable beams at the FRS-IC, followed up by studies with radioactive beams at the Super-FRS will contribute to a better understanding of the reaction mechanism and help to establish a new method of production of very heavy neutron-rich nuclei.

4.1.3 Commissioning: rate capability

The new (short) DC cage has been commissioned online separately from the reaction module during the S530 experiment, GSI beam time in 2021. A configuration of the prototype CSC with the short DC cage is aligned closely with the design concepts of the CSC for the Super-FRS described in Section 4.2. Therefore, the commissioning described below is simultaneously a test of the selected design concepts of the CSC. In this work, a dependence of ion extraction efficiency on the intensity of incident ions (i.e., the rate capability) has been investigated.

Previously, the rate capability of the prototype CSC with the standard (long) DC cage was investigated in a series of studies:

- In 2012 and 2014, the ions of ^{213}Fr and ^{221}Ac fragments were thermalized; short spills of 4–6 ms were used to simulate high beam intensities. It was shown that the extraction efficiency remained constant at beam intensities equivalent to up to $\sim 10^4$ ions/s, and decreased rapidly at higher intensities [Reiter et al., 2016].

- The simulation studies [Heiße, 2015] showed that the decrease of the efficiency can be attributed to the space-charge effect in the bulk of the stopping volume (Section A.4). This model was used to project the rate capability of the CSC for the Super-FRS (Section 4.2).

- In 2016, a primary beam of ^{238}U with a spill length of 1 second was thermalized. The beam intensity was scanned at three different RF voltages applied to the RF carpet of 94 V_{PP}, 40 V_{PP}, and 28 V_{PP}, corresponding to the ion transport efficiency of 100%, 100% and 40% respectively. It has been shown that the onset and the slope of the extraction efficiency trend are independent of the RF carpet setting [Miskun, 2019]. This result confirmed that the efficiency decrease is due to the space-charge in the bulk and not at the RF carpet or at the nozzle.

In 2021 (this work), a secondary ion beam of ^{235}U with a spill length of 5 s and 12 s was thermalized in the prototype CSC with the new (short) DC cage. A projectile fragmentation of ^{238}U primary beam at the energy of 1000 MeV/u in a beryllium target with the areal density of 0.66 g/cm^2 was utilized. The secondary beams were separated and identified in-flight at the FRS. After further slowing down at the final focal plane in the FRS-IC degrader system, the ions were injected in the prototype CSC. The prototype CSC was operated with the helium areal density of (1.09 ± 0.15) mg/cm^2 (*i.e.*, a pressure of (35 ± 5) mbar and a temperature of 75 K) and a DC push field of 30.4 V/cm. The RF carpet was operated with 100% ion transport efficiency.

The extraction efficiency was calculated as a ratio of the count rate of $^{235}UO^{2+}$ ions measured with the MR-TOF-MS and the count rate of incident ions measured with a plastic scintillator (SCI) mounted in front of the prototype CSC. The count rates were corrected for the duty cycle and dead time effects. In order to exclude the effects of stopping and transporting the ions from the prototype CSC to the MR-TOF-MS, the extraction efficiencies were normalized to the value measured at a beam rate of $2.2 \cdot 10^3$ ions/s. At this low rate, the space-charge effect is not prominent, and therefore a full extraction efficiency can be assumed.

Figure 4.4 shows a compilation of results obtained with the new (short) DC cage in this work and with the standard (long) DC cage in previous work. It can be seen that the rate capability is significantly higher with the new (short) DC cage. No loss of the extraction efficiency at the rates of the incident beam of up to $2 \cdot 10^5$ ions/s can be observed. Note that the higher beam intensities could not be tested as the radiation limit of the experimental area was reached. The improvement is due to the:

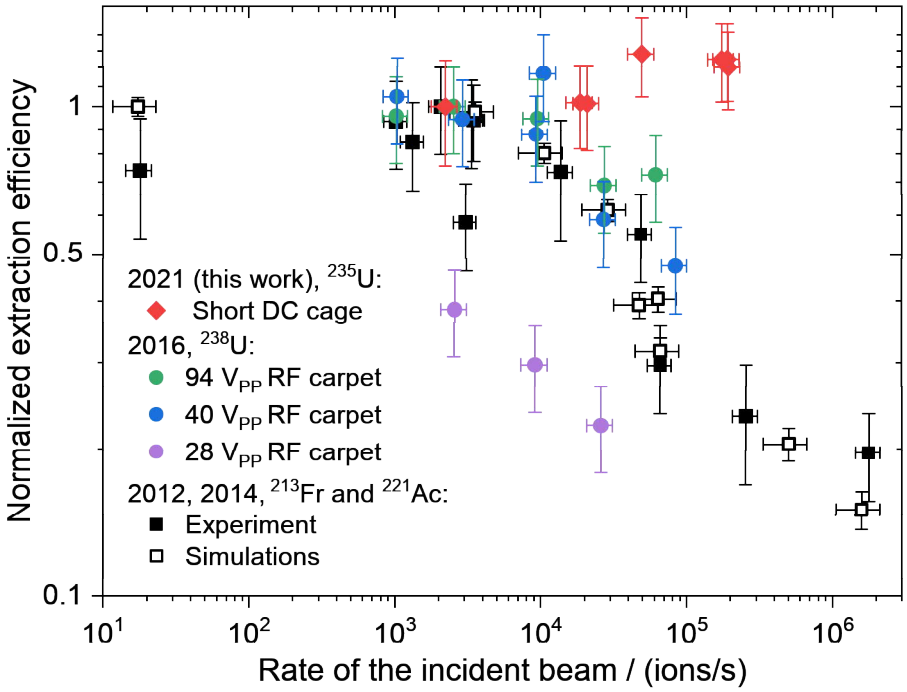

Figure 4.4: Normalized extraction efficiency as a function of the rate of the incident beam from experiments (filled symbols) and simulations (open symbols [Heiße, 2015]). The rate capability achieved in this work with the new (short) DC cage (diamonds) surpasses that of the standard (long) DC cage (squares [Reiter et al., 2016] and circles [Miskun, 2019]) by more than an order of magnitude. This result further supports the selected design concepts of the CSC for the Super-FRS (Section 4.2), as the prototype CSC with the short DC cage closely aligns with these concepts.

(i) smaller pitch design that reduces the near-field distortions and allows efficient transporting of the ions stopped closer to the electrodes

(ii) larger diameter of the DC cage which enlarges the stopping volume in radial direction

(iii) higher DC push field which leads to faster removal of the He ion-electron pairs

(iv) shorter length which shifts the distribution of stopped ions closer to the RF carpet, where the space-charge effect is weaker (Section A.4).

The new results complete the validation of the simulation model [Heiße, 2015], justify its use for the CSC for the Super-FRS and provide additional support for its selected design concepts outlined in Section 4.2.

4.2 Cryogenic stopping cell for the Super-FRS

A cryogenic stopping cell (CSC) for the Super-FRS will be a key device to enable mass, decay, and laser spectroscopy experiments. It will offer unique exper-

imental capabilities beyond mass measurements. A novel CSC concept has been proposed [Dickel et al., 2016] to achieve the unprecedented performance parameters.

As a part of this thesis, the CSC concept has been developed and evaluated in detailed simulations. This chapter formulates the requirements and design goals, presents and discusses the results of the simulations and summarizes the expected performance. Details on technical design of the CSC can be found in Appendix B.

4.2.1 Requirements, challenges and design goals

The FAIR facility is currently under construction at GSI in Darmstadt, Germany. Its scientific program aims to tackle numerous open questions in nuclear physics and related fields. Among its objectives is a research with exotic nuclei, addressing the structure and properties of atomic nuclei, the limits of their existence, the origin of the elements, and the role of nuclei in astrophysical events.

Central instrument in this program is the superconducting fragment separator (Super-FRS) [Geissel et al., 2003]. At the Super-FRS, the beams of exotic nuclei of all elements will be produced and separated in-flight (see Section 1.1.2). The production will occur with a primary beam accelerated to the magnetic rigidity of up to 20 Tm, corresponding to the relativistic energy of up to 1500 MeV/u for $^{238}U^{92+}$ which is unprecedented. This translates into higher intensity of secondary beam because of thicker production targets and more favorable kinematics. Moreover, a superior isotopical purity can be achieved at this energy because portion of ions that emerge fully-stripped is >90% even for the heaviest nuclei [Äystö et al., 2016]. The Super-FRS has a unique discovery potential for heavy radioactive beams (Z>70) at rates and purities not achievable elsewhere. It can act as a stand-alone spectrometer or be employed to deliver the beam to detector systems downstream.

A combination of the cryogenic stopping cell (CSC) and the multiple-reflection time-of-flight mass-spectrometer (MR-TOF-MS) is an example of such system. It will extend the experimental capabilities of the Super-FRS to studies of reactions with radioactive beams near the Coulomb barrier energies *e.g.*, multi-nucleon transfer (MNT) and fusion. These reactions might provide better access to neutron-rich heavy and super-heavy exotic nuclei essential for studying the nucleosynthesis r-process and the limits of nuclear stability. In addition, branching ratios of rare decay modes can be determined directly *e.g.*, β-delayed neutron emission probabilities. High-accuracy measurements of masses and isomer excitation energies will be carried out (Section 1.3). Moreover, it will be a tool for the absolute calibration of the particle identification (PID) of the Super-FRS which is indispensable *e.g.*, for the search of new isomers or studying the dependence of the isomer-to-ground-state ratios on the production mechanism. These experiments will be pursued by the Super-FRS Experiment Collaboration [Äystö et al., 2016]

At the low-energy branch (LEB) of the Super-FRS, the CSC will be a key device to enable the scientific program of several collaborations:

- MATS – precise Measurements on very short-lived nuclei using an Advanced Trapping System for highly charged ions [Rodriguez, 2013]

- LaSpec – Laser Spectroscopy of short-lived nuclei at FAIR [Nörtershäuser and Campbell, 2006]

The experimental techniques of MATS collaboration include high-accuracy mass measurements, in-trap conversion electron- and alpha-spectroscopy, and trap-assisted spectroscopy. The LaSpec collaboration will apply collinear laser spectroscopy on ions and atoms, and β-detected nuclear magnetic resonance (β-NMR) experimental techniques.

A fast and efficient conversion of intense RIB produced at relativistic energies into low-energy and low-emittance beams is a prerequisite for these experiments. Performance parameters of the CSC will have a strong impact on a variety of isotopes and isomers available for experiments and their yields.

Efficient stopping of relativistic ions is a challenging task, as explained in Section 1.2. The areal density of the CSC of > 20 mg/cm^2 is required.

Ion extraction efficiency has to be maximized for ions of all chemical elements to take advantage of universality of in-flight technique (Section 1.1.2). Moreover, it has to be similar for all ions of interest stopped everywhere throughout the CSC. This efficiency includes ion losses due to neutralization, chemical reactions, and improper transport along the RF carpets. Based on the experience gained with the prototype CSC, the extraction efficiency of $\geqslant$50% is achievable [Plaß et al., 2019].

The extraction time of ions from the CSC limits the accessible lifetimes of nuclides and isomers to be studied. Thus, it has to be comparable or shorter than the typical duration of measurements of the experiments downstream *e.g.*, cooling and preparation cycles of ion traps which are typically of $\sim$10 ms.

The requirements for the rate capability of the CSC are matched to the beam intensity expected at the output of the Super-FRS. The expected intensities were simulated in LISE++ [Tarasov and Bazin, 2008] and are shown in Figure 4.5 [Pietri, 2023]. The simulation considers the primary beam of ^{238}U with the highest planned energy and intensity of 1500 MeV/u and $3 \cdot 10^{11}$ pps incident on the ^{9}Be target with a thickness of 4 g/cm^2. The intensity in the most intense cases reaches up to 10^9 ions/s. Such intensities are several orders of magnitude higher compared to what is currently available at GSI.

Moreover, at the LEB, for the LaSpec experiments up to 10^4 ions of interest (IOI) per second have to be delivered from the CSC. For this the CSC has to handle incoming beam of up to three orders of magnitude higher rate, because (i) the fraction of IOI may constitute only $\sim$1% of beam composition and (ii) the combined stopping, extraction and transport efficiencies of the CSC of $\sim$25% are expected.

Considering all of the above, the rate capability of $\geqslant 10^7$ ions/s is therefore required.

In addition, an active area of the CSC of at least 300$\times$200 mm (width$\times$height) is required in order to accept a large beam spot of the Super-FRS. In addition, the mass of the CSC should stay below 5 tons for it to be movable in case the laboratory space has to be rearranged for other experimental setups to fit in.

It has been shown in Section 1.2 that no existing stopping cell is able to satisfy the aforementioned requirements simultaneously. Besides, the design goals cannot be achieved by up- or down-scaling the existing gas cells. Table 4.1 summarizes the design goals of the CSC.

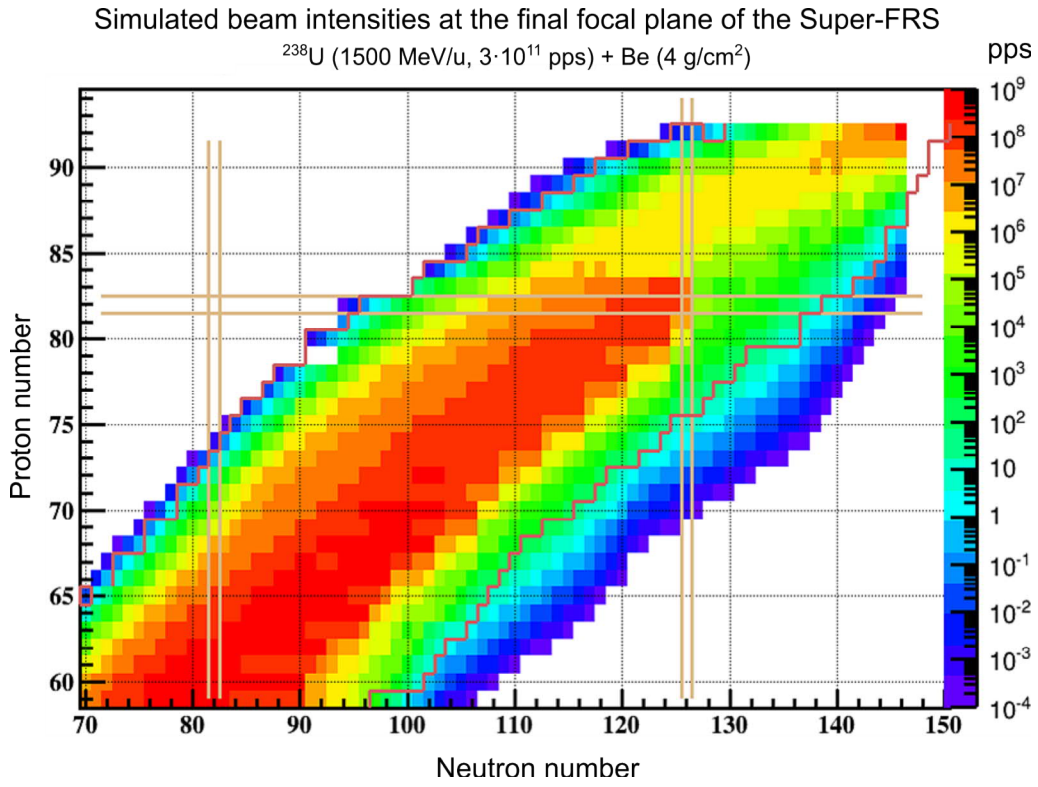

Figure 4.5: Simulated intensities of secondary beams expected at the final focal plane of the Super-FRS. The simulations consider primary beam of ^{238}U at the energy of 1500 MeV/u and a maximum intensity of $3 \cdot 10^{11}$ particles per spill (pps) on a beryllium target with a thickness of 4 g/cm^2 [Pietri, 2023].

4.2.2 Conceptual design

In order to achieve the unprecedented performance parameters, a novel CSC concept has been proposed [Dickel et al., 2014]. A schematic layout of the CSC is shown in Fig.4.6.

The CSC consists of two main vacuum chambers. An outer chamber provides a thermal insulation vacuum for an inner chamber which is operated at cryogenic temperature. The inner chamber is split into a high-density stopping region and a low-density extraction region. A high-energy beam enters the stopping region horizontally through the two beam windows on the outer and inner chambers. The stopped ions are guided orthogonally to the beam axis by a homogeneous DC field towards a first-stage RF carpet. At the RF carpet, ions are guided towards multiple nozzles and are taken by the gas flow to the extraction region. At the extraction region, a second-stage RF carpet transports and focuses ions at the exit nozzle where they are eventually extracted from the CSC. The extracted ions are separated from gas and transported to the experiments further downstream via an RF quadrupole ion guide. The unstopped part of the beam exits the CSC via two additional beam windows installed on the inner and outer chambers.

The proposed concept introduces several novel solutions:

- **Orthogonal ion extraction.** The direction of ion extraction is orthogonal to

Table 4.1: Design goals for the CSC at the LEB of the Super-FRS at FAIR. No existing stopping cell is able to meet these goals simultaneously.

Parameter	Design goal
Areal density	> 20 mg/cm^2
Extraction efficiency	$\geqslant$50%
Mean extraction time	$\sim$10 ms
Rate capability	$\geqslant 10^7$ ions/s

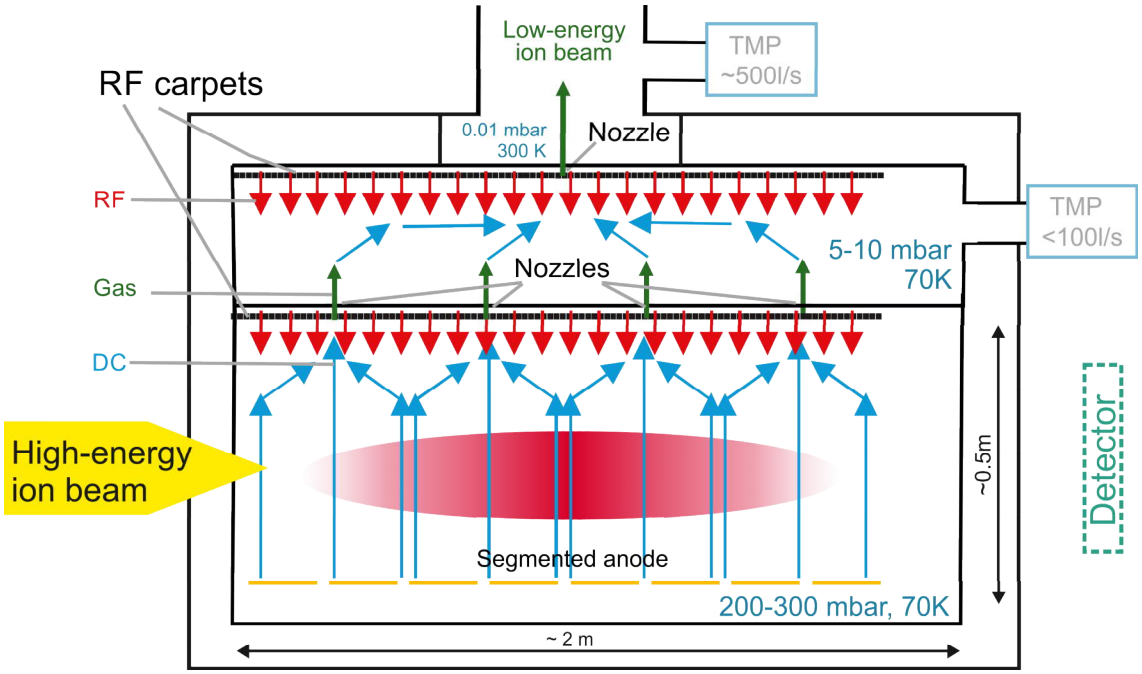

Figure 4.6: A schematic layout of the novel CSC concept. Please see text for the details.

the axis of the incoming beam throughout the entire stopping volume.

- **Two-stage extraction.** The stopped ions are first extracted from the high-density stopping to the low-density extraction region, and then from the extraction region to the RFQ ion guide.
- **Extraction via multiple nozzles.** At the first stage, the ions are extracted simultaneously through several nozzles.
- **Segmented anode.** In the stopping region, an electrode opposite to the first-stage RF carpet is segmented and coarsely repeats the structure of the RF carpet electrodes.
- **Transparent CSC.** With the beam windows at the entrance and exit of the vacuum chambers, it becomes possible to conduct a parasitic experiment in parallel to the CSC (*e.g.*, decay spectroscopy) and vice versa. Moreover, a

particle detector can be placed on the beam path behind the CSC for identification and counting of the unstopped beam. This will simplify the tuning procedure for the range of the ions of interest.

Other solutions are based on techniques which have been learned and proven to be successful from the prototype CSC at the FRS Ion Catcher at GSI (Section 2.1.2) and other stopping cells (Section 1.2):

- **Operation at cryogenic temperature.** Cold chamber and buffer gas are kept at ∼70 K.
- **High-electrode-density RF carpet (first-stage).** An RF carpet with finely-spaced electrodes is placed at the stopping region where the buffer gas density is high.
- **Traveling wave ion transport technique (second-stage).** In the extraction region at low gas density this technique enables faster ions transport.

The following describes qualitatively the way proposed solutions allow achieving the design goals. The quantitative results can be found in Section 4.2.3.

Short mean extraction time: the voltage is limited at the operating pressure of the CSC due to breakdown given by the Paschen's law [Paschen, 1889]. Because of the orthogonal extraction, the distance between the RF carpet and the anode is shorter which results in a stronger pushing DC field for a given voltage. This translates into faster ion motion (see Eq. A.13).

The two-stage extraction enables the differential pumping between the stopping and extraction regions. This makes it possible to increase the number of nozzles at the first-stage RF carpet, which in turn reduces the average distance ions travel at the RF carpet before reaching a nozzle.

The differential pumping allows operating the extraction region at low pressure, and thus to implement a traveling wave technique at the second-stage RF carpet. This technique enables ion transport velocities in the order of few 100 m/s [Bollen, 2011, Lund et al., 2020] *i.e.*, about 10 times higher than conventional technique. With the length of the CSC of 2 m (see below), the average distance ions travel at the second-stage RF carpet is 0.5 m which results in transport time of about few ms.

Furthermore, a low pressure in the extraction region does not require the second-stage RF carpet to have high electrode density. Efficient transport can be achieved with the density of 2 electrodes/mm.

High rate capability: it has been shown [Reiter et al., 2016] that in a stopping cell with a linear extraction layout, the ions stopped closer to the RF carpet are extracted successfully while the ones stopped further away are deflected and lost on the electrodes due to the space-charge effect in the bulk of the stopping volume (see Section A.4). In the orthogonal extraction layout, (i) the portion of ions stopped close to the RF carpet is larger, and (ii) the ratio of area covered by the RF carpet to the stopping volume is larger. The orders of magnitude stronger ionization density is required to deflect the ions past the RF carpet, hence the high rate capability.

Solution	High areal density	Short mean extraction time	High rate capability	High extraction efficiency
Orthogonal ion extraction		■	■	■
Two-stage extraction	■	■		
High-electrode-density RF carpet (first-stage)	■			
Extraction via multiple nozzles		■		■
Operation at cryogenic temperature			■	■
Traveling wave ion transport technique (second-stage)		■		■
Segmented anode	■			
Transparent CSC				

Figure 4.7: The contribution of the proposed solutions to the CSC design goals. The novel solutions are highlighted in bold. Although the "Transparent CSC" feature does not impact the performance parameters of the CSC, it expands its experimental flexibility and beam diagnostics capabilities.

The operation at cryogenic temperature plays a crucial role at high beam intensities as it minimizes the space-charge effect at the extraction nozzle of an RF carpet (see Section A.4).

High areal density: the differential pumping provided by the two-stage extraction makes operating the stopping region at a higher buffer gas density possible from technical point of view.

From the operational point of view, an RF carpet with high electrode density is what enables ion transport at high areal density (Eq. A.17).

The segmented anode allows to achieve a uniform DC pushing field across the complete RF carpet, thereby reducing the maximal pushing field the ions are experiencing. This allows to transport ions of a given mass-over-charge ratio at a lower RF amplitude. Alternatively, the ions with lower mass-over-charge ratios can be transported at a given amplitude.

High extraction efficiency: at cryogenic temperature the concentration of impurities in the buffer gas becomes ultra-low, which plays a crucial role in reducing the losses of ions associated with chemical reactions and neutralization. As demonstrated with the prototype CSC, the extraction efficiency is essentially element-independent [Plaß et al., 2019].

Because of fast ion extraction, ions spend less time interacting with impurities in the buffer gas. This further reduces the losses.

The trajectories of ions stopped throughout the entire stopping volume become similar to each other because of the multiple nozzles. This feature is of a high importance because the extraction efficiency becomes more consistent for all stopped ions.

The contribution of the proposed solutions to the design goals is summarized in Figure 4.7.

Further advantages: the proposed CSC concept will result in a length-independent performance. The length of the CSC along the high-energy beam

axis can be up- or downsized without affecting the mean extraction time, rate capability and extraction efficiency. Although the mean extraction time depends on the distance ions travel at the RF carpet in the extraction region, the velocities offered by the traveling wave technique make this dependence weak.

The electron current produced during the stopping process can be measured at the segmented anode. The segmentation allows resolving the stopping position of ions along the beam axis. This *e.g.*, simplifies the optimization of the momentum compression settings upstream the CSC.

Although the "Transparent CSC" feature does not impact the performance parameters of the CSC, it expands its experimental flexibility and beam diagnostics capabilities.

4.2.3 Numerical simulations

DC cage and the rate capability

The length of the stopping volume along the beam axis and thus the DC cage of 2 m has been selected. Considering the optimal mass-over-charge transport, electrode density and effective field of the first-stage RF carpet deduced in the Section 4.2.3, the areal density of 28 mg/cm^2 was decided. Combining the length, areal density and the temperature of 70 K – as in the prototype CSC – the pressure in the stopping region of 200 mbar was deduced.

The expected rate capability was investigated in [Heiße, 2015]. In order to study the ion extraction efficiency dependence on the rate of incoming beam, the ion trajectories in the DC cage were calculated using SIMION 8.1 software. The simulations take into account electric fields applied externally (resulting from the voltages applied to the DC cage electrodes), the electric fields induced by the ions (*i.e.*, space-charge field), ion mobility and diffusion in the gas. The initial spatial distribution of stopped ions and ionization in the buffer gas was obtained using MOCADI [Iwasa et al., 1997] and SRIM [Ziegler et al., 2010]. Ions were treated as successfully extracted once reached the RF carpet.

The model output was validated against the experimental results obtained with the prototype CSC in two experiments: (i) short spills of (4–6) ms of ^{221}Ac and ^{213}Fr ions in a broad range of equivalent rates of 10–$2 \cdot 10^6$ ions/s [Reiter et al., 2016] and (ii) long spills of 1 s of ^{235}U ions incoming at the rates of 10^3–10^5 ions/s [Miskun, 2019]. A good agreement was shown – the onset and the slope of the efficiency decrease at 10^4 ions/s were reproduced correctly (Section 4.1.3).

The model could be reliably applied to the CSC of the Super-FRS. The results showed a constant extraction efficiency at the beam rates of up to 10^7 ions/s. Even at the rate of 10^9 ions/s, the extraction efficiency still remained on the level of (50–65)%. For comparison, an equivalent increase of the beam rate in the prototype CSC – from 10^4 ions/s to 10^6 ions/s – leads to the efficiency decrease of more than 80%.

Parameters of the RF carpets

The simulations of ion transport at the RF carpets of the stopping and extraction regions were performed in order to deduce their parameters and project their performance under challenging conditions of the CSC.

The ion trajectory simulation program ITSIM 6.0 [Plaß, 2001, Wu et al., 2006, Plaß et al., 2008b] was used for this purpose. The ITSIM software calculates trajectories of ions in an arbitrary geometry taking into account interactions with electric fields and gas. The electric fields are calculated externally in SIMION 8.1. Similarly, external solvers are used to provide information about the gas parameters *i.e.*, pressure, temperature, velocity distributions. Stationary and uniform gas pressure arrays can be generated internally. To simulate ion-neutral elastic collisions, built-in microscopic and macroscopic collision models can be used.

The simulations were first validated against experimental results obtained with the prototype CSC. Transmission efficiency of $^{219}Rn^{+}$ ions transported onto and along the RF carpet was measured scanning the RF amplitude. The measurements were carried out for a range of DC push fields and volumetric gas densities of up to 72 V/cm and $\sim$50 μg/cm^3 ($\sim$ 10 mg/cm^2 areal density equivalent) correspondingly. The measurement results were fitted [Rink, 2017], and performance under conditions of the CSC for the Super-FRS was derived. The experimental and simulated RF amplitudes required to achieve transmission efficiency of 50% were compared. The results showed a good agreement in a broad range of DC push fields and areal densities of 20–100 V/cm and 2.8–28 mg/cm^2 (pressure of 20–200 mbar) correspondingly. The agreement was achieved for both microscopic and macroscopic collision models. As the latter model is computationally more efficient, it was used in all further simulations.

After a successful validation, the model was used to optimize an RF frequency. Three sets of buffer gas pressures and DC push fields were considered:

a) 14 mg/cm^2 (100 mbar or 69 μg/cm^3) and 50 V/cm

b) 28 mg/cm^2 (200 mbar or 137 μg/cm^3) and 100 V/cm

c) 41 mg/cm^2 (300 mbar or 206 μg/cm^3) and 150 V/cm

The DC push field was scaled with pressure according to Eq. A.13 in order to keep the ions transport time constant. The conditions above correspond to $\sim$10 ms mean extraction time. The following parameters were fixed in the model: RF carpet electrodes density of 6 electrodes/mm, RF amplitude of 150 Vpp, helium buffer gas at a temperature of 70 K, and reduced ion mobility of 17.5 cm^2/(V $\cdot$ s). Here and below, the inner layer was not considered in the simulations because its effect is weak at high gas density [Rink, 2017].

The results of the simulations are shown in Figure 4.8. Transmission efficiency of ions ranging from 10 u/e to 200 u/e as a function of RF frequency is color-coded, where red corresponds to full transmission, and white – to complete loss of ions. In all three cases, an efficient ion transport is possible once a certain RF frequency threshold is reached. The threshold is mass-dependent – lighter ions require larger RF frequency. This dependence is emphasized at higher pressure. Clearly, the RF frequency of 15 MHz is optimal for ion transport in all studied cases.

A cutoff in transporting low-mass ions exists. High pressure and strong DC push field weaken effective field of the RF carpet. The effective field remains strong enough to transport heavier ions but is too weak to transport lighter ones. The low-mass cutoff scales with pressure and DC field as $m/q \propto (P^2 \cdot E)$ which is in agreement with Eq. A.17.

Three operation modes of the CSC can be outlined based on the simulation results. *Low-mass mode*: 14 mg/cm^2 (100 mbar) and 50 V/cm, shown in Fig. 4.8a. The ions with the mass-over-charge ratio of down to ∼10 u/e can be transported. Note that at cryogenic temperatures, the molecules of buffer gas He are ionized as trimers He_3^+ with $m/q = 12$ u/e. They carry most of the charge created in the stopping process. Under given conditions, the ions of He_3^+ will be effectively transported by the RF carpet, and therefore will induce space-charge effect at the nozzle (Section A.4). Their transport has to be suppressed by moderating the conditions. Therefore the conditions of the low-mass mode are for the guidance only. In addition, since the range straggling of light ions is larger (Eq. A.5), this mode comes at the expense of reduced stopping efficiency.

Standard operation mode: 28 mg/cm^2 (200 mbar) and 100 V/cm, shown in Fig. 4.8b. Fast and efficient ion extraction at high areal density can be achieved simultaneously for an optimal range of masses.

Heavy-mass mode: 41 mg/cm^2 (300 mbar) and 150 V/cm, shown in Fig. 4.8c. It can be seen that only the ions with $m/q \gtrsim$190 u/e can be transported. The very high areal density of this mode is excessive for efficient stopping of heavy ions because their range straggling is small. However, it is beneficial *e.g.*, for in-cell reaction or decay studies.

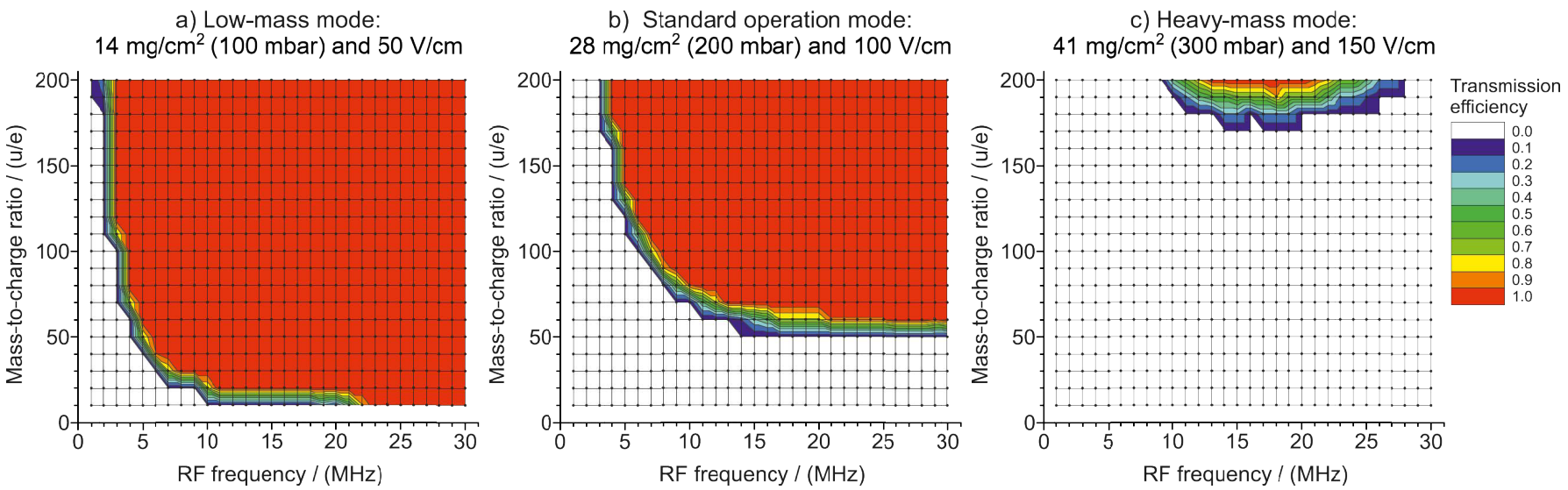

Figure 4.8: Simulated transmission efficiency of an RF carpet as a function of ion mass-over-charge ratio and RF frequency. The simulations represent (a) low-mass mode: 14 mg/cm^2 (100 mbar) and 50 V/cm, (b) standard operation mode: 28 mg/cm^2 (200 mbar) and 100 V/cm, and (c) heavy-mass mode: 41 mg/cm^2 (300 mbar) and 150 V/cm. These conditions correspond to the mean extraction time of 10 ms. The RF carpet fixed parameters are electrode density of 6 electrodes/mm, and RF amplitude of 150 Vpp. Results show that the RF frequency of 15 MHz is optimal for ion transport in all studied cases.

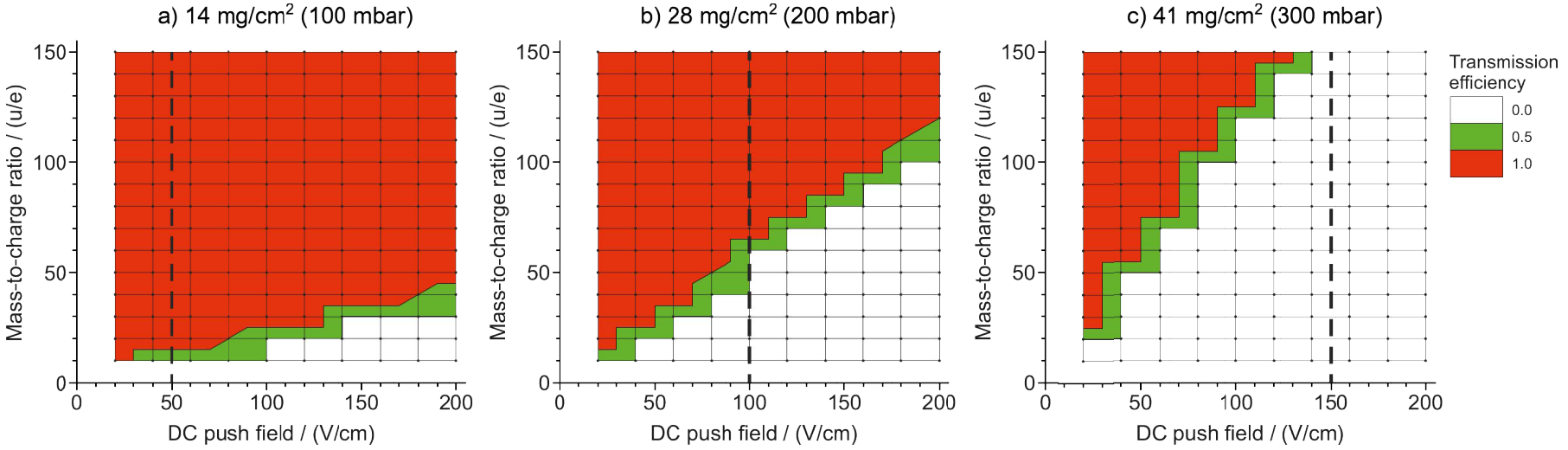

Figure 4.9: Simulated transmission efficiency of an RF carpet as a function of ion mass-over-charge ratio and DC push field. The simulations consider the areal density of (a) 14 mg/cm^2 (100 mbar), (b) 28 mg/cm^2 (200 mbar), and (c) 41 mg/cm^2 (300 mbar), corresponding to low-mass, standard and heavy-mass operation modes accordingly. Dashed vertical lines indicate the optimum DC push field which corresponds to the mean extraction time of 10 ms. The RF carpet fixed parameters are the RF frequency of 15 MHz, the electrode density of 6 electrodes/mm, and the RF amplitude of 150 Vpp. The results show that a reasonable trade-off between areal density, extraction time and rate capability can be found by tuning the areal density and/or DC push field in case the optimal setting does not yield efficient transport of ions of interest.

The effect of DC push field on ion transmission was studied at the next step. The DC push field was scanned from 20 V/cm to 200 V/cm for ions in the range of 10–150 u/e mass-over-charge ratios. The simulations were performed for the same buffer gas conditions as above – 14 mg/cm^2, 28 mg/cm^2, and 41 mg/cm^2 at 70 K. The RF frequency was fixed at 15 MHz. Other fixed parameters are identical to the simulations described above. The results are shown in Fig. 4.9. The ion transmission efficiency is color-coded, the dashed vertical lines indicate the optimum DC push field that corresponds to ∼10 ms mean extraction time. In all cases, DC push field stronger than optimum elevates the low-mass cutoff and vice versa. The dependence is linear and in agreement with Eq. A.17. Most importantly, the results show that a reasonable trade-off between stopping efficiency and extraction time can be found by tuning the areal density and/or DC push field. For instance, faster ion extraction can be achieved by applying stronger DC push field, however, at the expense of not transporting low-mass ions. In case the maximum stopping efficiency for low-mass ions is of interest, a combination of high pressure and low DC push field can be applied at the cost of increased extraction time. Such flexibility in operation parameters makes it possible to employ the CSC in experiments with nuclei across a broad region of the nuclide chart, and to meet a wide variety of requirements.

Similar investigations were performed for an RF carpet which will be installed at the extraction region – the second-stage RF carpet. It has been found out that an electrode density of 2 electrodes/mm and an RF frequency of 3 MHz will be optimal to effectively transport ions in helium at the volumetric density of 2–7 μg/cm^3 (3–10 mbar at 70 K).

Simulations of the two-stage ion extraction

The simulations above considered uniform and static pressure of the buffer gas. The ions were assumed to be successfully extracted once reached a vicinity of a nozzle. The assumption has been proven reasonable in case of one-stage extraction. However, in the CSC for the Super-FRS a two-stage ion extraction – a novel concept – will be implemented for the first time. The concept is illustrated schematically in Figure 4.10. In this concept, the gas flow plays important role because it impacts all aspects of ion transport from a nozzle of the 1st-stage RF carpet to the extraction nozzle of the 2nd-stage RF carpet. These aspects have been investigated in simulations which consider gas flow.

The ITSIM model was coupled to a gas flow array which was obtained with the ANSYS® Fluent fluid simulations software [ANSYS Fluent,]. A gas flow between two regions at 200 mbar and 3 mbar at a temperature of 75 K through a nozzle in shape of a cylindrical hole of 0.6 mm diameter and 1.6 mm length was considered. The distance from the nozzle to an upper boundary of the low-pressure region is 100 mm. This corresponds to the distance from a nozzle of the first-stage RF carpet to the surface of the second-stage RF carpet. Similar gas flow arrays were computed for the nozzles with diameters of 0.4 mm and 0.3 mm.

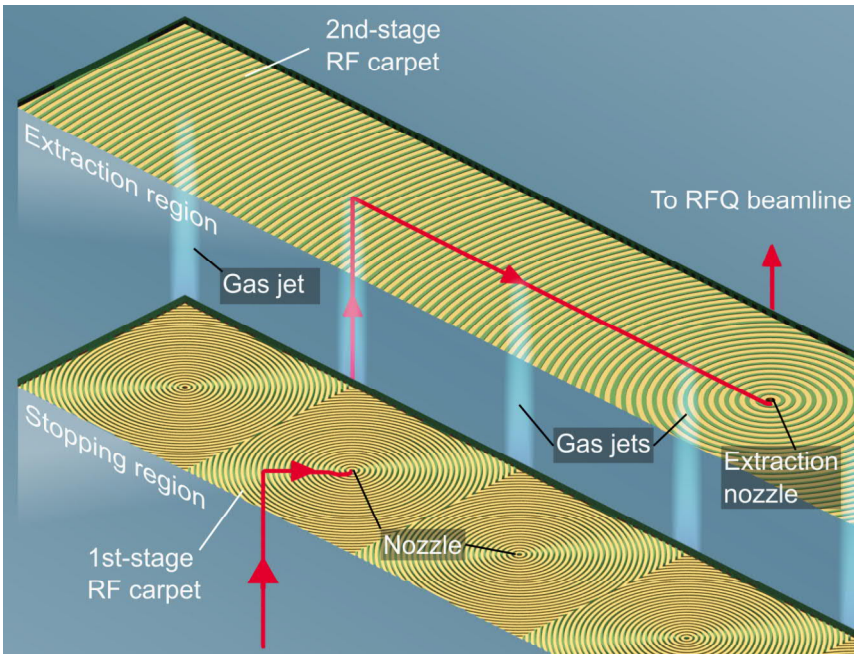

Figure 4.10: Schematic representation of a two-stage extraction concept. Red curve indicates a typical ion path. The ions are extracted through a nozzle of the 1st-stage RF carpet, jetted onto the 2nd-stage RF carpet, focused at the extraction nozzle and are eventually extracted. At the 2nd-stage RF carpet, ions cross one or several gas jets. The dimensions are not to scale.

The ion extraction through the nozzle of the 1st-stage RF carpet

First, the ion extraction through the nozzle of the first-stage RF carpet by the gas flow was simulated. A DC potential applied to the nozzle electrode was scanned to optimize the extraction efficiency. Ions were considered successfully extracted once they reach a virtual detector placed on the *opposite* side of the RF carpet at the nozzle. The following parameters were fixed in the ITSIM model: ions with mass-over-charge of 219 u/e, RF carpet electrode density of 6 electrodes/mm, RF amplitude of 150 Vpp, RF frequency of 15 MHz, DC push field of 100 V/cm and DC field along the RF carpet electrodes of 20 V/cm.

Figure 4.11 shows the status of ions as a function of the DC offset potential applied to the nozzle electrode. The results are shown for the nozzles with diameters of 0.3 mm (top panel), 0.4 mm (middle panel), and 0.6 mm (bottom panel). When no DC offset is applied, the ions are either extracted (blue) or lost because they hit the nozzle electrode (green). No potential trap is formed, and therefore no ions are stored at the RF carpet (red). As the offset potential increases, fewer ions are lost at the nozzle, no ions are stored, and thus the fraction of extracted ions peaks at ∼100%. Once a threshold offset is reached, the potential trap becomes strong enough to counteract gas flow – the ions are stored and cannot be extracted.

According to the simulations, before traveling through the nozzle ions overcome a shallow trap formed there by a low DC offset potential, and end up being concentrated closer to the nozzle axis and further from its walls. This results in

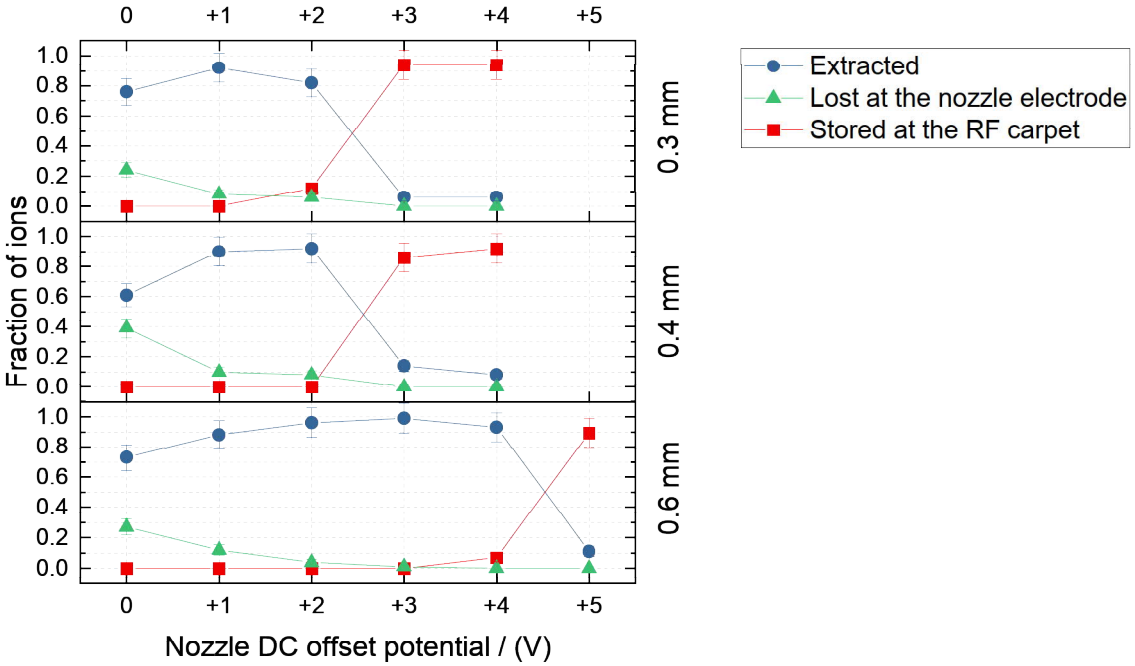

Figure 4.11: Simulated status of ions as a function of the DC offset potential applied to a nozzle electrode of the 1st-stage RF carpet for the nozzles diameters of 0.3 mm (top), 0.4 mm (middle), and 0.6 mm (bottom). Color-coded is the fraction of ions that are extracted (blue), lost at the nozzle electrode (green) or stored at the RF carpet (red).

fewer ions hitting the nozzle electrode when traveling through, and thus improved extraction efficiency. This behavior is consistent with experimental observations at the prototype CSC. The optimum and trapping offset potentials are diameter-dependent. The dependence seems linear but a broader parameter space has to be probed with finer steps in order to characterize it properly.

Most importantly, the simulations predict that RF carpets which have a diameter of the nozzle smaller than 0.6 mm can achieve equally high extraction efficiency. Smaller nozzle is advantageous since it improves differential pumping. Therefore either (a) more nozzles can be introduced between the stopping and extraction regions which reduces the mean extraction time, or (b) higher areal density can be reached for a given number of nozzles. Furthermore, it reduces the gas consumption quadratically, and thus the heat input to the system which is important for the cryogenic operation. For the RF carpets at the CSC for the Super-FRS, the nozzles with the diameter of 0.6 mm are considered because this has been proven to work at the prototype CSC. Later, when tested experimentally, smaller nozzles could be an upgrade of the CSC.

The manipulation of ions in the extraction region

At the next step, the ability to manipulate ions in the extraction region by DC field was studied in simulations. The ions were sent onto the second-stage RF carpet in a gas jet. A DC field along the RF carpet was applied in order to separate them from the gas jet and guide in a preferred direction. The DC field instead of

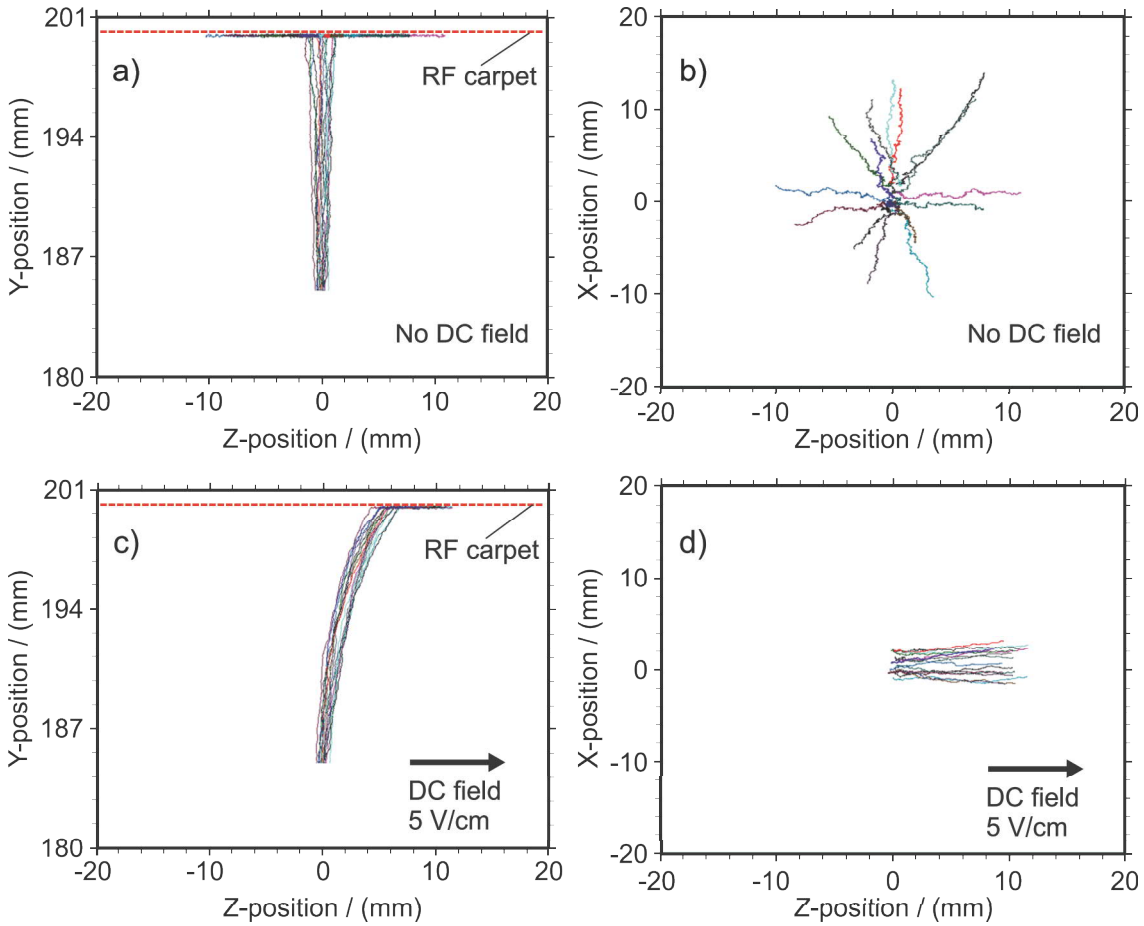

Figure 4.12: Simulated ion trajectories in the extraction region. Panels a) and b) represent the case when no DC field along the RF carpet electrodes is applied. Ions travel in planes orthogonal (a)) and parallel (b)) to the RF carpet. Similarly, panels c) and d) demonstrate the case when DC field of 5 V/cm is applied. The red dashed line indicates RF carpet electrodes (not to scale). For the details please see text.

traveling wave was applied in order to reduce the parameter space of the model. The following parameters were fixed in the ITSIM model: ions with mass-over-charge of 219 u/e, RF carpet electrode density of 2 electrodes/mm, RF amplitude of 50 Vpp, RF frequency of 3 MHz, DC push field of 5 V/cm.

Typical results of the simulations for the nozzle with diameter of 0.6 mm are shown in Figure 4.12. Panels a) and b) show ion trajectories in case no DC field *along* the RF carpet electrodes is applied. Ions travel in planes orthogonal (a)) and parallel (b)) to the RF carpet. Similarly, panels c) and d) demonstrate the case when DC field of 5 V/cm is applied.

When no DC field is applied ions are guided radially outwards in arbitrary directions once reached the RF carpet. This motion is due to ions following the natural gas flow path. In case DC field of 5 V/cm is applied along the RF carpet electrodes, all ions are separated from the gas jet and guided in a preferred direction. The results indicate that ion motion in the extraction region can be controlled sufficiently by DC field along the second-stage RF carpet electrodes. Given that the ef-

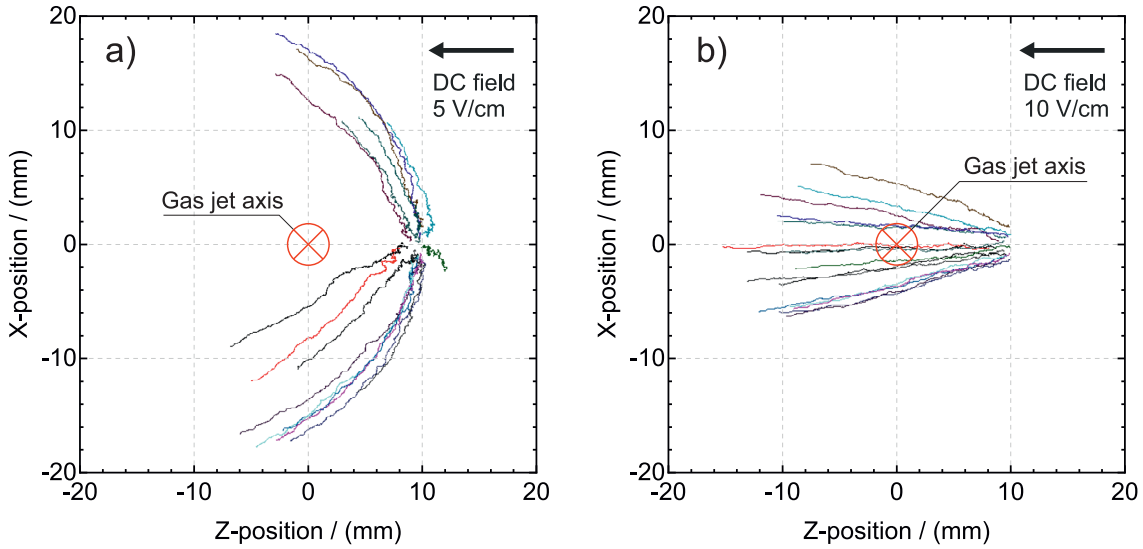

Figure 4.13: Simulated trajectories of ions traveling across a gas jet in the extraction region. The ions are guided along an RF carpet by DC field of 5 V/cm (a) and 10 V/cm (b). The gas jet axis is perpendicular to the plane of the plots; its position is indicated by a red circle over cross. Note that the model considers an RF carpet with parallel strip electrodes.

fect of traveling wave is comparable to the DC field of ∼100 V/cm [Bollen, 2011], achieving effective ion manipulation with weaker fields strongly indicates the viability of utilizing traveling wave technique.

Transporting ions through the gas jets in the extraction region

Ions traveling at the second-stage RF carpet cross one or several gas jets formed by the nozzles of the first-stage RF carpet. These gas jets might be a considerable obstacle for the ions on their way to extraction nozzle. The influence of gas jets on ion transport was studied in simulations. Ions were generated 10 mm off the gas jet axis, and guided along the RF carpet by a corresponding DC field across the gas jet. The following model parameters were fixed: ions with mass-over-charge of 219 u/e, RF carpet electrode density of 2 electrodes/mm, RF amplitude of 50 Vpp, RF frequency of 3 MHz, DC push field of 5 V/cm.

Typical results of the simulations shown in Figure 4.13 indicate that although the gas jet does not forbid ion transport in a preferred direction, it defocuses ions. Higher DC field along the RF carpet electrodes help reducing the spread of ions *e.g.*, from about ±20 mm at 5 V/cm (Fig. 4.13a) to about ±10 mm at 10 V/cm (Fig. 4.13b). Nevertheless, an additional refocusing is required in order to reduce the spread of ions before they reach extraction nozzle. Note that the model considers an RF carpet with parallel strip electrodes. Using an RF carpet with concentric ring electrodes as shown in Fig. 4.10 will allow to refocus ions automatically. Such geometry is considered for the second-stage RF carpet of the CSC.

Mean extraction time

Another important finding of the simulations above is that the velocity of ion transport along an RF carpet is the same as when traveling in the bulk of the gas (Section A.2). Therefore Eq. A.13 can be used to calculate the duration of ion transport at each consecutive stage towards extraction (Fig. 4.10). The cumulative result of these calculations yields the mean extraction time, shown in Table 4.2. The following assumptions were made:

(1) The starting positions of the stopped ions are uniformly distributed across the stopping region. Therefore the average distance the ions travel towards 1st-stage RF carpet is half of the height of the stopping region that is 30/2 = 15 cm. Pressure of 200 mbar, temperature of 70 K, and DC push field of E = 100 V/cm corresponding to the *standard operation mode* are assumed.

(2) The 1st-stage RF carpet consists of 8 square-shaped segments arranged consecutively. Each segment has a length of L = 25 cm, and has a nozzle at the center. From (1) it follows that the ions are uniformly distributed across the area of a segment. The average distance d from the center of a square with length L to a point selected uniformly over its area is [Stone, 1991]:

$$d = \frac{L}{6}\left(\ln(1+\sqrt{2}) + \sqrt{2}\right).$$

For L=25 cm, the average distance ions travel towards a nozzle is d = 9.6 cm.

(3) The ions are transported to the 2nd-stage RF carpet by a gas jet. The average velocity along the jet axis of v=360 m/s was obtained from the gas flow array described in Section 4.2.3. The distance between the two RF carpets is 10 cm.

(4) The 2nd-stage RF carpet operates in the extraction region at a pressure of 10 mbar. It employs the traveling wave technique. The velocity enabled by this technique varies – a value of 100 m/s has been achieved experimentally [Lund et al., 2020] whereas theoretical velocities of >200 m/s have been predicted [Bollen, 2011]. The RF carpet is a rectangle with the dimensions of 200×25 cm (L×W), and the extraction nozzle at the center. Unlike in (2), the ions are not uniformly distributed across the carpet. Their starting positions are clustered on both sides of the nozzle along a line passing through the center of the rectangle along its long side. The average distance from the clusters to the extraction nozzle is 50 cm.

Importantly, the calculations show that the mean extraction time can meet the requirements simultaneously with other operational parameters. Furthermore, it can be reduced to <10 ms *e.g.*, by injecting the ions closer to the 1st-stage RF carpet at the expense of stopping efficiency.

4.2.4 Expected performance

The expected performance of the CSC for the Super-FRS at FAIR is summarized in Table 4.3. These values have been derived from the results of the simulations

Table 4.2: Calculated mean travel time of stopped ions at consecutive stages towards extraction. The cumulative result is the mean extraction time. The conditions assumed at each stage are given. The velocities achieved with traveling wave technique vary in literature, therefore the range of values is given. The resulting mean extraction time meets the requirements simultaneously with other operational parameters. Please see text for details.

#.	From	To	Driving force	Pressure P, mbar	Electric field E_{DC}, V/cm	Avg. distance d, cm	Velocity v, m/s	Time t, ms
1.	Stopping region	1^{st}-stage RF carpet	DC field	200	100	15	-	7.2
2.	1^{st}-stage RF carpet	Nozzle	DC field	200	100	9.6	-	4.6
3.	Nozzle	2^{nd}-stage RF carpet	Gas jet	10	-	10	360	0.3
4.	2^{nd}-stage RF carpet	Extraction nozzle	Traveling wave	10	-	50	100–200	2.5–5.0
	Mean extraction time, ms							**14.6–17.1**

described in Section 4.2.3, as well as projected from the prototype CSC at the FRS Ion Catcher at GSI (see Chapter 2). The values are presented for the standard mode and the trade-off mode. In standard mode, all performance parameters can be reached simultaneously. The trade-off mode reflects the case when one of the performance parameters is maximized at the expense of sacrificing the others. Obviously, the values of the parameters in this mode cannot be reached simultaneously.

Based on the conceptual design and the developments presented above, a technical design of the CSC has been developed and is described in detail in Appendix B. A digital mockup is shown in Figure 4.14.

The results of this chapter indicate that the proposed concept of the CSC will be

Table 4.3: Expected performance of the CSC for the Super-FRS at FAIR. In standard mode, all performance parameters can be reached simultaneously. In the trade-off mode, one of the performance parameters is maximized at the expense of sacrificing the others. The values presented in this mode cannot be reached simultaneously.

Parameter	Standard mode	Trade-off mode
Areal density	28 mg/cm^2	41 mg/cm^2
Extraction efficiency	$\geqslant$50%	$\geqslant$50%
Mean extraction time	15–17 ms	$<$10 ms
Rate capability	10^7 ions/s	10^9 ions/s

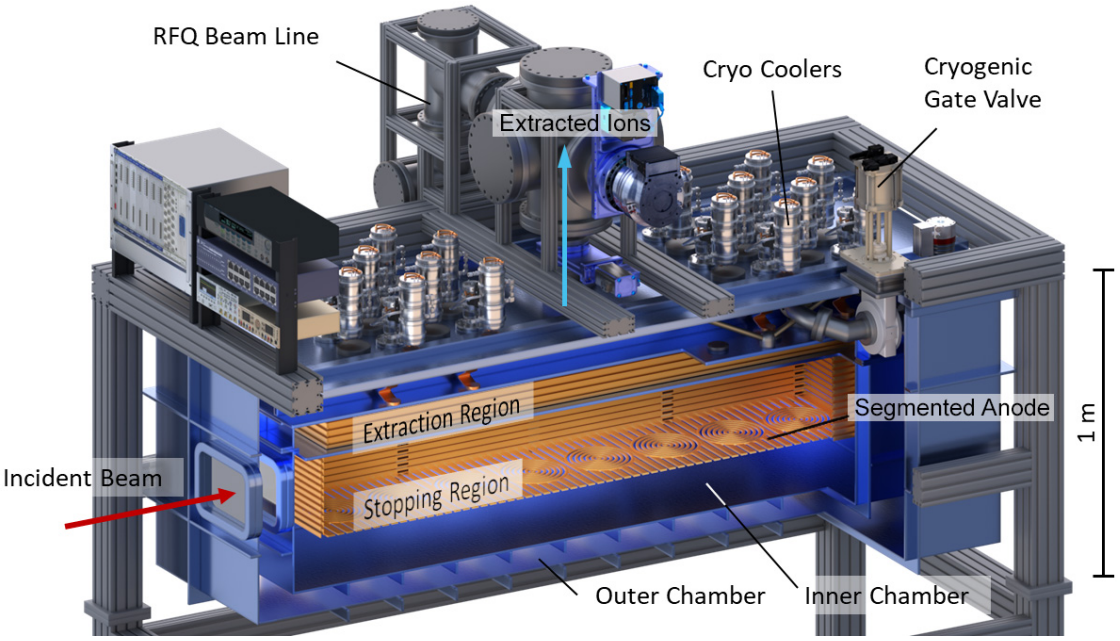

Figure 4.14: A digital mockup of the cryogenic stopping cell for the Super-FRS.

able to fulfill the unprecedented performance requirements. The state-of-the-art gas-filled cryogenic stopping cell with the stopping efficiency close to unity, short ion extraction time of 15–17 ms, two-stage extraction with efficiency of $\geqslant$50% that is almost ion- and element-independent, and rate capability of 10^7 ions/s is feasible both conceptually and technically. Intense relativistic beams of short-lived exotic nuclei will be converted into low-energy and low-emittance beams in a fast and efficient manner, enabling unique experiments at the Super-FRS at FAIR.

Summary and outlook

Research with exotic nuclei provides essential information for understanding the structure of atomic nucleus and the evolution of the Universe. Significant efforts are made at large-scale accelerator-based facilities worldwide to provide experimental access to more exotic nuclei. The efforts include: (i) building more powerful next-generation radioactive ion beam (RIB) facilities, (ii) pushing the limits of the existing RIB facilities by improving the instrumentation and detection methods, and (iii) exploring new techniques and reactions for producing the exotic nuclei. The Super-FRS fragment separator at the future Facility for Antiproton and Ion Research FAIR (Darmstadt, Germany) is an example of point (i). For points (ii) and (iii) advanced detection systems have been developed and first results are presented in this thesis.

The related experimental concepts were developed and tested at the FRS Ion Catcher (FRS-IC) setup at GSI Helmholtz Center for Heavy Ion Research (Darmstadt, Germany) under different conditions. There, fast and intense ion beams of exotic nuclei are thermalized in the cryogenic stopping cell (CSC) and are detected in the multiple-reflection time-of-flight mass-spectrometer (MR-TOF-MS) allowing numerous type of measurements.

A measurement campaign for isomer studies was done in the region of the heaviest $N = Z$ nuclei. The isomeric states in odd $^{101-109}$In haven been studied. The detected abundances of ground and isomeric states reflect the processes of angular momentum population in the reaction. The systematics for five isotopes with the same spin assignment in ground and isomeric states and very similar excitation energy of the isomer, studied here presented an ideal test case to see if the details of the nuclear structure of these nuclei were relevant. A comparison of the measured isomer-to-ground-state ratios to the widely-used sharp cutoff model (SCM) revealed a significant discrepancy as one approaches the $N = 50$ shell closure. Since nuclear structure contributions are not considered in the SCM, it is concluded that the nuclear structure changes in ^{101}In. Thus, a refined model that considers the reaction dynamics and the nuclear structure is urgently called for.

The measured isomer excitation energies probed the nuclear shell and mean-field models, and allowed to study the isotope of ^{99}In (one proton removed from ^{100}Sn). The mass and isomer excitation energy of ^{99}In isotope have been measured only very recently and have confirmed predictions made in this work.

During this study also the first discovery of an isomeric state, namely a $(1/2^-)$ isomeric state in ^{97}Ag, with an MR-TOF-MS was possible. The discovery was supported by a mean-field model. In the future, many more isomer discoveries are anticipated using this method due to unique characteristics of the MR-TOF-MS.

In a next step the neutron-rich region at $N = 126$ was studied. The mean range

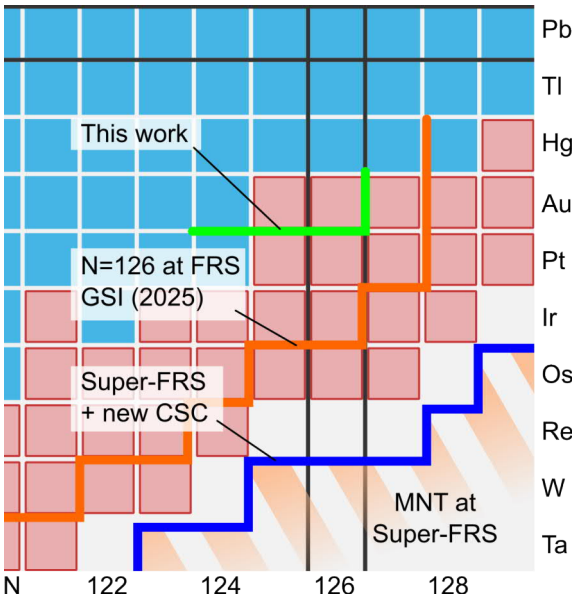

Figure 4.15: A chart of nuclides in the region of N=126 below doubly-magic ^{208}Pb. Nuclei with known and unknown masses are shown in blue and red correspondingly. The masses of $^{203-205}$Au isotopes measured in this work reveal discrepancies and show a need for future measurements (green line). The regions of interest of the future experiments at the FRS, GSI in 2025 and at the Super-FRS, FAIR are denoted by orange and blue lines correspondingly. Multi-nucleon transfer (MNT) reactions with radioactive beams at the Super-FRS are expected to provide better access to lighter nuclei in this region, relevant to the r-process studies (hashed orange region). The developments presented in this work pave the way for these experiments.

bunching technique, developed in this work, allowed to thermalize ions of multiple nuclides simultaneously, thereby making a more effective use of beam time. The presented mass measurements of $^{203-205}$Au isotopes (Fig. 4.15, green) mark an important milestone in reaching the $N = 126$ isotones that are relevant for the 3rd abundance peak of the r-process. Moreover these masses put to test the mass models that are used in calculations of the r-process. The revealed discrepancies clearly showed the need for further measurements.

A campaign aiming for systematic large-scale mass measurement at the $N = 126$ region below ^{205}Au is scheduled for GSI beam time in 2025. This region, denoted in Fig. 4.15 by orange and blue lines for FRS and Super-FRS, is uniquely accessible at GSI and FAIR.

As mentioned before there is also a search for new reaction methods which provide a better access to the $N = 126$, beyond what is technically possible with in-flight fragmentation of stable beams. The multi-nucleon transfer (MNT) reactions are a promising candidate for that role, especially MNT reactions with neutron-rich RIB. The latter has not been experimentally studied so far. The instrumentation to conduct proof-of-concept experiments with MNT reactions at the FRS-IC has been developed, built and commissioned in this thesis. At the FRS-IC, the MNT experiments with stable and close-to-stable fragment beams are scheduled for beam time in 2024. This will be followed up by studies with RIB at the

Super-FRS at the end of the decade, aiming at the hashed orange region shown in Fig. 4.15.

The same instrumentation is also suited for studying spontaneous fission. A measurement campaign planned at the FRS-IC will provide high-quality data for both fundamental and practical applications of nuclear fission.

The CSC at the FRS-IC serves as a prototype of the future CSC for the Super-FRS at FAIR, where the intensity, energy and dimensions of the ion beams place even more stringent requirements on the CSC. In this thesis, the proposed conceptual design of the CSC was developed and studied in detailed simulations. The results showed that the future CSC will be able to fulfill the unprecedented performance requirements – the stopping efficiency close to unity, short ion extraction time of 15 ms, two-stage extraction with efficiency of $\geqslant$50% that is almost ion- and element-independent, and rate capability of 10^7 ions/s.

The CSC for the Super-FRS in combination with the MR-TOF-MS will be a key device to enable mass, decay, and laser spectroscopy experiments. It will offer unique experimental capabilities beyond mass measurements. Branching ratios of rare decay modes will be determined directly *e.g.*, β-delayed neutron emission probabilities P_{xn}. A dedicated experiment is among the first experiments planned for FAIR Early Science beam time in 2028.

Zusammenfassung

Die Forschung mit exotischen Kernen liefert entscheidende Informationen für das Verständnis der Struktur des Atomkerns und die Entwicklung des Universums. Weltweit werden erhebliche Anstrengungen unternommen, um experimentellen Zugang zu exotischeren Kernen zu ermöglichen. Diese Bemühungen umfassen: (i) den Aufbau leistungsfähigerer radioaktiver Ionenstrahl (RIB)-Einrichtungen der nächsten Generation, (ii) das Ausreizen der Grenzen der bestehenden RIB-Einrichtungen durch Verbesserung der Instrumentierung und Detektionsmethoden, (iii) die Erforschung neuer Techniken und Reaktionen zur Herstellung exotischer Kerne.

Das Super-FRS Fragmentseparator am künftigen FAIR (Darmstadt, Deutschland) ist ein Beispiel für Punkt (i). Fortschrittliche Detektionssysteme wurden für die Punkte (ii) und (iii) entwickelt, und erste Ergebnisse werden in dieser Arbeit präsentiert.

Die damit verbundenen experimentellen Konzepte wurden unter verschiedenen Bedingungen im FRS Ion Catcher (FRS-IC) am GSI Helmholtzzentrum für Schwerionenforschung (Darmstadt, Deutschland) entwickelt und getestet. Dort werden schnelle und intensive Ionenstrahlen exotischer Kerne in der kryogenen Stoppzelle (CSC) abgekühlt und im Multireflexions-Flugzeit-Massenspektrometer (MR-TOF-MS) detektiert, was verschiedene Arten von Messungen ermöglicht.

In einem Messkampagne wurden Isomeriestudien im Bereich der schwersten $N = Z$-Kerne durchgeführt. Die isomeren Zustände in ungeraden $^{101-109}$In Isotopen wurden untersucht. Die festgestellten Häufigkeiten von Grundzuständen und isomeren Zuständen spiegeln die Prozesse der Population von Drehimpuls in der Reaktion wider. Die Systematik für fünf Isotope mit der gleichen Spinzuordnung in Grundzuständen und isomeren Zuständen sowie sehr ähnlichen Anregungsenergien der Isomere, die hier untersucht wurden, stellte sich als ein idealer Testfall heraus, um festzustellen, ob die Details der Kernstruktur dieser Kerne relevant waren. Ein Vergleich der gemessenen Isomer-zu-Grundzustands-Verhältnisse mit dem weit verbreiteten Sharp Cutoff Model (SCM) ergab eine erhebliche Abweichung, wenn man sich dem $N = 50$ Schalenabschluss nähert. Da Kernstrukturbeiträge im SCM nicht berücksichtigt werden, wird geschlussfolgert, dass sich die Kernstruktur in ^{101}In ändert. Daher ist ein verfeinertes Modell, das die Reaktionsdynamik und die Kernstruktur berücksichtigt, dringend erforderlich.

Die gemessenen Isomer-Anregungsenergien wurden zur Prüfung von Kernschalen- und Mean-Field-Modellen verwendet und ermöglichten die Untersuchung des Isotops ^{99}In (ein Proton entfernt von ^{100}Sn). Die Masse und die Isomer-Anregungsenergien des Isotops ^{99}In wurde erst kürzlich gemessen und hat die in dieser Arbeit getroffenen Vorhersagen bestätigt.

Im Rahmen dieser Studie wurde auch die erste Entdeckung eines isomeren Zustands möglich, nämlich eines $(1/2^-)$ isomeren Zustands in ^{97}Ag, mit einem MR-TOF-MS. Die Entdeckung wurde durch ein Mean-Field-Modell unterstützt. In der Zukunft werden viele weitere Isomerentdeckungen erwartet, die diese Methode aufgrund der einzigartigen Eigenschaften des MR-TOF-MS ermöglicht.

In einem nächsten Schritt wurde die neutronenreiche Region bei $N = 126$ untersucht. Die entwickelte Mean-Range-Bunching-Technik ermöglichte das gleichzeitige Stoppen von Ionen verschiedener Nuklide, was eine effektivere Nutzung der Strahlzeit ermöglichte. Die vorgestellten Massenmessungen der Isotope $^{203-205}$Au markieren einen wichtigen Meilenstein auf dem Weg zur $N = 126$-Isotone, die für den 3.Abundanzgipfel des r-Prozesses relevant sind. Diese Massen stellen auch die Massenmodelle auf die Probe, die für Berechnungen des r-Prozesses verwendet werden. Die aufgedeckten Abweichungen zeigen deutlich den Bedarf an weiteren Messungen.

Zusätzlich wird eine Kampagne zur systematischen Massenmessung in der $N = 126$-Region unterhalb von ^{205}Au für die GSI-Strahlzeit im Jahr 2025 geplant. Diese Region, wie in Abb. 4.15 durch orange und blaue Linien für FRS und Super-FRS dargestellt, ist ausschließlich verfügbar bei GSI und FAIR.

Wie bereits erwähnt, wird auch nach neuen Reaktionsmethoden gesucht, um einen besseren Zugang zu $N = 126$ zu erhalten, der über das hinausgeht, was technisch mit in-flight Fragmentierung von Strahlen stabiler Nuklide möglich ist. Die Multi-Nucleon-Transfer (MNT)-Reaktionen sind ein vielversprechender Kandidat für diese Rolle, insbesondere MNT-Reaktionen mit neutronenreichen RIB. Letztere wurden bisher noch nicht experimentell untersucht. Die entwickelte Instrumentierung ermöglicht Proof-of-Concept-Experimente mit Strahlen stabiler und nahezu stabiler Fragmente am FRS-IC. Bei FRS-IC sind MNT-Experimente mit stabilen und nahezu stabilen Fragmentstrahlen für die Strahlzeit im Jahr 2024 geplant. Dies wird durch Studien mit RIB am Super-FRS gegen Ende des Jahrzehnts fortgesetzt, mit dem Ziel, die in Abb. 4.15 gezeigte schraffierte orangefarbene Region zu erreichen. Die gleiche Instrumentierung ist auch für die Untersuchung der Spontanspaltung geeignet. Eine geplante Messkampagne am FRS-IC wird hochwertige Daten für sowohl grundlegende als auch praktische Anwendungen der Kernspaltung liefern.

Die CSC am FRS-IC dient als Prototyp für die zukünftige CSC am Super-FRS bei FAIR, wo die Intensität, die Energie und die Abmessungen der Ionenstrahlen noch anspruchsvollere Anforderungen an die CSC stellen. In dieser Arbeit wurde das vorgeschlagene konzeptionelle Design der CSC entwickelt und in detaillierten Simulationen untersucht. Die Ergebnisse zeigten, dass die zukünftige CSC in der Lage sein wird, die rekorden Leistungsanforderungen zu erfüllen - die Stoppeffizienz nahe bei Eins, kurze Extraktionszeit von 15 ms, zweistufige Extraktion mit einer Effizienz von $\geqslant$50%, die nahezu ionen- und elementunabhängig ist, und eine Rate von 10^7 Ionen/s.

Die CSC für den Super-FRS in Kombination mit dem MR-TOF-MS wird ein Schlüsselgerät sein, um Massen-, Zerfalls- und Laserspektroskopie-Experimente zu ermöglichen und einzigartige experimentelle Möglichkeiten jenseits von Massenmessungen zu bieten. Ein dediziertes Experiment zur β-verzögerten Neutronenemission (P_{xn}) ist für 2028 geplant.

Acknowledgments

As I reflect on the pages of this thesis, I find myself humbled and profoundly grateful for the multitude of individuals who have contributed to this journey.

First and foremost, I would like to express my deepest appreciation to my academic advisors Prof. Dr. Christoph Scheidenberger and Prof. Dr. Dr. h.c. Hans Geissel for this remarkable research opportunity in the IONAS group, captivating topics and challenging projects you entrusted me with. Your trust and support have been pivotal in shaping my academic journey. I would like to extend my sincere gratitude to Prof. Dr. Kai-Thomas Brinkmann for his insightful comments, guidance and expertise.

I'm deeply indebted to Dr. Timo Dickel for always finding that 25^{th} hour in the day to provide guidance, share knowledge and wisdom, and offer help in preparing this thesis. I would also like to extend my deepest gratitude to Dr. Wolfgang R. Plaß for his invaluable mentorship that has steered me through the challenges of my doctoral journey.

This endeavor would not have been possible without my dearest colleagues. I wish to thank Dr. Christine Hornung, Dr. Ivan Miskun and Dr. Samuel Ayet for their assistance and knowledge as I embarked on this new journey. I wish to thank Gabriella Kripkó-Koncz, Sönke Beck, and Julian Bergmann, with whom I had the pleasure of learning and going through the roller-coaster of the beam times together. I would like to extend my thanks to Dr. Jianwei Zhao, Kriti Mahajan, Nazarena Tortorelli who seamlessly took over my lab responsibilities, allowing me to focus on this thesis. Special thanks to my dear colleagues Dr. Darya Kostyleva, Dr. Heinrich Wilsenach, Florian Greiner and Makar Simonov for their supportive friendship, and quality time inside and outside of work.

I am deeply thankful to Prof. Dr. Israel Mardor, Dr. Alexandru State, Dr. Adrian Rotaru, Dr. Anamaria Spataru and Lizzy Gröf for very fruitful collaboration in working on the developments for the spontaneous fission and MNT reaction studies. My gratitude extends to Prof. Jerzy Dudek, Prof. Takaharu Otsuka, Dr. Magdalena Górska, Dr. Hubert Grawe, Dr. Andrey Blazhev, Dr. Irene Dedes, Dr. Noritaka Shimizu and Dr. Yusuke Tsunoda for immense contributions to our nuclear structure explorations in the region of $N = Z$ nuclei.

I want to express my sincere gratitude to Evelin Prinz, Daniela Preß, Rita Krause and Luise Dörsching-Steitz for their endless support with an endless bureaucracy and beyond. I extend my gratitude to Karl-Heinz Behr, Bogdan Szczepanczyk, Michael Will, Philipp Schwarz and other members of the technical staff of the FRS/Super-FRS for their help in the lab and for understanding even without words what technical problem I was having. Many thanks to Thomas Wasem for his masterful support with CAD-related matters.

To my dearest friends in Kazakhstan – Eskendir, Almas, Ernaz and Tani – thank you for making our rare meetings so re-energizing and heartwarming.

To my wife Assel – thank you for your love, patience and support, no matter what. You mean the world to me. To Alan, my son, my Windkraftanlage and my world-class pilot of Tu-154 aircraft – thank you for waiting so patiently while dad wrote his “book” and for all the wonderful moments you filled this difficult time with.

I would like to express my deepest gratitude to my parents Жанат Канетбековна and Данияр Усерович, brother Амаль and grandfather Өсер Өмірбайұлы for their unwavering love, encouragement, and sacrifices that have made all this possible.

Lastly, I would like to extend my heartfelt appreciation to anyone whose support and contributions I may have inadvertently overlooked in these acknowledgments.

Appendix A

Ion motion in electrical fields and matter

This chapter provides an overview of the processes involved in the slowing down, thermalization and extraction of ions in the stopping cell. A comprehensive understanding of these processes is crucial for effectively running experiments with stopped beams and related developments.

A.1 Slowing down of relativistic heavy ions in matter

When passing through medium, heavy-ion projectile lose energy primarily via inelastic collisions with electrons of target atom. The energy loss can be treated as a continuous process because in dense matter the number of discrete collisions is very large. The mean energy loss dE in a matter of a thickness dX (expressed in units of areal density) is called **stopping power** and can be expressed as:

$$-\frac{dE}{dX} = \frac{4\pi e^2}{m_e c^2 \beta^2} \cdot (Z_1 e)^2 \cdot N Z_2 \cdot L, \tag{A.1}$$

where e is the elementary charge, $c^2\beta^2$ and $Z_1 e$ are the velocity and charge of the projectile ion, m_e and NZ_2 are the mass and average density of the target electrons, and L is the so-called stopping logarithm.

The stopping logarithm L was derived from first-order quantum perturbation theory by Bethe [Bethe, 1932] in the form:

$$L_{\text{Bethe}} = \ln\left(\frac{2m_e c^2 \beta^2 \gamma^2}{I}\right) - \beta^2, \tag{A.2}$$

where I is the mean ionization potential of the target atoms, and γ is the Lorentz factor.

Further, additional corrections were introduced:

- Density effect $-\delta/2$. Considers the fact that distant electrons are screened from projectile ion by polarized target atoms. Their contribution to the energy loss is therefore reduced.

- The Bloch correction $\Delta L_{\mathrm{Bloch}}$ [Bloch, 1933]. Brings to agreement classical treatment of Bohr [Bohr, 1913] and quantum-mechanical treatment of Bethe at low energies.
- The Mott correction ΔL_{Mott} [Mott, 1929]. Considers scattering of Dirac electrons in a potential of point-like nuclei instead of free electrons. The correction becomes especially prominent for highly charged nuclei at relativistic energy.
- The Ahlen correction $\Delta L_{\mathrm{Ahlen}}$ [Ahlen, 1982]. Introduces relativistic correction to $\Delta L_{\mathrm{Bloch}}$.

Other corrections exist *e.g.*, the Barkas correction, the shell corrections but are below 1%, and thus negligible in the case of heavy relativistic ions. A comprehensive description and numerical formulations can be found in [Weaver and Westphal, 2002].

First direct measurements of stopping power of relativistic heavy nuclei performed at GSI revealed systematic deviations from Bethe theory [Scheidenberger et al., 1994]. A satisfactory agreement was achieved when the corrections above were considered.

A new formulation of the theory was proposed by Lindhard and Sørensen (LS theory) [Lindhard et al., 1996]. In their work, it was shown that the shortcomings of Bethe theory were due to the first-order quantum perturbation approach being inapplicable in close collisions which dominate stopping process. The correction they introduced Δ_{LS} is based on calculating the momentum transfer cross sections of Dirac electrons in a spherically-symmetric potential of a finite size nucleus. It follows that Δ_{LS} incorporates Bloch, Mott and Ahlen corrections. Moreover, the finite size consideration plays a role at very high energies *i.e.*, when the de Broglie wavelength of the scattered electron approaches the size of the projectile nucleus.

The stopping logarithm L can therefore be expressed as:

$$L = L_{\mathrm{Bethe}} + \Delta L_{\mathrm{LS}} - \delta/2. \tag{A.3}$$

The LS theory showed excellent agreement with measurements of stopping powers of fully-stripped relativistic heavy ions performed at GSI [Geissel and Scheidenberger, 1998, Weick et al., 2000] (0.5–1.0 GeV/u) and CERN [Datz et al., 1996] (160 GeV/u).

At lower energies the projectile ions are no longer fully-stripped, therefore one has to take into account charge states. This is done by (i) replacing $Z_1 e$ by effective charge [Pierce and Blann, 1968] in Eq. A.1, and (ii) calculating weighted sum of partial stopping powers, where the weights are obtained from measured charge-state distributions [Weick et al., 2000].

The process of slowing down in matter takes place in the sub-nanosecond time scale because the electric field in the atom is many orders of magnitude larger compared to the strongest electromagnetic device.

Range and range straggling

The amount of energy transferred in a single collision between an ion and an electron fluctuates due to the statistical nature of the process. After multiple collisions

when passing through matter, the width of the initial energy distribution of ions broadens. Such broadening is referred to as energy-loss straggling.

It also follows that the distance ions travel in matter before full thermalization is statistically distributed. The mean and standard deviation of this distribution are range R and range straggling Ω_R correspondingly, and can be expressed as:

$$R(E) = \int_{E_{\min}}^{E_0} (dE/dX)^{-1}\, dE, \qquad R \propto \frac{A_1}{{Z_1}^2}, \tag{A.4}$$

$$\Omega_R^2(E) = \left\langle \left(R(E) - \langle R(E)\rangle\right)^2 \right\rangle, \qquad \Omega_R \propto \frac{\sqrt{A_1}}{{Z_1}^2}. \tag{A.5}$$

Besides nuclear reaction kinematics, additional contributions to the range straggling are present (i) in case the beam of incident ions is a mixture of several charge-states [Weick et al., 2000, Weick et al., 2002] and (ii) due to matter inhomogeneity [Geissel et al., 2002]. The former vanishes at relativistic energies because the ions are fully-stripped. The latter is minimized by focusing the beam to a spot of a diameter of $\leqslant$1 mm, and using materials with low surface roughness and low thickness variation.

A.2 Ion motion in gas and electrostatic fields

The ions are thermalized in a buffer gas of a stopping cell and are guided towards extraction by the means of electric fields and/or gas flow. In the general case, the motion of a particle in a fluid is governed by the Navier–Stokes equation [Landau and Lifshitz, 1987]:

$$\frac{D\vec{v}}{Dt} = \frac{\delta\vec{v}}{\delta t} + (\vec{v}\cdot\nabla)\,\vec{v} = \vec{G} - \frac{1}{\rho}\nabla P + \left(\zeta + \frac{\mu}{3}\right)\nabla(\nabla\cdot\vec{v}) + \mu\nabla^2\vec{v}, \tag{A.6}$$

where $\vec{v}$, ρ, μ, ζ are the velocity, volumetric density, dynamic shear viscosity and volume viscosity of the particle correspondingly; $\vec{G}$ represents external forces acting on the fluid, ∇P is a pressure gradient, and the remaining terms represent viscous forces.

For a charged particle undergoing collisions with gas molecules in presence of electrostatic fields, the term $\vec{G}$ is:

$$\vec{G} = \pm\frac{q}{m}\vec{E} - f\,(\vec{v} - \vec{u})\,, \tag{A.7}$$

where $\pm q$ and m are the charge and mass of the particle, $\vec{E}$ is the applied electric field, f is averaged collision frequency, and $\vec{u}$ is velocity of the collisional counterpart *i.e.*, gas flow. Mutual collisions between ions can be neglected as well as Coulomb interaction because the density of ions is many orders of magnitude smaller compared to the density of the buffer gas.

If the motion of the fluid is slower compared to the time between collisions, one can assume the steady state *i.e.*, $D\vec{v}/Dt = 0$ and $\vec{u} = 0$. Further, an incompressible flow can be considered *i.e.*, $\nabla\cdot\vec{v} = 0$ in case there are no significant changes in fluid density. The Eq. A.6 then simplifies to:

$$0 = \pm\frac{q}{m}\vec{E} - f\vec{v} - \frac{1}{\rho}\nabla P. \tag{A.8}$$

Solving for $\vec{v}$, and considering for a single ion $\rho = mn$, where n is a number density, one obtains:

$$\vec{v} = \pm\frac{q}{mf}\vec{E} - \frac{1}{mnf}\nabla P \tag{A.9}$$

$$\vec{v} = \pm\frac{q}{mf}\vec{E} - \frac{k_B T}{mf}\frac{\nabla n}{n} = K\vec{E} - D\frac{\nabla n}{n}. \tag{A.10}$$

Here, K is the ion mobility and D is the diffusion coefficient.

From Eq. A.10 it follows that the ion motion occurs along the electric field lines superimposed on isotropic (*i.e.*, directionless) diffusion in gas. The value of the ion velocity is therefore:

$$|\vec{v}| = K|\vec{E}| \tag{A.11}$$

The ion mobility K is often expressed in term of reduced ion mobility K_0 *i.e.*, ion mobility obtained under normal conditions $P_0 = 1.013 \cdot 10^5$ Pa and $T_0 = 273.15$ K:

$$K = K_0 \cdot \frac{P_0}{P} \cdot \frac{T}{T_0} \tag{A.12}$$

One can obtain an expression for the mean time t it takes an ion to travel distance d under given gas and electric field conditions:

$$t = \frac{1}{K_0} \cdot \frac{T_0}{P_0} \cdot \frac{P}{T} \cdot \frac{d^2}{V_{\mathrm{DC}}}. \tag{A.13}$$

It follows that at stable gas conditions, a faster ion extraction from a stopping cell can be achieved under shorter distances and higher DC voltages V_{DC}. The voltage at certain gas conditions is limited due to breakdown given by the Paschen's law [Paschen, 1889].

The assumptions above are applicable to the large-volume stopping cells where the nuclei are thermalized in ionized form. In case the nuclei are neutralized, their transport is only possible with a gas flow. Therefore all terms of Eq. A.6 have to be considered. The analytical solution does not exists, and the problem can only be approached using numerical methods. A related discussion is beyond the scope of this thesis.

A.3 Ion motion at RF carpet

The ions guided towards extraction by an electric (pushing) field will terminate on electrodes. In order to prevent this, a radio frequency (RF) electrode structure is used [Masuda et al., 1972]. It generates an effective RF field which counteracts the pushing field, and thus repels the ions from the surface.

The working principle is schematically shown in Figure A.1. Such RF structure is an array of closely spaced electrodes to which the RF of a few MHz and about 100 Vpp is applied. The phase of the RF is shifted by 180° at adjacent electrodes. These structures are typically shaped as cones (RF funnel) or have a planar geometry (RF carpet). Several examples of the RF carpets and funnels are shown in

Fig. 1.7 and are discussed in the corresponding section. In the setups considered in this thesis, an RF carpet geometry is used. Therefore, the following describes the RF carpet, while it is also applicable to other geometries.

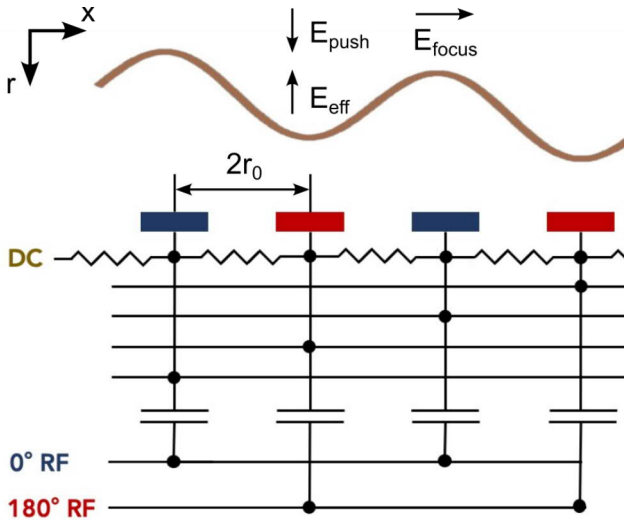

Figure A.1: Schematic illustration of a working principle of an RF carpet. An inhomogeneous field E_{eff} is created by an RF phase-shifted by 180° on adjacent electrodes spaced at a distance of $2r_0$. It counteracts pushing field E_{push} allowing ions to be stored above the surface. An imposed DC gradient generates focusing field E_{focus} which transports the ions along the surface towards extraction.

The effective field generated by an RF carpet can be estimated using a pseudopotential approach, suggested by M. Wada [Wada et al., 2003]. In vacuum, an ion oscillating in a non-uniform RF field $E(r,t) = E_0(r)\cos(\omega t)$ encounters the strongest repulsive force when it is closest to the electrode. This force averaged over the cycle can be associated with pseudopotential $U(r)_{\text{ps}}^{\text{vac}}$ [Dehmelt, 1967]:

$$U(r)_{\text{ps}}^{\text{vac}} = \frac{q}{4m\omega^2}\cdot E_0^2(r) = \frac{q}{4m\omega^2}\cdot V^2\cdot\frac{4}{r_0^2}\cdot\left(\frac{r}{r_0}\right)^2. \tag{A.14}$$

The Eq. A.14 assumes E_0 to be a quadrupole field with the amplitude of the potential V, and the half distance between the electrodes r_0. The resulting effective field is therefore:

$$E_{\text{eff}}^{\text{vac}} = -\nabla U(r)_{\text{ps}}^{\text{vac}} = -2\cdot\frac{q}{m\omega^2}\cdot V^2\cdot\left(\frac{1}{r_0}\right)^3\cdot\frac{r}{r_0}. \tag{A.15}$$

The influence of the buffer gas can be taken into account by introducing a damping coefficient γ [Tolmachev et al., 1997]:

$$\gamma = \frac{E_{\text{eff}}^{\text{gas}}}{E_{\text{eff}}^{\text{vac}}} = \frac{\omega^2\tau^2}{1+\omega^2\tau^2} = \begin{cases} 1 & \text{for } \omega^2\tau^2 \gg 1 \text{ (vacuum)},\\ \omega^2\tau^2 & \text{for } \omega^2\tau^2 \ll 1 \text{ (high pressure)}, \end{cases} \tag{A.16}$$

where $\tau = K\cdot m/q$ is a relaxation time between collisions. A high-pressure environment of the stopping cell corresponds to the case $\omega^2\tau^2 \ll 1$.

Combining Eq. A.12, A.15–A.16 and considering the applied RF voltage is twice the voltage associated with the pseudopotential field $V_{\text{RF}} = 2V$ we find the effective field of the RF carpet in buffer gas:

$$E_{\text{eff}}^{\text{gas}} = -\frac{1}{2}\cdot\frac{r}{r_0}\cdot\left(K_0\frac{P_0}{T_0}\right)^2\cdot\left(\frac{1}{r_0}\right)^3\cdot\left(\frac{T}{P}\right)^2\cdot\frac{m}{q}\cdot {V_{\text{RF}}}^2. \tag{A.17}$$

This equation demonstrates an intricate balance between parameters of buffer gas (P, T), applied voltage (V_{RF}) and electrodes geometry (r_0) which have to be carefully selected to effectively repel and store ions of interest (m, q, K_0). An analytical description of ion motion in the two-phase RF field and buffer gas can be found in [Schwarz, 2011].

Next, the stored ions are transported along the RF carpet surface towards an exit hole *i.e.*, an orifice or a *de Laval* nozzle where they are pushed through by the gas flow and are eventually extracted out of the stopping cell. The transport along the RF carpet can be realized by imposing a DC gradient which generates a focusing field (see Fig. A.1). If the depth of the trapping pseudopotential is shallow, this transverse motion can be approximated by the electrostatic case described in Section A.2.

Another focusing technique called "ion surfing" has been demonstrated [Bollen, 2011, Brodeur et al., 2013, Arai et al., 2014]. Here, the RF is imposed with a weak audio-frequency (AF) signal phase-shifted by 90° across the electrodes with a frequency in a kHz region. This technique enables about a factor of 10 faster ion transport, although limited to low-pressure environment.

A.4 Space-charge effect

At high rates of incoming ions, the efficiency of ion extraction from a stopping cell is impacted negatively. This phenomenon is referred to as a space-charge effect, and it manifests itself in two regions – in the bulk of the stopping volume [Takamine et al., 2005] and at the extraction nozzle of RF carpet/funnel [Savard, 2011].

In the bulk of the stopping volume: in the process of thermalization, an ion loses its kinetic energy via inelastic collisions with buffer gas atoms (see Section A.1). Each collision results in a production of ion–electron pair of buffer gas. The mean energy for ion–electron pair creation in He is 41 eV [Leo, 1994]. Thus, a beam of ions with an energy of 1 MeV/u and a mass of 100 u generates on average $2.4 \cdot 10^6$ $\mathrm{He}^+/\mathrm{e}^-$ pairs per thermalized ion.

In presence of applied (external) electric field, the electrons are quickly removed since their mobility K is ∼2–3 orders of magnitude higher than that of the ions (see Eq. A.13). The He^+ and beam ions have similar ion mobility. Hence, a large amount of positive charge is created in the stopping volume, forming a region of non-neutral plasma. The resulting (internal) electric field pushes ions outwards thereby increasing the size of the ion cloud. At high intensity, the size of ion cloud exceeds the internal dimensions of the stopping volume causing ions to hit the walls or electrodes, resulting in a loss in extraction efficiency. In the most intense cases, the plasma completely screens its internal volume from the applied (external) electric field.

In the vicinity of an RF carpet (or funnel), the space-charge effect is weaker [Heiße, 2015]. Typically, mass–over–charge ratio m/q of IOI is larger compared to He^+ ions, therefore the latter feel weaker repelling effective RF field E_{eff} (see Eq. A.17). As a result, the He^+ ions – the major charge-carrier – are dumped at the RF carpet surface while the ions of IOI are repelled and extracted.

It follows that space-charge effect in the bulk can be mitigated by faster removal of the excessive positive charge (see Eq. A.13), stopping ions closer to the RF carpet, and increasing the area of the stopping volume covered in RF electrode structures.

The ionization potential of impurities in buffer gas is lower than that of He. Therefore ions of He^+ will preferably undergo charge-exchange reactions when colliding with impurities. If present in large amounts, the impurity ions become the major charge carrier. In case m/q of such ions is low compared to that of IOI, the situation described above applies. However, if the m/q of impurity ions becomes comparable or larger than that of IOI, the space-charge effect **at the extraction nozzle** may occur. Being effectively transported by an RF carpet along with IOI, the impurity ions create a region at the extraction nozzle with high charge density, pushing all ions away from it and thus disrupting the extraction.

This effect can be mitigated by ensuring the highest cleanliness of the buffer gas. In situ gas purification, and operation of a stopping cell at cryogenic temperature serve this purpose [Dendooven et al., 2006]. Additional improvement is due to geometry of the extraction nozzle – higher gas throughput removes the excessive charge faster. As demonstrated in [Ringle et al., 2021], the onset of space-charge effect for a nozzle with a simple orifice geometry occurred at about an order of magnitude higher beam intensity compared to the *de Laval* nozzle of a similar diameter.

A.5 Ion-molecule chemical reactions

Chemical reactions between an atomic ion of interest and an impurity molecule in the buffer gas is one of the mechanisms of ion loss. The reaction can be described as:

$$\mathrm{X}^+ + \mathrm{M}_i \longrightarrow \mathrm{XM}_i{}^+, \tag{A.18}$$

where X^+ is an atomic ion of interest, M_i is a ligand of impurity molecule i (*e.g.*, $(\mathrm{OH})_n$, $(\mathrm{CO})_n$, $\mathrm{H_2O}$, etc), and $\mathrm{XM}_i{}^+$ is a molecular ion product. Technically, the molecular ion $\mathrm{XM}_i{}^+$ is not lost for extraction because it still carries the charge and can be effectively transported by an RF carpet/funnel. However, the IOI becomes spread across several molecular forms i, and thus only a fraction of the total signal can be measured at a time. Such losses are minimized if the number of collisions between IOI and impurity molecule until extraction is minimized.

The number of such collisions can be controlled via buffer gas density, ion extraction time and concentration of impurity *i.e.*, gas cleanliness. Fixing the buffer gas and extraction time, one can deduce requirements for gas cleanliness by comparing extraction time to a time constant τ of chemical reaction. The time constant τ can be expressed as:

$$\tau = \frac{1}{k_i[\mathrm{M}_i]} = \frac{1}{k_i} \cdot \frac{1}{w_i \cdot n_{\mathrm{He}}}, \tag{A.19}$$

where k_i is a reaction rate, $[\mathrm{M}_i]$ is a concentration of impurity expressed as a fraction w_i of buffer gas number density n_{He}. Considering reaction rates of fast reactions of $k_i \geqslant 10^{-9}\,\mathrm{cm}^3/\mathrm{s}$ [Pohjalainen, 2018], number density of buffer gas of $n_{\mathrm{He}} = 2 \cdot 10^{18}\,\mathrm{cm}^{-3}$ (100 mbar, 298 K) and ion extraction time of 100 ms, one

can deduce that the impurity fraction has to be $w_i \ll 4 \cdot 10^{-9}$ *i.e.*, below 1 ppb level [Reiter, 2015].

Appendix B

Technical design of the CSC for the Super-FRS

Technical design of the CSC for the Super-FRS consolidates vacuum, cryogenic, electrodes, and gas handling systems. It has to ensure that the solutions of conceptual design are implemented. In addition, it has to meet infrastructure-related requirements *i.e.*, the overall dimensions, the mass of complete system, the down-time, etc.

The technical design is illustrated schematically in Figure B.1. As described in Section 4.2.2, a cold inner vacuum chamber is mounted inside a warm outer chamber. A turbomolecular pump TMP 1 evacuates the outer chamber, to create a thermal insulation vacuum for the inner chamber. A lower body of the inner chamber accommodates the stopping region. A turbomolecular pump TMP 2 is used for initial pumping down before the buffer gas is supplied, and during the vacuum chamber bake-out (see below). When buffer gas is supplied, its pressure is too high for TMP 2 operation. Therefore the TMP 2 is cut-off from the chamber by a cryogenic gate valve. An upper body of the inner chamber corresponds to the extraction region. It is pumped down by a turbomolecular pump TMP 3 similarly to the lower body. During the CSC operation, it is cut-off from the chamber by a corresponding gate-valve, and the buffer gas flows to a Helium Recovery Unit (HRU). The HRU recycles and purifies buffer gas, and feeds it back to the stopping region. A cooling of the buffer gas line and inner chamber is provided by an array of cryocoolers connected to a top flange of the inner chamber via flexible copper braids. The upper and lower bodies are separated by a plate which provides mechanical support to a first-stage RF carpet. The electrode systems (not shown) *e.g.*, DC cage, RF carpets, detectors, etc. are interfaced with the corresponding electronics via electrical vacuum feedthroughs. The feedthroughs which supply high voltage of several kV to the stopping region are isolated from the extraction region. This is done in order to avoid electrical breakdown – at pressures of 3–10 mbar such high voltage is above the Paschen limit [Paschen, 1889]. Note that all connections for vacuum, cryogenic, electrodes and gas handling systems are located at the top flanges of inner and outer chambers in order to ensure the ease of maintenance.

The following subsections describe individual systems and related developments in more detail.

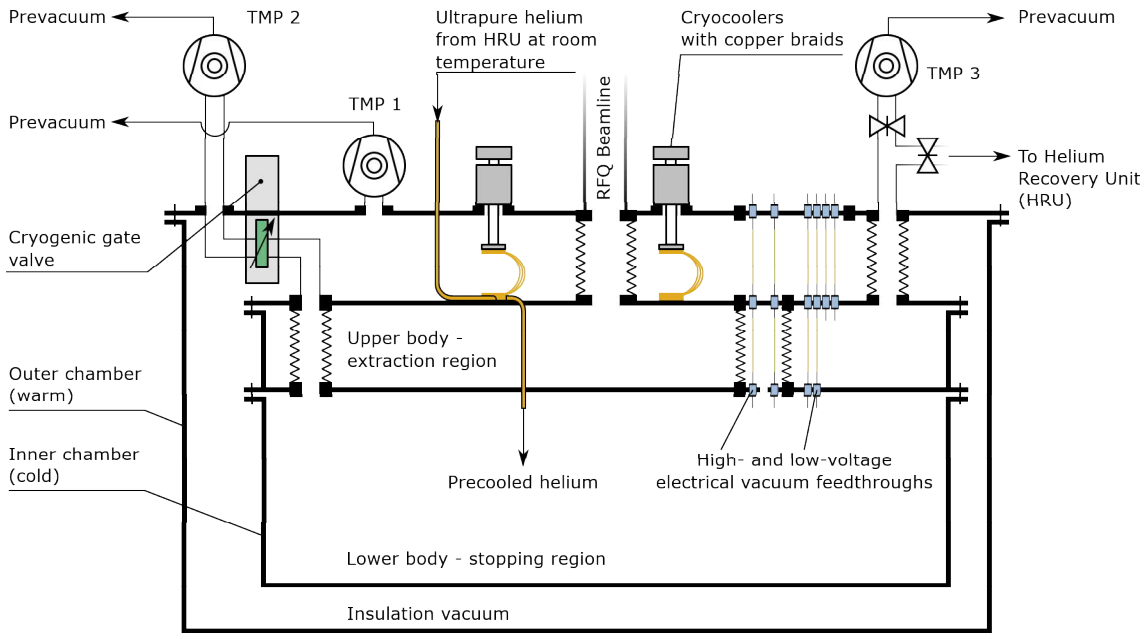

Figure B.1: Schematic figure of technical design of the CSC. See text for details.

B.1 DC cage and RF carpets

The width and height of the DC cage of 400 mm and 300 mm accordingly will accommodate a large beam spot of 300×200 mm. In addition, it will allow placing auxiliary instrumentation for diagnostics purposes without obscuring the beam path. All four side faces of the DC cage will be composed of strip electrodes which will form an overlapping pattern similar to the prototype CSC. The beam entrance and exit faces will be made out of thin foil strips. An electrode opposite to the 1st-stage RF carpet – the segmented anode – will coarsely repeat the structure of the RF carpet electrodes.

The first- and second-stage RF carpets will inherit design of the PCB-based multi-layer RF carpet used currently at the prototype CSC [Reiter, 2015]. It is a 5-layer design with a layer of electrodes that faces the ions, two inner layers that control field penetration, an electric component layer, and a shielding layer behind the nozzle exit on the opposite side of the RF carpet. Both RF carpets will cover a rectangular area with a width of 250 mm and length of 2000 mm. The first-stage RF carpet will consist of several identical segments. Each segment will have a concentric ring electrodes layout and a cylindrical nozzle. The electrode density will be 6 electrodes/mm. The second-stage RF carpet will also have a concentric ring electrodes layout, however, with a single nozzle at the center. The electrode density will be 2 electrodes/mm.

B.2 Vacuum chambers

Both, the inner and the outer chambers are of a cuboid shape. The inner dimensions in length, width and height are:

- Outer chamber – 2500×1200×1200 mm

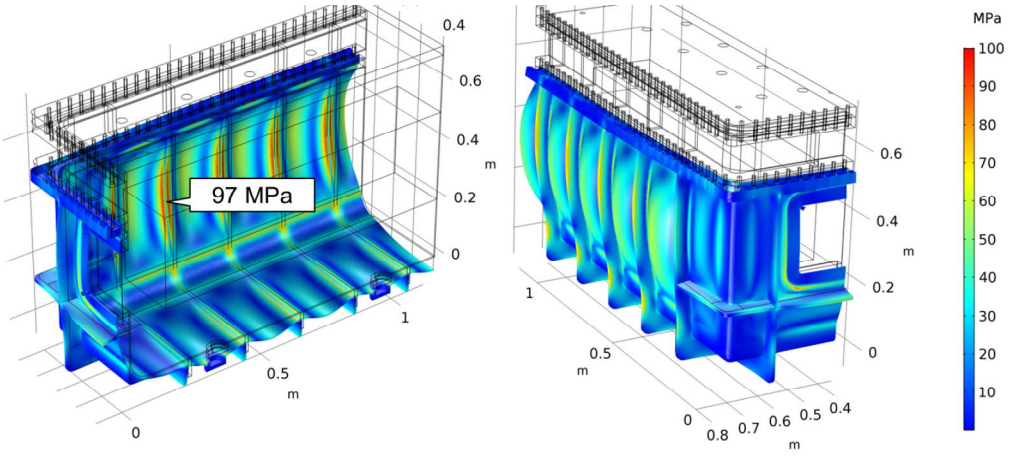

Figure B.2: Simulated von Mises stress distribution on the lower body of the inner chamber with a wall thickness of 4 mm at an overpressure of 1 bar and at temperature of 75 K. The resulting deformations are exaggerated by a factor of 50. The largest von Misses stress of 97 MPa is well below the tensile yield strength of aluminum 6061-T6 of 276 MPa.

- Inner chamber upper body – 2250×700×100 mm
- Inner chamber lower body – 2250×700×500 mm

The outer chamber and the lower body of the inner chamber have two beam windows, each located on the faces perpendicular to the beam axis. Such symmetric design allows for a larger experimental flexibility of the CSC. Dimensions of the beam windows of 300×200 mm match the size of a beam spot at the Super-FRS. All chambers are designed with reinforcement ribs. This increases the stiffness and, in addition, reduces the overall mass. The latter is beneficial for cooling and general handling of the system. Dimensions of the reinforcement ribs were selected such that they carry half of the mechanical load.

A material selected for all chambers is aluminum 6061-T6. The properties of aluminum are superior to conventionally used stainless steel. E.g., an order of magnitude larger thermal conductivity results in a uniform cooling or bake-out; a factor of 3 lower density reduces the cooling mass; few orders of magnitude lower outgasing rate is beneficial for the buffer gas cleanliness as it reduces the presence of contaminants such as H_2O, CO and CH_4. Moreover, results of the cooling down simulations performed for aluminum and stainless steel strongly suggest that aluminum is the material of choice (see Section B.3).

The inner and the outer chambers are required to withstand an overpressure of 1 bar. Note that this represents an extreme case. Under normal operational conditions the load will be much lower. The mechanical stability of vacuum chambers has been studied in simulations using COMSOL Multiphysics® 5.3 software [COMSOL Multiphysics®,]. The model is built by coupling modules responsible for solid mechanics and heat transfer in solids. The solid mechanics module considers linear elastic material, where vacuum chamber walls are gradually loaded until the desired pressure is reached. The heat transfer in solids module considers various sources of positive (heating) and negative (cooling) heat

flux. It reduces all mechanisms of heat transfer to thermal conduction. The module does not solve fluid flow, and therefore does not compute the convection heat transfer coefficient directly. Instead, the Nusselt number Nu is computed [Stephan and Atlas, 2010]. It is a function of many parameters of the heat exchange process and geometry, and its analytical description only exists for special cases. Nu is defined as the ratio of total heat flux hL to conductive heat flux k. The product of known conductive heat flux and computed Nusselt number yields an equivalent conductivity which accounts for the convective heat flux $hL = k \cdot Nu$. Radiative heat transfer is modeled as a positive heat flux across corresponding boundaries. The coupling between the modules ensures that the dependence of mechanical properties on temperature is taken into account. Symmetries of a vacuum chamber geometry were exploited to reduce the model size.

A wall thickness of the vacuum chambers has been varied in the simulations. For each case the von Mises stress has been computed and used as an evaluation criterion. The von Mises stress σ_v is a value used to determine if a given material will yield *i.e.*, will not return to its original shape after the load is removed [Budynas and Nisbett,]. It is mostly used for ductile materials, such as metals. It is a function of tensile and shear stress components, and allows the most complicated stress situation to be represented by a single quantity, the von Mises stress. It is then can be compared against the yield strength of the material under simple tension (the tensile yield strength S_y). Figure B.2 shows calculated distribution of the von Mises stress on the lower body of the inner chamber with 4-mm-thick walls at overpressure of 1 bar and at temperature of 75 K. The resulting deformations are purposely exaggerated by a factor of 50 to clearly show the shape. The largest von Misses stress of $\sigma_v = 97$ MPa under extreme load is by a factor of 2.8 lower than the tensile yield strength of aluminum 6061-T6 of $S_y = 276$ MPa. Similar analysis has been performer for the outer chamber. The results indicate that the vacuum chambers with proposed geometry satisfy the aforementioned load requirements. Wall thickness of 4 mm has been selected as a reasonable compromise between the mechanical stability and the overall mass.

A spring-energized metal gasket will be used to seal the inner chamber since it is applicable at cryogenic temperature and tolerates related thermal contractions. The outer chamber will be sealed by a regular Viton® sealing. The complete inner chamber is mounted suspended from the top flange of the outer chamber.

B.3 Cryogenic cooling system

A cryogenic cooling system of the inner chamber and the buffer gas will be based on Stirling cryocoolers, such as the CryoTel® DS 30 cryocooler (Sunpower, Inc.). An array of such coolers will be attached to the top flange of the inner chamber via oxygen-free flexible copper braids. Although their cooling power of 32 W at 77 K is about a factor of 5 lower compared to analogues *i.e.*, Gifford-McMahon (GM) or Pulse Tube (PT) single-stage cryocoolers, CryoTel® DS 30 coolers offer unique characteristics advantageous to the CSC. The most decisive ones are a maintenance-free operation, and a possibility of a bake-out.

The bake-out is a process when a vacuum chamber is heated to and held at tem-

perature above 100 °C for several hours under continuous pumping down. This accelerates desorption of volatile contaminants such as water and hydrocarbons from the surfaces of the vacuum chamber, and thus tremendously improves the cleanliness. In contrast to analogues, the CryoTel® DS 30 cryocoolers are driven by a *built-in* compressor, and therefore a complete unit is water-cooled. This allows exposing it to high temperatures without damaging the unit *e.g.*, during the vacuum chamber bake-out. For reference, conventional cryocoolers can be heated up to about 50 °C.

The number of cryocoolers has been optimized with respect to the cooling time. As the first step, a heat input budget has been calculated. The following describes the sources of heat load and methods of their evaluation.

A buffer gas heat input was deduced as

$$\dot{q}_{\mathrm{He}} = \dot{m} C_P \Delta T,$$

where $\dot{m} = 0.128$ g/s is mass flow of He through 8 nozzles calculated from a throughput of a thin orifice with a diameter of 0.6 mm, $C_p = 5.19$ J/(g · K) is a heat capacity of He at standard conditions (assumed to be constant over the temperature range), and $\Delta T = (300 - 70)$ K is a temperature difference. The heat load generated by an RF carpet was scaled from the RF carpet of the prototype CSC.

In order to minimize the heat load from radiative heat exchange, a multi-layer insulation (MLI) between inner and outer chamber will be used. The corresponding heat load was calculated as:

$$\dot{q}_{\mathrm{r}} = \sigma_{\mathrm{SB}} \frac{\varepsilon}{(2-\varepsilon)\cdot(n+1)} A \left(T_h^4 - T_c^4\right),$$

where $\sigma_{\mathrm{SB}} = 5.67 \cdot 10^{-8}\,\mathrm{W/(m^2 \cdot K^4)}$ is the Stefan–Boltzmann constant, $\varepsilon = 0.1$ is the emissivity of polished metal, $n = 30$ is the number of MLI layers, $A = 9.92\,\mathrm{m^2}$ is the surface area, and $T_h = 300\,\mathrm{K}, T_c = 70\,\mathrm{K}$ are the temperatures of hot and cold surfaces correspondingly.

The heat load from suspension system and electrical wires was estimated using a thermal conductivity integral method to take into account strong temperature dependence of thermal conductivity $K(T)$. Here, for a body with a length l, and a uniform cross-sectional area A, the heat load is

$$\dot{q} = \frac{A}{l} \left(\Theta(T_1) - \Theta(T_2)\right),$$

where $\Theta(T_i) = \int_0^{T_i} K(T) dT$, (W/m) is a thermal conductivity integral. The values of $\Theta(T_i)$ for various materials are tabulated *e.g.*, in [Weisend, 1998]. The input parameters and results are shown in Table B.1.

The inner chamber almost entirely constitutes the cold mass. Table B.2 summarizes the heat input budget.

Next, the heat input budget was set up in the COMSOL model described above (Sec. B.2), and the cooling down of the CSC has been simulated with different number of cryocoolers. A dependence of cooling power of DS30 cryocoolers on temperature was taken into account. The study has been performed for the inner

Table B.1: Estimated heat load from suspension system and electrical wires. Slender stainless steel rods for suspension system, and small diameters of electrical wires are selected to minimize the heat load. Manganin is an alloy with low thermal conductivity, and is considered for cables of the regular electrodes. For cabling the RF carpets and motors, the copper cables will be used. The values of thermal conductivity integrals $\Theta(T_i)$ are taken from [Weisend, 1998].

	Suspension system	Electrical wires	
Material	Stainless steel	Manganin	Copper
Diameter, mm	8	0.14	0.25
Average length, m	1	0.4	0.4
Number of elements	16	250	40
$\Theta(300K)$, W/m	3000	4000	120000
$\Theta(77K)$, W/m	220	450	45000
Heat load, W	2.2	0.03	0.37
Total heat load, W	**2.2**	**0.40**	

chamber made of aluminum or stainless steel. The results are shown in Figure B.3 for inner chamber made of (a) aluminum 6061-T6 and (b) stainless steel 304, cooled with 10 (black), 16 (red), 30 (blue) and 40 (green) cryocoolers. A scenario when the buffer gas reaches a temperature of 70 K in 24 hours has been defined as optimal. The results suggest that the optimal cooling down can be achieved with 16 cryocoolers in the inner chamber built from aluminum (Fig B.3a). Smaller number of cryocoolers will result in a significant increase in cooling down time. Using 10 cryocoolers or less is insufficient to achieve a temperature of 70 K. Increase in the number of cryocoolers above optimum results in proportionally faster cooling. When using more than 30 cryocoolers, the gain in cooling performance does not justify the resulting costs and complexity of the system.

In case of the stainless steel inner chamber (Fig B.3b), the optimal cooling requires more than twice the number of cryocoolers. Increasing the number further does not improve the cooling performance significantly.

B.4 Gas handling system

The gas handling system of the CSC will consist of the following modules:

Pumping down: turbomolecular pumps evacuate the CSC (TMP 1-3 on Figure B.1), the RFQ beamline, and a Helium Recovery Unit (see next) before it is filled with buffer gas or during the bake-out.

Helium Recovery Unit (HRU): under the operating conditions planned for the CSC, buffer gas consumption is a critical limiting factor. A commercial gas bundle of ultra-pure helium – 12 gas cylinders with a volume of 50 liters each and at a pressure of 200 bar – will be fully consumed in ∼2.5 days of continuous operation

Table B.2: Estimated heat input budget for the CSC. For the cold mass, the inner chamber made out of aluminum is given.

Heat source	Heat load, W
Circulating buffer gas	160
RF carpet	100
Radiative heat	7
Suspension system	3
Electrical wires	<1
Total heat load	**270**
Cold mass (inner chamber)	337 kg

of the CSC in standard mode. The costs associated with purchasing new gas bundles will quickly become unbearable. Moreover, the presence of impurities *e.g.*, noble gases other than helium, and their concentrations vary depending on how the gas cylinders have been used in the past [Mollaebrahimi, 2021]. Therefore, replacing bundles within one experimental run has to be avoided. This is unfeasible at such a high gas consumption rate. For reference, the prototype CSC at the highest areal density of 10 mg/cm^2 depletes the gas bundle in about 3 weeks.

A Helium Recovery Unit (HRU) has been developed to address this issue. The HRU is a self-sufficient system which has been designed to recover more than 98% of buffer gas at a flow rate of 2 m^3/h. This will be achieved by (i) compressing helium exiting the extraction region from 3–10 mbar (70 K) to 700 mbar (room temperature) by roots pumps, (ii) further compressing helium to 4 bar by a membrane compressor, and (iii) feeding pressurized helium to the stopping region via a corresponding control valve. The HRU is described in detail in [State, 2022]. Given the estimated losses of helium of 0.16%, the HRU will enable a continuous operation of the CSC in standard mode for more than a month from a single gas cylinder. This translates into a year-long continuous operation form the gas bundle.

Control and regulation: a control system manages various hardware to reach desired operation conditions in the CSC and RFQ beamline. It will be based on a slow control system (SCS) recently developed and implemented at the FRS Ion Catcher at GSI. Besides hardware control, the SCS significantly improves the overall operational stability of the setup. E.g., in a series of offline tests at the FRS IC it has been demonstrated that stable ion extraction at full rate is possible under varying conditions of the buffer gas. The buffer gas was warmed up from 85 K to 120 K for over 6 hours while the SCS stabilized the areal density within $\pm$1% by regulating the buffer gas pressure. The benefits of such a remarkable stability for long data taking campaigns are clear. A detailed description of the SCS can be found in [State et al., 2022, Beck, 2023].

Cleaning and monitoring: as it has been discussed in Section 1.2, a level of buffer gas impurities of<1 ppb is a prerequisite for effective extraction of stopped ions of exotic nuclei. A commercial ultra-pure helium 6.0 – impurities are at a level

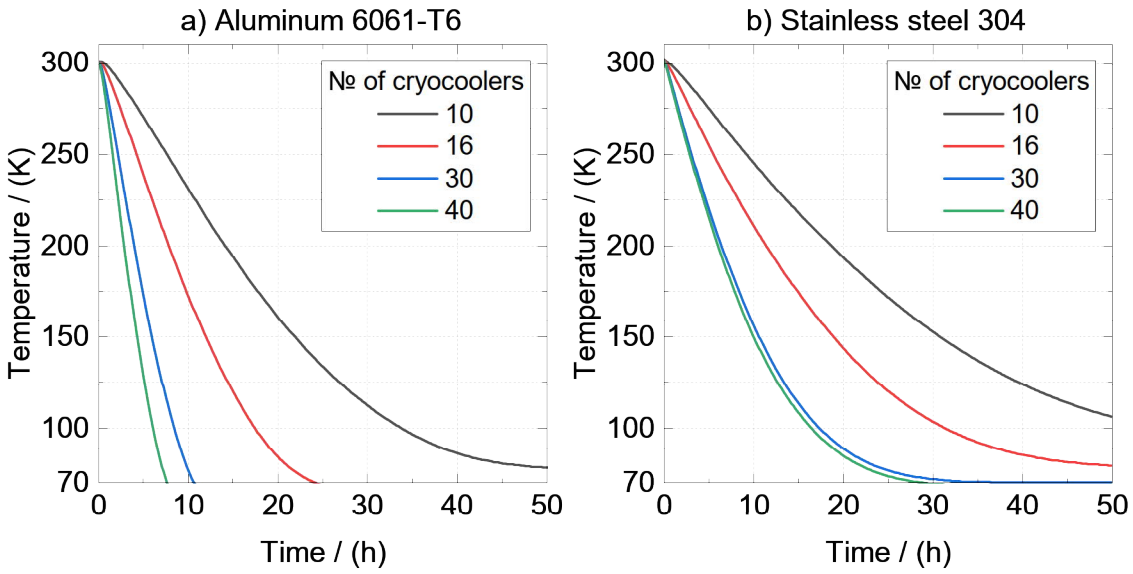

Figure B.3: Simulated cooling down of helium buffer gas in the CSC. The results are shown for inner chamber made of (a) aluminum 6061-T6 and (b) stainless steel 304, cooled with 10 (black), 16 (red), 30 (blue) and 40 (green) cryocoolers. Optimal cooling down time of 24 hours can be achieved with 16 cryocoolers in the inner chamber built from aluminum 6061-T6.

of 1000 ppb – will undergo additional purification stages before filling the CSC. These stages include the passive and active gas getters as well as a cold trap. The passive gas getter removes H_2O, O_2, CO, CO_2, H_2 and organic compounds to a level of <0.1 ppb by physical adsorption. The active getter offers in addition a removal of N_2 and all hydrocarbons to a <1 ppb level by chemical and physical absorption in a heated getter material. The GateKeeper® GPU IX and HGU (Entegris, Inc) are considered as the passive and active getters correspondingly. The noble gases cannot be removed by gas getters in principle, therefore the cold trap will be used to suppress them by adsorption at cryogenic temperatures. The cooling will be provided by a GT-cryocooler Sumitomo CH-208L. It will be temperature-regulated which will enable control over the noble gases suppression.

The cleanliness of the buffer gas entering the CSC will be constantly monitored by a moisture sensor on a ∼1 ppb level and an O_2 sensor on a 0.1 ppb level. In order to monitor the gas exiting the CSC, a residual gas analyzer (RGA) will be used.

The described solutions have been implemented and tested with the prototype CSC at the FRS Ion Catcher at GSI [Mollaebrahimi, 2021].

The gas cleaning and monitoring systems will be integrated in the HRU. The buffer gas will circulating in the HRU will by processed by the getters multiple times, and therefore its purity is expected to improve further.

Charge-state control: in purified helium stopped ions will survive in charge states of +1, +2, and even +3. Reducing charge state to +1 will be beneficial for an effective ion transport at the RF carpet, as its effective field $E_{\text{eff}} \propto 1/q$ (see Eq. A.17). This can be achieved by admixing trace amounts of gases other than

helium to the buffer gas. A dedicated gas line with a low-flow control valve and a matching gas getter will be utilized for this purpose. The process of selecting an appropriate gas and testing this concept remains to be completed.

Care has been taken to make sure that the components selected for the gas handling system are UHV-compatible and tolerate bake-out temperatures.

Bibliography

[Agostinelli et al., 2003] Agostinelli, S., Allison, J., Amako, K. a., Apostolakis, J., Araujo, H., Arce, P., Asai, M., Axen, D., Banerjee, S., Barrand, G., et al. (2003). Geant4—a simulation toolkit. *Nuclear instruments and methods in physics research section A: Accelerators, Spectrometers, Detectors and Associated Equipment*, 506(3):250–303.

[Ahlen, 1982] Ahlen, S. P. (1982). Calculation of the relativistic bloch correction to stopping power. *Physical Review A*, 25(4):1856.

[Ajayakumar et al., 2023] Ajayakumar, A., Romans, J., Authier, M., Balasmeh, Y., Brizard, A., Boumard, F., Caceres, L., Cam, J.-F., Claessens, A., Damoy, S., et al. (2023). In-gas-jet laser spectroscopy with S3-LEB. *Nuclear Instruments and Methods in Physics Research Section B: Beam Interactions with Materials and Atoms*, 539:102–107.

[Al-Adili et al., 2015] Al-Adili, A., Jansson, K., Lantz, M., Solders, A., Gorelov, D., Gustavsson, C., Mattera, A., Moore, I., Prokofiev, A., Rakopoulos, V., et al. (2015). Simulations of the fission-product stopping efficiency in IGISOL. *The European Physical Journal A*, 51:1–7.

[Angert and Schmelzer, 1969] Angert, N. and Schmelzer, C. (1969). The UNILAC, a variable energy linear accelerator for atomic ions of any mass. *Kerntech.*, 11:690–695.

[ANSYS Fluent,] ANSYS Fluent. Fluid Simulations Software https://www.ansys.com/products/fluids/ansys-fluent.

[Arai et al., 2014] Arai, F., Ito, Y., Wada, M., Schury, P., Sonoda, T., and Mita, H. (2014). Investigation of the ion surfing transport method with a circular rf carpet. *International Journal of Mass Spectrometry*, 362:56–58.

[Ärje et al., 1985] Ärje, J., Äysto, J., Hyvönen, H., Taskinen, P., Koponen, V., Honkanen, J., Hautojärvi, A., and Vierinen, K. (1985). Submillisecond on-line mass separation of nonvolatile radioactive elements: An application of charge exchange and thermalization processes of primary recoil ions in helium. *Phys. Rev. Lett.*, 54:99–101.

[Ärje and Valli, 1981] Ärje, J. and Valli, K. (1981). Helium-jet ion guide for an on-line isotope separator. *Nucl. Instrum. Methods*, 179:535–539.

[Audi et al., 2017] Audi, G., Kondev, F. G., Wang, M., Huang, W. J., and Naimi, S. (2017). The NUBASE2016 evaluation of nuclear properties. *Chinese Phys. C*, 41(3):030001.

[Aumann, 2007] Aumann, T. (2007). Prospects of nuclear structure at the future GSI accelerators. *Prog. Part. Nucl. Phys.*, 59(1):3–21.

[Ayet San Andrés, 2018] Ayet San Andrés, S. (2018). *Developments for Multiple-Reflection Time-of-Flight Mass Spectrometers and Their Application to High-Resolution Accurate Mass Measurements of Short-Lived Exotic Nuclei*. PhD thesis, Justus Liebig University Gießen.

[Ayet San Andrés et al., 2019] Ayet San Andrés, S., Hornung, C., Ebert, J., Plaß, W. R., Dickel, T., Geissel, H., Scheidenberger, C., Bergmann, J., Greiner, F., Haettner, E., et al. (2019). High-resolution, accurate multiple-reflection time-of-flight mass spectrometry for short-lived, exotic nuclei of a few events in their ground and low-lying isomeric states. *Phys. Rev. C*, 99:064313.

[Äystö et al., 2016] Äystö, J., Behr, K.-H., Benlliure, J., Bracco, A., Egelhof, P., Fomichev, A., Galès, S., Geissel, H., Grahn, T., Grigorenko, L., et al. (2016). Experimental program of the super-frs collaboration at fair and developments of related instrumentation. *Nuclear Instruments and Methods in Physics Research Section B: Beam Interactions with Materials and Atoms*, 376:111–115.

[Beck, 2023] Beck, S. T. (2023). *Direct mass measurements of neutron-deficient lanthanides for nuclear structure studies at the proton dripline*. PhD thesis, Justus-Liebig-Universität Gießen.

[Bergmann, 2023] Bergmann, J. (2023). *High-resolution tandem mass spectrometry of complex mixtures with a multiple-reflection time-of-flight mass-spectrometer*. PhD thesis, Justus-Liebig-Universität Gießen.

[Bethe, 1932] Bethe, H. (1932). Bremsformel für elektronen relativistischer Geschwindigkeit. *Zeitschrift für Physik*, 76(5-6):293–299.

[Blasche and Franczak, 1992] Blasche, K. and Franczak, B. (1992). The heavy ion synchrotron SIS. In *Proc. EPAC*, page 9.

[Blaum, 2006] Blaum, K. (2006). High-accuracy mass spectrometry with stored ions. *Phys. Rep.*, 425:1–78.

[Blazhev et al., 2004] Blazhev, A., Górska, M., Grawe, H., Nyberg, J., Palacz, M., Caurier, E., Dorvaux, O., Gadea, A., Nowacki, F., Andreoiu, C., de Angelis, G., Balabanski, D., Beck, C., Cederwall, B., Curien, D., Döring, J., Ekman, J., Fahlander, C., Lagergren, K., Ljungvall, J., Moszyński, M., Norlin, L.-O., Plettner, C., Rudolph, D., Sohler, D., Spohr, K. M., Thelen, O., Weiszflog, M., Wisell, M., Wolińska, M., and Wolski, W. (2004). Observation of a core-excited $e4$ isomer in $^{98}\mathrm{Cd}$. *Physical Review C*, 69(6):064304.

[Bloch, 1933] Bloch, F. (1933). Zur Bremsung rasch bewegter Teilchen beim Durchgang durch Materie. *Annalen der Physik*, 408(3):285–320.

[Block et al., 2010] Block, M., Ackermann, D., Blaum, K., Droese, C., Dworschak, M., Eliseev, S., Fleckenstein, T., Haettner, E., Herfurth, F., Heßberger, F. P., Hofmann, S., Ketelaer, J., Ketter, J., Kluge, H.-J., Marx, G., Mazzocco, M., Novikov, Y. N., Plaß, W. R., Popeko, A., Rahaman, S., Rodriguez, D., Scheidenberger, C., Schweikhard, L., Thirolf, P. G., Vorobjev, G. K., and Weber, C. (2010). Direct mass measurements above uranium bridge the gap to the island of stability. *Nature*, 463(08774):785–788.

[Block et al., 2022] Block, M., Giacoppo, F., Heßberger, F.-P., and Raeder, S. (2022). Recent progress in experiments on the heaviest nuclides at SHIP. *La Rivista del Nuovo Cimento*, pages 1–45.

[Bohr, 1913] Bohr, N. (1913). II. On the theory of the decrease of velocity of moving electrified particles on passing through matter. *The London, Edinburgh, and Dublin Philosophical Magazine and Journal of Science*, 25(145):10–31.

[Bollen, 2011] Bollen, G. (2011). "Ion surfing" with radiofrequency carpets. *Int. J. Mass Spetrom.*, 299:131–138.

[Borer et al., 1974] Borer, J., Bramham, P., Schnell, W., Hübner, K., Hereward, H. G., and Thorndahl, L. (1974). Non-destructive diagnostics of coasting beams with schottky noise. Technical report, CM-P00063743.

[Brodeur et al., 2013] Brodeur, M., Gehring, A., Bollen, G., Schwarz, S., and Morrissey, D. (2013). Experimental investigation of the ion surfing transport method. *Int. J. Mass Spetrom.*, 336:53–60.

[Brown et al., 2018] Brown, D. A., Chadwick, M., Capote, R., Kahler, A., Trkov, A., Herman, M., Sonzogni, A., Danon, Y., Carlson, A., Dunn, M., et al. (2018). Endf/b-viii. 0: The 8th major release of the nuclear reaction data library with cielo-project cross sections, new standards and thermal scattering data. *Nuclear Data Sheets*, 148:1–142.

[Budynas and Nisbett,] Budynas, R. and Nisbett, K. Shigley's Mechanical engineering design.

[Burkey et al., 2022] Burkey, M., Savard, G., Gallant, A., Scielzo, N., Clark, J., Hirsh, T., Varriano, L., Sargsyan, G., Launey, K., Brodeur, M., et al. (2022). Improved limit on tensor currents in the weak interaction from li 8 β decay. *Physical Review Letters*, 128(20):202502.

[Chen et al., 2009] Chen, L., Litvinov, Y. A., Plaß, W. R., Beckert, K., Beller, P., Bosch, F., Boutin, D., Caceres, L., Cakirli, R. B., Carroll, J. J., Casten, R. F., Chakrawarthy, R. S., Cullen, D. M., Cullen, I. J., Franzke, B., Geissel, H., Gerl, J., Górska, M., Jones, G. A., Kishada, A., Knöbel, R., Kozhuharov, C., Litvinov, S. A., Liu, Z., Mandal, S., Montes, F., Münzenberg, G., Nolden, F., Ohtsubo, T., Patyk, Z., Podolyák, Z., Propri, R., Rigby, S., Saito, N., Saito, T., Scheidenberger, C., Shindo, M., Steck, M., Ugorowski, P., Walker, P. M., Williams, S., Weick, H., Winkler, M., Wollersheim, H.-J., and Yamaguchi, T. (2009). Schottky mass measurement of the ^{208}Hg isotope: Implications for the proton-neutron interaction strength around the doubly magic ^{208}Pb. *Phys. Rev. Lett.*, 102:122503.

[Cocolios et al., 2009] Cocolios, T. E., Andreyev, A., Bastin, B., Bree, N., Büscher, J., Elseviers, J., Gentens, J., Huyse, M., Kudryavtsev, Y., Pauwels, D., et al. (2009). Magnetic dipole moment of cu 57, 59 measured by in-gas-cell laser spectroscopy. *Physical Review Letters*, 103(10):102501.

[COMSOL Multiphysics®,] COMSOL Multiphysics®. www.comsol.com, COMSOL AB, Stockholm, Sweden.

[Cuillerier and Stanić, 2019] Cuillerier, A. and Stanić, G. (2019). Numerical calculations for the CSC's efficiency. Internal report, Justus-Liebig-Universität Gießen.

[Cwiok et al., 1987] Cwiok, S., Nazarewicz, W., Dudek, J., Skalski, J., and Werner, T. (1987). Single-particle energies, wave functions, quadrupole moments and g-factors in an axially deformed woods-saxon potential with applications to the two-centre-type nuclear problems. *Comp. Phys. Comm.*, 46:379.

[Dasso et al., 1994] Dasso, C., Pollarolo, G., and Winther, A. (1994). Systematics of isotope production with radioactive beams. *Physical review letters*, 73(14):1907.

[Datz et al., 1996] Datz, S., Krause, H., Vane, C., Knudsen, H., Grafström, P., and Schuch, R. (1996). Effect of nuclear size on the stopping power of ultrarelativistic heavy ions. *Physical review letters*, 77(14):2925.

[de Jong et al., 1997] de Jong, M., Ignatyuk, A. V., and Schmidt, K.-H. (1997). Angular momentum in peripheral fragmentation reactions. *Nucl. Phys. A*, 613(4):435–444.

[De Voigt et al., 1983] De Voigt, M. J. A., Dudek, J., and Szymański, Z. (1983). High-spin phenomena in atomic nuclei. *Rev. Mod. Phys.*, 55(4):949.

[Dehmelt, 1967] Dehmelt, H. G. (1967). Radiofrequency spectroscopy of stored ions I: Storage. *Adv. At. Mol. Phys.*, 3:53–72.

[Dendooven et al., 2006] Dendooven, P., Purushothaman, S., and Gloos, K. (2006). On a cryogenic noble gas ion catcher. *Nucl. Instrum. Methods A*, 558:580–583.

[Dickel, 2010] Dickel, T. (2010). *Design and Commissioning of an Ultra-High-Resolution Time-of-Flight Based Isobar Separator and Mass Spectrometer*. PhD thesis, Justus Liebig University Gießen.

[Dickel et al., 2019] Dickel, T., Ayet San Andres, S., Beck, S., Bergmann, J., Dilling, J., Greiner, F., Hornung, C., Jacobs, A., Kripko-Koncz, G., Kwiatkowski, A., et al. (2019). Recent upgrades of the multiple-reflection time-of-flight mass spectrometer at TITAN, TRIUMF. *Hyperfine Interact.*, 240.

[Dickel et al., 2017] Dickel, T., Constantin, P., Winfield, J., Ayet, S., Bagchi, S., Balabanski, D., Beck, S., Geissel, H., Greiner, F., Haettner, E., Heinz, S., Hornung, C., Karpov, A., Kostyleva, D., Kuzminchuk, N., Kindler, B., Lommel, B.,

Mardor, I., Miskun, I., Mukha, I., Münzenberg, G., Pietri, S., Martinez-Pinedo, G., Plaß, W., Prochazka, A., Purushothaman, S., Rappold, C., Saiko, V., Saito, T., Scheidenberger, C., Tanaka, Y., and Weick, H. (2017). Reaction studies with the FRS Ion Catcher: A novel approach and universal method for the production, identification of and experiments with unstable isotopes produced in multi-nucleon transfer reactions with stable and unstable beams. *Proposal to the G-PAC for FAIR Phase-0 Experiments, GSI Darmstadt*.

[Dickel et al., 2023] Dickel, T., Hornung, C., Amanbayev, D., San Andrés, S. A., Beck, S., Bergmann, J., Geissel, H., Gerl, J., Górska, M., Gröf, L., et al. (2023). Mean range bunching of exotic nuclei produced by in-flight fragmentation and fission—Stopped-beam experiments with increased efficiency. *Nuclear Instruments and Methods in Physics Research Section B: Beam Interactions with Materials and Atoms*, 541:275–278.

[Dickel et al., 2020] Dickel, T., Kankainen, A., Spătaru, A., Amanbayev, D., Beliuskina, O., Beck, S., Constantin, P., Benyamin, D., Geissel, H., Gröf, L., et al. (2020). Multi-nucleon transfer reactions at ion catcher facilities-a new way to produce and study heavy neutron-rich nuclei. In *Journal of Physics: Conference Series*, volume 1668, page 012012. IOP Publishing.

[Dickel et al., 2015a] Dickel, T., Plaß, W. R., Ayet San Andrés, S., Ebert, J., Geissel, H., Haettner, E., Hornung, C., Miskun, I., Pietri, S., Purushothaman, S., Reiter, M. P., Rink, A. K., Scheidenberger, C., Weick, H., Dendooven, P., Diwisch, M., Greiner, F., Heiße, F., Knöbel, R., Lippert, W., Moore, I. D., Pohjalainen, I., Prochazka, A., Ranjan, M., Takechi, M., Winfield, J. S., and Xu, X. (2015a). First spatial separation of a heavy ion isomeric beam with a multiple-reflection time-of-flight mass spectrometer. *Phys. Lett. B*, 744:137–141.

[Dickel et al., 2015b] Dickel, T., Plaß, W. R., Becker, A., Czok, U., Geissel, H., Haettner, E., Jesch, C., Kinsel, W., Petrick, M., Scheidenberger, C., and Yavor, M. I. (2015b). A high-performance multiple-reflection time-of-flight mass spectrometer and isobar separator for the research with exotic nuclei. *Nucl. Instrum. Methods A*, 777:172–188.

[Dickel et al., 2016] Dickel, T., Plaß, W. R., Geissel, H., Heiße, F., Miskun, I., Purushothaman, S., Reiter, M. P., Rink, A.-K., and Scheidenberger, C. (2016). Conceptional design of a novel next-generation cryogenic stopping cell for the Low-Energy Branch of the Super-FRS. *Nucl. Instrum. Methods B*, 376:216–220.

[Dickel et al., 2014] Dickel, T., Plaß, W. R., Reiter, P., Geissel, H., and Scheidenberger, C. (2014). Conceptual design of a next-generation cryogenic stopping cell for the Low-Energy Branch of the Super-FRS. *GSI Scientific Report 2013*, page 106.

[Dilling et al., 2018] Dilling, J., Blaum, K., Brodeur, M., and Eliseev, S. (2018). Penning-trap mass measurements in atomic and nuclear physics. *Annual Review of Nuclear and Particle Science*, 68:45–74.

[Dimitriou et al., 2016] Dimitriou, P., Hambsch, F., and Pomp, S. (2016). Fission yields: current status & perspective.

[Droese et al., 2014] Droese, C., Eliseev, S., Blaum, K., Block, M., Herfurth, F., Laatiaoui, M., Lautenschläger, F., Ramirez, E. M., Schweikhard, L., Simon, V. V., and Thirolf, P. G. (2014). The cryogenic gas stopping cell of SHIPTRAP. *Nucl. Instrum. Methods B*, 338:126–138.

[Dudek et al., 1981] Dudek, J., Szymański, Z., and Werner, T. (1981). Woods-saxon potential parameters optimized to the high spin spectra in the lead region. *Phys. Rev. C*, 23(2):920.

[Duflo and Zuker, 1995] Duflo, J. and Zuker, A. (1995). Microscopic mass formulas. *Phys. Rev. C*, 52(1):R23–R27.

[Dworschak et al., 2010] Dworschak, M., Block, M., Ackermann, D., Audi, G., Blaum, K., Droese, C., Eliseev, S., Fleckenstein, T., Haettner, E., Herfurth, F., et al. (2010). Penning trap mass measurements on nobelium isotopes. *Physical Review C*, 81(6):064312.

[Ebert, 2016] Ebert, J. (2016). *Mass Measurements of ^{238}U-Projectile Fragments for the First Time with a Multiple-Reflection Time-Of-Flight Mass Spectrometer*. PhD thesis, Justus Liebig University Gießen.

[Eliseev et al., 2013] Eliseev, S., Blaum, K., Block, M., Droese, C., Goncharov, M., Ramirez, E. M., Nesterenko, D. A., Novikov, Y. N., and Schweikhard, L. (2013). Phase-imaging ion-cyclotron-resonance measurements for short-lived nuclides. *Phys. Rev. Lett.*, 110:082501.

[Elomaa, 2009] Elomaa, V.-V. (2009). Mass measurements for explosive nucleosynthesis in stars. *Research report/Department of Physics, University of Jyväskylä*, (11/2009).

[ENSDF, 2020] ENSDF (2020). ENSDF database as of October, 2020. https://www.nndc.bnl.gov/ensarchivals/.

[Ferrer et al., 2017] Ferrer, R., Barzakh, A., Bastin, B., Beerwerth, R., Block, M., Creemers, P., Grawe, H., de Groote, R., Delahaye, P., Fléchard, X., et al. (2017). Towards high-resolution laser ionization spectroscopy of the heaviest elements in supersonic gas jet expansion. *Nature communications*, 8(1):14520.

[Ferrer et al., 2014] Ferrer, R., Bree, N., Cocolios, T. E., Darby, I., De Witte, H., Dexters, W., Diriken, J., Elseviers, J., Franchoo, S., Huyse, M., et al. (2014). In-gas-cell laser ionization spectroscopy in the vicinity of 100sn: Magnetic moments and mean-square charge radii of n= 50–54 ag. *Physics Letters B*, 728:191–197.

[Franzke, 1987] Franzke, B. (1987). The heavy ion storage and cooler ring project ESR at GSI. *Nucl. Instrum. Methods B*, 24/25:18–25.

[Franzke et al., 1995] Franzke, B., Beckert, K., Eickhoff, H., Nolden, F., Reich, H., Schaaf, U., Schlitt, B., Schwinn, A., Steck, M., and Winkler, T. (1995). Schottky mass spectrometry at the experimental storage ring esr. *Physica Scripta*, 1995(T59):176.

[Freedman and Diaconis, 1981] Freedman, D. and Diaconis, P. (1981). On the histogram as a density estimator:L2 theory. *Z. Wahrscheinlichkeit.*, 57(4):453–476.

[Gabrielse, 2009] Gabrielse, G. (2009). Why is sideband mass spectrometry possible with ions in a Penning trap. *Phys. Rev. Lett.*, 102:172501.

[Gaimard and Schmidt, 1991] Gaimard, J.-J. and Schmidt, K.-H. (1991). A reexamination of the abrasion-ablation model for the description of the nuclear fragmentation reaction. *Nucl. Phys. A*, 531(3-4):709–745.

[Garcia et al., 2017] Garcia, F., Turpeinen, R., Äystö, J., Grahn, T., Rinta-Antila, S., Jokinen, A., Voss, B., Kunkel, J., Kleipa, V., Risch, H., Caesar, C., Simons, C., Prochazka, A., Schmidt, C. J., Hoffmann, J., I., R., and H., K. N. H. (2017). Twin GEM-TPC prototype (HGB4) beam test at GSI - a tracking detector for the Super-FRS. *GSI Sci. Rep. 2016*, 2017-1:475 p.

[Geissel et al., 1992] Geissel, H., Armbruster, P., Behr, K. H., Brünle, A., Burkard, K., Chen, M., Folger, H., Franczak, B., Keller, H., Klepper, O., Langenbeck, B., Nickel, F., Pfeng, E., Pfützner, M., Roeckl, E., Rykaczewski, K., Schall, I., Schardt, D., Scheidenberger, C., Schmidt, K. H., Schröter, A., Schwab, T., Sümmerer, K., Weber, M., Münzenberg, G., Brohm, T., Clerc, H. G., Fauerbach, M., Gaimard, J. J., Grewe, A., Hanelt, E., Knödler, B., Steiner, M., Voss, B., Weckenmann, J., Ziegler, C., Magel, A., Wollnik, H., Dufour, J. P., Fujita, Y., Vieira, D. J., and Sherrill, B. (1992). The GSI projectile fragment separator (FRS): a versatile magnetic system for relativistic heavy ions. *Nucl. Instrum. Methods B*, 70(1-4):286 – 297.

[Geissel et al., 2006] Geissel, H., Knöbel, R., Litvinov, Y. A., Sun, B., Beckert, K., Beller, P., Bosch, F., Boutin, D., Brandau, C., Chen, L., Fabian, B., Hausmann, M., Kozhuharov, C., Kurcewicz, J., Litvinov, S. A., Mazzocco, M., Montes, F., Münzenberg, G., Musumarra, A., Nociforo, C., Nolden, F., Plaß, W. R., Scheidenberger, C., Steck, M., Weick, H., and Winkler, M. (2006). A new experimental approach for isochronous mass measurement of short-lived exotic nuclei with the FRS-ERS facility. *Hyperfine Interact.*, 173:49–54.

[Geissel et al., 2004] Geissel, H., Litvinov, Y., Attallah, F., Beckert, K., Beller, P., Bosch, F., Boutin, D., Faestermann, T., Falch, M., Franzke, B., Hausmann, M., Hellström, M., Kaza, E., Kerscher, T., Klepper, O., Kluge, H.-J., Kozhuharov, C., Kratz, K.-L., Litvinov, S., Löbner, K., Maier, L., Matoš, M., Münzenberg, G., Nolden, F., Novikov, Y., Ohtsubo, T., Ostrowski, A., Patyk, Z., Pfeiffer, B., Portillo, M., Radon, T., Scheidenberger, C., Shishkin, V., Stadlmann, J., Steck, M., Viera, D., Weick, H., Winkler, M., Wollnik, H., and Yamaguchi, T. (2004). New results with stored exotic nuclei at relativistic energies. *Nuclear Physics A*,

746:150–155. Proceedings of the Sixth International Conference on Radioactive Nuclear Beams (RNB6).

[Geissel et al., 1995] Geissel, H., Münzenberg, G., and Riisager, K. (1995). Secondary exotic nuclear beams. *Annu. Rev. Nucl. Part. Sci.*, 45:163–203.

[Geissel and Scheidenberger, 1998] Geissel, H. and Scheidenberger, C. (1998). Slowing down of relativistic heavy ions and new applications. *Nuclear Instruments and Methods in Physics Research Section B: Beam Interactions with Materials and Atoms*, 136:114–124.

[Geissel et al., 1989] Geissel, H., Schwab, T., Armbruster, P., Dufour, J., Hanelt, E., Schmidt, K.-H., Scherrill, B., and Münzenberg, G. (1989). Ions penetrating through ion-optical systems and matter - non-Liouvillian phase-space modelling. *Nucl. Instrum. Methods A*, 282:247–260.

[Geissel et al., 2002] Geissel, H., Weick, H., Scheidenberger, C., Bimbot, R., and Gardes, D. (2002). Experimental studies of heavy-ion slowing down in matter. *Nucl. Instrum. Methods B*, 195(1-2):3–54.

[Geissel et al., 2003] Geissel, H., Weick, H., Winkler, M., Münzenberg, G., Chichkine, V., Yavor, M., Aumann, T., Behr, K. H., Böhmer, M., Brünle, A., Burkard, K., Benlliure, J., Cortina-Gil, D., Chulkov, L., Dael, A., Ducret, J.-E., Emling, H., Franczak, B., Friese, J., Gastineau, B., Gerl, J., Gernhäuser, R., Hellström, M., Jonson, B., Kojouharova, J., Kulessa, R., Kindler, B., Kurz, N., Lommel, B., Mittig, W., Moritz, G., Mühle, C., Nolen, J. A., Nyman, G., Roussell-Chomaz, P., Scheidenberger, C., Schmidt, K.-H., Schrieder, G., Sherrill, B., Simon, H., Sümmerer, K., Tahir, N. A., Vysotsky, V., Wollnik, H., and Zeller, A. F. (2003). The Super-FRS project at GSI. *Nucl. Instrum. Methods B*, 204:71–85.

[Gladnishki et al., 2004] Gladnishki, K. A., Podolyak, Z., Regan, P. H., Gerl, J., Hellstrom, M., Kopatch, Y., Mandal, S., Gorska, M., Page, R. D., Wollersheim, H. J., Banu, A., Benzoni, G., Boardman, H., La Commara, M., Ekman, J., Fahlander, C., Geissel, H., Grawe, H., Kaza, E., Korgul, A., Matos, M., Mineva, M. N., Pearson, C. J., Plettner, C., Rudolph, D., Scheidenberger, C., Schmidt, K.-H., Shishkin, V., Sohler, D., Summerer, K., Valiente-Dobon, J. J., Walker, P. M., Weick, H., Winkler, M., and Yordanov, O. (2004). Angular momentum population in the projectile fragmentation of U-238 at 750 MeV/nucleon. *Phys. Rev. C*, 69(2).

[Goriely et al., 2010] Goriely, S., Chamel, N., and Pearson, J. M. (2010). Further explorations of skyrme-hartree-fock-bogoliubov mass formulas. xii. stiffness and stability of neutron-star matter. *Phys. Rev. C*, 82:035804.

[Grabmayr et al., 1994] Grabmayr, P., Mondry, A., Wagner, G., Woldt, P., Berg, G., Lisantti, J., Miller, D., Nann, H., and Stephenson, E. (1994). 3s-proton occupancies in hg 204 and pb 206. *Physical Review C*, 49(6):2971.

[Gräff et al., 1980] Gräff, G., Kalinowsky, H., and Traut, J. (1980). A direct determination of the proton electron mass ratio. *Z. Physik A*, 297:35–39.

[Greiner, 2013] Greiner, F. (2013). *Construction and Commissioning of an RF Quadrupole Switchyard (in German)*. Bachelor thesis, Justus Liebig University Gießen.

[Greiner et al., 2020] Greiner, F., Dickel, T., Ayet San Andrés, S., Bergmann, J., Constantin, P., Ebert, J., Geissel, H., Haettner, E., Hornung, C., Miskun, I., Lippert, W., Mardor, I., Moore, I., Plaß, W., Purushothaman, S., Rink, A.-K., Reiter, M., Scheidenberger, C., and Weick, H. (2020). Removal of molecular contamination in low-energy RIBs by the isolation–dissociation–isolation method. *Nucl. Instrum. Methods B*, 463:324–326.

[Gröf, 2020] Gröf, L. (2020). Troubleshooting and assembly of the new MNT reaction- and spontaneous fission investigation system for the FRS Ion Catcher. Internal report, Spezialisierungsmodul, Justus-Liebig-Universität Gießen.

[Gröf, 2023] Gröf, L. (2023). In preparation. Master thesis, Justus-Liebig-Universität Gießen.

[Gross and Frenkel, 1976] Gross, R. and Frenkel, A. (1976). Effective interaction of protons and neutrons in the $2p_{1/2} - 1g_{9/2}$ subshells. *Nucl. Phys. A*, 267:85–108.

[Haettner et al., 2020] Haettner, E., Franczak, B., Geissel, H., Dickel, T., Pietri, S., Plaß, W., Prochazka, A., Purushothaman, S., Scheidenberger, C., Tanaka, Y., Terashima, S., Weick, H., Winfield, J., and Yavor, M. (2020). New high-resolution and high-transmission modes of the FRS for FAIR phase-0 experiments. *Nucl. Instrum. Methods B*, 63:455?459.

[Haettner et al., 2018] Haettner, E., Plaß, W. R., Czok, U., Dickel, T., Geissel, H., Kinsel, W., Petrick, M., Schäfer, T., and Scheidenberger, C. (2018). A versatile triple radiofrequency quadrupole system for cooling, mass separation and bunching of exotic nuclei. *Nucl. Instrum. Methods A*, 880:138–151.

[Häfner et al., 2019] Häfner, G., Moschner, K., Blazhev, A., Boutachkov, P., Davies, P., Wadsworth, R., Ameil, F., Baba, H., Bäck, T., Dewald, M., et al. (2019). Properties of γ-decaying isomers in the sn 100 region populated in fragmentation of a xe 124 beam. *Phys. Rev. C*, 100(2):024302.

[Hausmann et al., 2013] Hausmann, M., Aaron, A., Amthor, A., Avilov, M., Bandura, L., Bennett, R., Bollen, G., Borden, T., Burgess, T., Chouhan, S., et al. (2013). Design of the advanced rare isotope separator ARIS at FRIB. *Nuclear Instruments and Methods in Physics Research Section B: Beam Interactions with Materials and Atoms*, 317:349–353.

[Hausmann et al., 2000] Hausmann, M., Attallah, F., Beckert, K., Bosch, F., Dolinskiy, A., Eickhoff, H., Falch, M., Franczak, B., Franzke, B., Geissel, H., Kerscher, T., Klepper, O., Kluge, H.-J., Kozhuharov, C., Löbner, K. E. G., Münzenberg, G., Nolden, F., Novikov, Y. N., Radon, T., Schatz, H., Scheidenberger, C., Stadlmann, J., Steck, M., Winkler, T., and Wollnik, H. (2000). First isochronous mass specrometry at the experimental storage ring ESR. *Nucl. Instrum. Methods A*, 446:569–580.

[Heiße, 2015] Heiße, F. (2015). *Investigation of the cryogenic gas-filled stopping cell for the FRS Ion Catcher*. Master thesis, Technische Universität Dresden.

[Hirayama et al., 2017] Hirayama, Y., Watanabe, Y., Mukai, M., Oyaizu, M., Ahmed, M., Ishiyama, H., Jeong, S., Kakiguchi, Y., Kimura, S., Moon, J., et al. (2017). Doughnut-shaped gas cell for kek isotope separation system. *Nuclear Instruments and Methods in Physics Research Section B: Beam Interactions with Materials and Atoms*, 412:11–18.

[Hjorth-Jensen et al., 1995] Hjorth-Jensen, M., Kuo, T. T. S., and Osnes, E. (1995). Realistic effective interactions for nuclear systems. *Phys. Rep.*, 261(3-4):125–270.

[Hornung, 2018] Hornung, C. (2018). *High-Resolution Experiments with the Multiple-Reflection Time-Of-Flight Mass Spectrometer at the Fragment Separator FRS*. PhD thesis, Justus Liebig University Gießen.

[Hornung et al., 2018] Hornung, C., Amanbayev, D., Ayet San Andrés, S., Bergmann, J., Dickel, T., Geissel, H., Greiner, F., Gröf, L., Plaß, W. R., Rink, A.-K., and Scheidenberger, C. (2018). An upgrade to the RFQ beam line of the FRS Ion Catcher. *GSI-FAIR Sci. Rep. 2017*, 2018-1:p. 116.

[Hornung et al., 2020] Hornung, C., Amanbayev, D., Dedes, I., Kripko-Koncz, G., Miskun, I., Shimizu, N., Ayet San Andrés, S., Bergmann, J., Dickel, T., Dudek, J., Ebert, J., Geissel, H., Górska, M., Grawe, H., Greiner, F., Haettner, E., Otsuka, T., Plaß, W. R., Purushothaman, S., Rink, A.-K., Scheidenberger, C., Weick, H., Bagchi, S., Blazhev, A., Charviakova, O., Curien, D., Finlay, A., Kaur, S., Lippert, W., Otto, J.-H., Patyk, Z., Pietri, S., Tanaka, Y. K., Tsunoda, Y., and Winfield, J. S. (2020). Isomer studies in the vicinity of the doubly-magic nucleus ^{100}Sn: Observation of a new low-lying isomeric state in ^{97}Ag. *Phys. Lett. B*, 802:135200.

[Hu and Zidek, 2002] Hu, F. and Zidek, J. V. (2002). The weighted Likelihood. *Can. J. Stat.*, 30(3):347–371.

[Hu et al., 1999] Hu, Z., Batist, L., Agramunt, J., Algora, A., Brown, B. A., Cano-Ott, D., Collatz, R., Gadea, A., Gierlik, M., Górska, M., Grawe, H., Hellström, M., Janas, Z., Karny, M., Kirchner, R., Moroz, F., Płochocki, A., Rejmund, M., Roeckl, E., Rubio, B., Shibata, M., Szerypo, J., Tain, J. L., and Wittmann, V. (1999). β decay of ^{97}ag: Evidence for the gamow-teller resonance near ^{100}sn. *Phys. Rev. C*, 60:024315.

[Huang et al., 2021] Huang, W., Wang, M., Kondev, F. G., Audi, G., and Naimi, S. (2021). The ame 2020 atomic mass evaluation (i). evaluation of input data, and adjustment procedures. *Chinese Physics C*, 45(3):030002.

[Iwasa et al., 1997] Iwasa, N., Geissel, H., Münzenberg, G., Scheidenberger, C., Schwab, T., and Wollnik, H. (1997). MOCADI, a universal Monte Carlo code for the transport of heavy ions through matter within ion-optical systems. *Nucl. Instrum. Methods B*, 126:284–289.

[Jacobs et al., 2022] Jacobs, A., Andreoiu, C., Bergmann, J., Brunner, T., Dickel, T., Dillmann, I., Dunling, E., Flowerdew, J., Graham, L., Gwinner, G., et al. (2022). Collision-Induced Dissociation at TRIUMF's Ion Trap for Atomic and Nuclear science. *International Journal of Mass Spectrometry*, 482:116931.

[Jain et al., 2015] Jain, A. K., Maheshwari, B., Garg, S., Patial, M., and Singh, B. (2015). Atlas of nuclear isomers. *Nucl. Data Sheets*, 128:1–130.

[Janik et al., 2011] Janik, R., Prochazka, A., Sitar, B., Strmen, P., Szarka, I., Geissel, H., Behr, K.-H., Karagiannis, C., Nociforo, C., Weick, H., and Winkler, M. (2011). Time projection chambers with C-pads for heavy-ion tracking. *Nucl. Intrum. Methods A*, 640:54–57.

[Jesch et al., 2015] Jesch, C., Dickel, T., Plaß, W. R., Short, D., Ayet San Andres, S., Dilling, J., Geissel, H., Greiner, F., Lang, J., Leach, K. G., et al. (2015). The MR-TOF-MS isobar separator for the TITAN facility at TRIUMF. *Hyperfine Interact.*, 235:97–106.

[Jurado et al., 2002] Jurado, B., Schmidt, K.-H., and Behr, K.-H. (2002). Application of a secondary-electron transmission monitor for high-precision intensity measurements of relativistic heavy-ion beams. *Nuclear Instruments and Methods in Physics Research Section A: Accelerators, Spectrometers, Detectors and Associated Equipment*, 483(3):603–610.

[Kaleja et al., 2022] Kaleja, O., Anđelić, B., Bezrodnova, O., Blaum, K., Block, M., Chenmarev, S., Chhetri, P., Droese, C., Düllmann, C. E., Eibach, M., et al. (2022). Direct high-precision mass spectrometry of superheavy elements with shiptrap. *Physical Review C*, 106(5):054325.

[Kaleja, 2020] Kaleja, O. T. (2020). *High-precision mass spectrometry of nobelium, lawrencium and rutherfordium isotopes and studies of long-lived isomers with SHIPTRAP*. PhD thesis, Mainz.

[Karpov and Saiko, 2017] Karpov, A. and Saiko, V. (2017). Modeling near-barrier collisions of heavy ions based on a langevin-type approach. *Physical Review C*, 96(2):024618.

[Kavatsyuk et al., 2007] Kavatsyuk, O., Mazzocchi, C., Janas, Z., Banu, A., Batist, L., Becker, F., Blazhev, A., Brüchle, W., Döring, J., Faestermann, T., Górska, M., Grawe, H., Jungclaus, A., Karny, M., Kavatsyuk, M., Klepper, O., Kirchner, R., La Commara, M., Miernik, K., Mukha, I., Plettner, C., Płochocki, A., Roeckl, E., Romoli, M., Rykaczewski, K., Schädel, M., Schmidt, K., Schwengner, R., and Żylicz, J. (2007). Beta decay of ^{101}sn. *Eur. Phys. J. A*, 31(3):319–325.

[Kessler, 2008] Kessler, T. (2008). *Development and application of laser technologies at radioactive ion beam facilities*. Number 8/2008. University of Jyväskylä.

[Kondev et al., 2021] Kondev, F., Wang, M., Huang, W., Naimi, S., and Audi, G. (2021). The NUBASE2020 evaluation of nuclear physics properties. *Chin. Phys. C*, 45(3):030001.

[Kostyleva, 2020] Kostyleva, D. (2020). *Experimental studies of proton-unbound nuclei via in-flight decay spectroscopy*. PhD thesis, Justus-Liebig-Universität Gießen.

[Kripko-Koncz, 2023] Kripko-Koncz, G. (2023). *Investigation of isomeric states in medium-heavy nuclei using advances in multiple-reflection time-of-flight mass spectrometry*. PhD thesis, Justus-Liebig-Universität Gießen.

[Kubo, 2003] Kubo, T. (2003). In-flight RI beam separator BigRIPS at RIKEN and elsewhere in Japan. *Nucl. Instrum. Methods B*, 204:97–113.

[Kudryavtsev et al., 1996] Kudryavtsev, Y., Andrzejewski, J., Bijnens, N., Franchoo, S., Gentens, J., Huyse, M., Piechaczek, A., Szerypo, J., Reusen, I., Van Duppen, P., Van Den Bergh, P., Vermeeren, L., Wauters, J., and Wöhr, A. (1996). Beams of short lived nuclei produced by selective laser ionization in a gas cell. *Nuclear Instruments and Methods in Physics Research Section B: Beam Interactions with Materials and Atoms*, 114(3):350–365.

[Kudryavtsev et al., 2016] Kudryavtsev, Y., Creemers, P., Ferrer, R., Granados, C., Gaffney, L., Huyse, M., Mogilevskiy, E., Raeder, S., Sels, S., Van den Bergh, P., Van Duppen, P., and Zadvornaya, A. (2016). A new in-gas-laser ionization and spectroscopy laboratory for off-line studies at ku leuven. *Nuclear Instruments and Methods in Physics Research Section B: Beam Interactions with Materials and Atoms*, 376:345–352. Proceedings of the XVIIth International Conference on Electromagnetic Isotope Separators and Related Topics (EMIS2015), Grand Rapids, MI, U.S.A., 11-15 May 2015.

[Kudryavtsev et al., 2013] Kudryavtsev, Y., Ferrer, R., Huyse, M., Van den Bergh, P., and Van Duppen, P. (2013). The in-gas-jet laser ion source: Resonance ionization spectroscopy of radioactive atoms in supersonic gas jets. *Nuclear Instruments and Methods in Physics Research Section B: Beam Interactions with Materials and Atoms*, 297:7–22.

[Kumar et al., 2009] Kumar, R., Molina, F., Pietri, S., Casarejos, E., Algora, A., Benlliure, J., Doornenbal, P., Gerl, J., Gorska, M., Kojouharov, I., et al. (2009). Testing of a dsssd detector for the stopped rising project. *Nuclear Instruments and Methods in Physics Research Section A: Accelerators, Spectrometers, Detectors and Associated Equipment*, 598(3):754–758.

[Landau and Lifshitz, 1987] Landau, L. and Lifshitz, E. (1987). Chapter ii - viscous fluids. In Landau, L. and Lifshitz, E., editors, *Fluid Mechanics (Second Edition)*, pages 44–94. Pergamon, second edition edition.

[Leo, 1994] Leo, W. R. (1994). *Techniques for Nuclear and Particle Physics Experiments*. Springer, Berlin, Heidelberg, New York.

[Lincoln et al., 2013] Lincoln, D. L., Holt, J. D., Bollen, G., Brodeur, M., Bustabad, S., Engel, J., Novario, S. J., Redshaw, M., Ringle, R., and Schwarz, S. (2013). First direct double-β decay Q-value measurement of ^{82}Se in support of understanding the nature of the neutrino. *Phys. Rev. Lett*, 110:012501.

[Lindhard et al., 1996] Lindhard, J., So, A. H., et al. (1996). Relativistic theory of stopping for heavy ions. *Phys. Rev. A*, 53(4):2443.

[Litvinov et al., 2005] Litvinov, Y. A., Geissel, H., Radon, T., Attallah, F., Audi, G., Beckert, K., Bosch, F., Falch, M., Franzke, B., Hausmann, M., Hellström, M., Kerscher, T., Klepper, O., Kluge, H.-J., Kozhuharov, C., Löbner, K. E. G., Münzenberg, G., Nolden, F., Novikov, Y. N., Quint, W., Patyk, Z., Reich, H., Scheidenberger, C., Schlitt, B., Steck, M., Sümmerer, K., Vermeeren, L., Winkler, M., Winkler, T., and Wollnik, H. (2005). Mass measurement of cooled neutron-deficient bismuth projectile fragments with time-resolved Schottky mass spectrometry at the FRS-ESR facility. *Nucl. Phys. A*, 756:3–38.

[Lund et al., 2020] Lund, K., Bollen, G., Lawton, D., Morrissey, D., Ottarson, J., Ringle, R., Schwarz, S., Sumithrarachchi, C., Villari, A., and Yurkon, J. (2020). Online tests of the advanced cryogenic gas stopper at nscl. *Nuclear Instruments and Methods in Physics Research Section B: Beam Interactions with Materials and Atoms*, 463:378–381.

[M. Schädel, 2007] M. Schädel (2007). Superheavy element chemistry at GSI - status and perspectives. *Eur. Phys. J. D*, 45(1):67–74.

[Mardor et al., 2021] Mardor, I., Andrés, S. A. S., Dickel, T., Amanbayev, D., Beck, S., Bergmann, J., Geissel, H., Gröf, L., Haettner, E., Hornung, C., Kalantar-Nayestanaki, N., Kripko-Koncz, G., Miskun, I., Mollaebrahimi, A., Plaß, W. R., Scheidenberger, C., Weick, H., Bagchi, S., Balabanski, D. L., Bezbakh, A. A., Brencic, Z., Charviakova, O., Chudoba, V., Constantin, P., Dehghan, M., Fomichev, A. S., Grigorenko, L. V., Hall, O., Harakeh, M. N., Hucka, J.-P., Kankainen, A., Kiselev, O., Knöbel, R., Kostyleva, D. A., Krupko, S. A., Kurkova, N., Kuzminchuk, N., Mukha, I., Muzalevskii, I. A., Nichita, D., Nociforo, C., Patyk, Z., Pfützner, M., Pietri, S., Purushothaman, S., Reiter, M. P., Roesch, H., Schirru, F., Sharov, P. G., Spătaru, A., Stanic, G., State, A., Tanaka, Y. K., Vencelj, M., Yavor, M. I., and Zhao, J. (2021). Mass measurements of as, se, and br nuclei, and their implication on the proton-neutron interaction strength toward the $n = z$ line. *Phys. Rev. C*, 103:034319.

[Mardor et al., 2020] Mardor, I., Dickel, T., Amanbayev, D., San Andrés, S. A., Beck, S., Benyamin, D., Bergmann, J., Constantin, P., Cuillerier, A. C., Geissel, H., et al. (2020). Determining spontaneous fission properties by direct mass measurements with the FRS Ion Catcher. In *EPJ Web of Conferences*, volume 239, page 02004. EDP Sciences.

[Massey Jr, 1951] Massey Jr, F. J. (1951). The Kolmogorov-Smirnov test for goodness of fit. *Journal of the American statistical Association*, 46(253):68–78.

[Masuda et al., 1972] Masuda, S., Fujibayashi, K., Ishida, K., and Inaba, H. (1972). Confinement and transport of charged aerosol clouds by means of electric curtains. *The transactions of the Institute of Electrical Engineers of Japan.B*, 92(1):9–18.

[Mendoza-Temis et al., 2015] Mendoza-Temis, J. d. J., Wu, M.-R., Langanke, K., Martínez-Pinedo, G., Bauswein, A., and Janka, H.-T. (2015). Nuclear robustness of the r process in neutron-star mergers. *Phys. Rev. C*, 92:055805.

[Miskun, 2019] Miskun, I. (2019). *A Novel Method for the Measurement of Half-Lives and Decay Branching Ratios of Exotic Nuclei with the FRS Ion Catcher*. PhD thesis, Justus-Liebig-Universität Gießen.

[Miskun et al., 2019] Miskun, I., Dickel, T., Mardor, I., Hornung, C., Amanbayev, D., Ayet San Andrés, S., Bergmann, J., Ebert, J., Geissel, H., Górska, M., Greiner, F., Haettner, E., Plaß, W. R., Purushothaman, S., Scheidenberger, C., Rink, A.-K., Weick, H., Bagchi, S., Constantin, P., Kaur, S., Lippert, W., Mei, B., Moore, I., Otto, J.-H., Pietri, S., Pohjalainen, I., Prochazka, A., Rappold, C., Reiter, M. P., Tanaka, Y. K., and Winfield, J. S. (2019). A novel method for the measurement of half-lives and decay branching ratios of exotic nuclei. *Eur. Phys. J. A*, 55(9):148.

[Miskun et al., 2021] Miskun, I., Dickel, T., San Andrés, S. A., Bergmann, J., Constantin, P., Ebert, J., Geissel, H., Greiner, F., Haettner, E., Hornung, C., et al. (2021). Separation of atomic and molecular ions by ion mobility with an rf carpet. *International Journal of Mass Spectrometry*, 459:116450.

[Miskun et al., 2015] Miskun, I., Reiter, M. P., Rink, A., Dickel, T., Ayet San Andrés, S., Ebert, J., Geissel, H., Greiner, F., Haettner, E., Hornung, C., Plaß, W. R., Purushothaman, S., and Scheidenberger, C. (2015). An RFQ based beam line and mass filter to improve identification capabilities at the diagnostics unit of the prototype CSC for the LEB. *GSI Sci. Rep. 2014*, 2015-1:146.

[Mollaebrahimi, 2021] Mollaebrahimi, A. (2021). *Mass and half-life measurements of neutron-deficient isotopes with A 100 and developments for the FRS Ion Catcher and CISE*. PhD thesis, University of Groningen.

[Mollaebrahimi et al., 2023] Mollaebrahimi, A., Hornung, C., Dickel, T., Amanbayev, D., Kripko-Koncz, G., Plaß, W. R., San Andrés, S. A., Beck, S., Blazhev, A., Bergmann, J., et al. (2023). Studying gamow-teller transitions and the assignment of isomeric and ground states at n= 50. *Physics Letters B*, 839:137833.

[Möller et al., 2016] Möller, P., Sierk, A. J., Ichikawa, T., and Sagawa, H. (2016). Nuclear ground-state masses and deformations: FRDM(2012). *At. Data Nucl. Data Tables*, 109:1–204.

[Moore et al., 2013] Moore, I. D., Eronen, T., Gorelov, D., Hakala, J., Jokinen, A., Kankainen, A., Kolhinen, V. S., Koponen, J., Penttilä, H., Pohjalainen, I., Reponen, M., Rissanen, J., Saastamoinen, A., Rinta-Antila, S., Sonnenschein, V., and Äystö, J. (2013). Towards commissioning the new IGISOL-4 facility. *Nucl. Instrum. Methods B*, 317:208–213.

[Mott, 1929] Mott, N. F. (1929). The scattering of fast electrons by atomic nuclei. *Proc. R. Soc. London*, 124(794):425–442.

[Mougeot et al., 2021] Mougeot, M., Atanasov, D., Karthein, J., Wolf, R., Ascher, P., Blaum, K., Chrysalidis, K., Hagen, G., Holt, J., Huang, W., et al. (2021). Mass measurements of 99–101in challenge ab initio nuclear theory of the nuclide 100sn. *Nature Physics*, 17(10):1099–1103.

[Mun et al., 2014] Mun, M.-H., Adamian, G., Antonenko, N., Oh, Y., and Kim, Y. (2014). Production cross section of neutron-rich isotopes with radioactive and stable beams. *Physical Review C*, 89(3):034622.

[Münzenberg et al., 1979] Münzenberg, G., Faust, W., Hofmann, S., Armbruster, P., Güttner, K., and Ewald, H. (1979). The velocity filter SHIP, a separator of unslowed heavy ion fusion products. *Nucl. Instrum. Methods*, 161:65–82.

[Neumayr et al., 2006] Neumayr, J. B., Thirolf, P. G., Habs, D., Heinz, S., Kolhinen, V. S., Sewtz, M., and Szerypo, J. (2006). Performance of the MLL-IonCatcher. *Rev. Sci. Instrum.*, 77:065109.

[Nies et al., 2023] Nies, L., Atanasov, D., Athanasakis-Kaklamanakis, M., Au, M., Blaum, K., Dobaczewski, J., Hu, B., Holt, J., Karthein, J., Kulikov, I., et al. (2023). Isomeric Excitation Energy for In-99m from Mass Spectrometry Reveals Constant Trend Next to Doubly Magic Sn-100. *Physical Review Letters*, 131(2):022502.

[Niwase et al., 2023] Niwase, T., Watanabe, Y., Hirayama, Y., Mukai, M., Schury, P., Andreyev, A., Hashimoto, T., Iimura, S., Ishiyama, H., Ito, Y., et al. (2023). Discovery of New Isotope U-241 and Systematic High-Precision Atomic Mass Measurements of Neutron-Rich Pa-Pu Nuclei Produced via Multinucleon Transfer Reactions. *Physical Review Letters*, 130(13):132502.

[Nörtershäuser and Campbell, 2006] Nörtershäuser, W. and Campbell, P. (2006). LaSpec at FAIR's low energy beam line: A new perspective for laser spectroscopy of radioactive nuclei. *Hyperfine Interact.*, 171:149–156.

[Nowacki, 2002] Nowacki, F. (2002). Shell model description of correlations in ^{56}ni and ^{100}sn. *Nucl. Phys. A*, 704(1):223 – 231.

[Otsuka et al., 2010] Otsuka, T., Suzuki, T., Honma, M., Utsuno, Y., Tsunoda, N., Tsukiyama, K., and Hjorth-Jensen, M. (2010). Novel features of nuclear forces and shell evolution in exotic nuclei. *Phys. Rev. Lett.*, 104(1):012501.

[Pakkanen et al., 1972] Pakkanen, A., Komppa, T., and Helppi, H. (1972). New 204au activity and the decay of 202au. *Nuclear Physics A*, 184(1):157–165.

[Papadakis et al., 2016] Papadakis, P., Moore, I., Pohjalainen, I., Sarén, J., and Uusitalo, J. (2016). Development of a low-energy radioactive ion beam facility for the mara separator. *Hyperfine Interactions*, 237(1):1–10.

[Park et al., 2019] Park, J., Krücken, R., Lubos, D., Gernhäuser, R., Lewitowicz, M., Nishimura, S., Ahn, D. S., Baba, H., Blank, B., Blazhev, A., Boutachkov, P., Browne, F., Čeliković, I., de France, G., Doornenbal, P., Faestermann, T., Fang, Y., Fukuda, N., Giovinazzo, J., Goel, N., Górska, M., Grawe, H., Ilieva, S., Inabe,

N., Isobe, T., Jungclaus, A., Kameda, D., Kim, G. D., Kim, Y.-K., Kojouharov, I., Kubo, T., Kurz, N., Kwon, Y. K., Lorusso, G., Moschner, K., Murai, D., Nishizuka, I., Patel, Z., Rajabali, M. M., Rice, S., Sakurai, H., Schaffner, H., Shimizu, Y., Sinclair, L., Söderström, P.-A., Steiger, K., Sumikama, T., Suzuki, H., Takeda, H., Wang, Z., Watanabe, H., Wu, J., and Xu, Z. Y. (2019). New and comprehensive β- and βp-decay spectroscopy results in the vicinity of $^{100}\mathrm{Sn}$. *Phys. Rev. C*, 99:034313.

[Paschen, 1889] Paschen, F. (1889). Über die zum Funkenübergang in Luft, Wasserstoff und Kohlensäure bei verschiedenen Drucken erforderliche Potentialdifferenz. *Annalen der Physik*, 273(5):69–96.

[Pfützner et al., 1994] Pfützner, M., Geissel, H., Münzenberg, G., Nickel, F., Scheidenberger, C., Schmidt, K.-H., Sümmerer, K., Brohm, T., Voss, B., and Bichsel, H. (1994). Energy deposition by relativistic heavy ions in thin argon absorbers. *Nucl. Instrum. Methods B*, 86:213–218.

[Pierce and Blann, 1968] Pierce, T. and Blann, M. (1968). Stopping powers and ranges of 5-90-mev s 32, cl 35, br 79, and i 127 ions in h 2, he, n 2, ar, and kr: A semiempirical stopping power theory for heavy ions in gases and solids. *Physical Review*, 173(2):390.

[Pietri, 2023] Pietri, S. (2023). Private communication.

[Pietri et al., 2018] Pietri, S., Bruce, A. M., Grahn, T., Plaß, W. R., Scheidenberger, C., Dickel, T., Kelić-Heil, A., Geissel, H., Weick, H., Ameil, F., Arici, T., Audouin, L., Ayet San Andrés, S., Aysto, J., Bagchi, S., Bai, M., Benlliure, S. B. J., Benzoni, G., Bruno, C., Cortina, D., Davisson, T., Gerl, J., Górska, M., Greiner, F., Haettner, E., Hall, O., Brennan, L. H., Heinz, A., Helert, A., Hornung, C., Hucka, J., Jokinen, A., Kankainen, A., Kahl, D., Kindler, B., Kojuharov, I., Kostyleva, D., Kuzminchuk, N., Labiche, M., Woods, C. L., Lomme, B., Matinez Pinedo, G., Miskun, I., Münzenberg, G., Mukha, I., Page, R., Pfützner, M., Podolyak, Z., Prochazka, A., Purushothaman, S., Rappold, C., Regan, P., Ricciardi, M. V., Antila, S. R., Saha, S., Saito, T., Schaffner, H., Schirru, F., Simpson, J., Simon, H., Spiller, P., Stadlmann, J., Taieb, J., Tanaka, Y., Tanihata, I., Vesic, J., Voss, B., Walker, P. M., Woods, P. J., Winfield, J., and Winkler, M. (2018). Search for new neutron-rich isotopes and exploratory studies in the element range from terbium to rhenium. *GSI-FAIR Sci. Rep. 2017*, 2018-1.

[Plaß, 2001] Plaß, W. R. (2001). *The Dependence of RF Ion Trap Mass Spectrometer Performance on Electrode Geometry and Collisional Processes*. PhD thesis, Justus Liebig University Gießen.

[Plaß et al., 2015] Plaß, W. R., Dickel, T., Ayet San Andrés, S., Ebert, J., Greiner, F., Hornung, C., Jesch, C., Lang, J., Lippert, W., Majoros, T., Short, D., Geissel, H., Haettner, E., amd A.-K. Rink, M. P. R., Scheidenberger, C., and Yavor, M. I. (2015). High-performance multiple-reflection time-of-flight mass spectrometers for research with exotic nuclei and for analytical mass spectrometry. *Phys. Scr. T*, 166:014069.

[Plaß et al., 2008a] Plaß, W. R., Dickel, T., Czok, U., Geissel, H., Petrick, M., Reinheimer, K., Scheidenberger, C., and Yavor, M. I. (2008a). Isobar separation by time-of-flight mass spectrometry for low-energy radioactive ion beam facilities. *Nucl. Instrum. Methods B*, 266:4560–4564.

[Plaß et al., 2008b] Plaß, W. R., Dickel, T., Fabian, B., and Haettner, E. (2008b). An advanced concept for mass spectrometry simulations – the Ion Trajectory Simulation program ITSIM 6. In *Proceedings of the 56th ASMS Conference on Mass Spectrometry and Allied Topics*, page MP 015, Denver, USA.

[Plaß et al., 2019] Plaß, W. R., Dickel, T., Mardor, I., Pietri, S., Geissel, H., Scheidenberger, C., Amanbayev, D., San Andrés, S. A., Äystö, J., Balabanski, D. L., et al. (2019). The science case of the FRS Ion Catcher for FAIR Phase-0. *Hyperfine Interact.*, 240(1):73.

[Plaß et al., 2007] Plaß, W. R., Dickel, T., Petrick, M., Boutin, D., Di, Z., Fleckenstein, T., Geissel, H., Jesch, C., Scheidenberger, C., and Wang, Z. (2007). An RF quadrupole-time-of-flight system for isobar-separation and multiplexed low energy rare-isotope beam experiments. *Eur. Phys. J. Special Topics*, 150:367–368.

[Plaß et al., 2013a] Plaß, W. R., Dickel, T., Purushothaman, S., Dendooven, P., Geissel, H., Ebert, J., Haettner, E., Jesch, C., Ranjan, M., Reiter, M. P., Weick, H., Amjad, F., Ayet, S., Diwisch, M., Estrade, A., Farinon, F., Greiner, F., Kalantar-Nayestanaki, N., Knöbel, R., Kurcewicz, J., Lang, J., Moore, I., Mukha, I., Nociforo, C., Petrick, M., Pfuetzner, M., Pietri, S., Prochazka, A., Rink, A.-K., Rinta-Antila, S., Schäfer, D., Scheidenberger, C., Takechi, M., Tanaka, Y. K., Winfield, J. S., and Yavor, M. I. (2013a). The FRS Ion Catcher - a facility for high-precision experiments with stopped projectile and fission fragments. *Nucl. Instrum. Methods B*, 317:457–462.

[Plaß et al., 2013b] Plaß, W. R., Dickel, T., and Scheidenberger, C. (2013b). Multiple-reflection time-of-flight mass spectrometry. *Int. J. Mass Spectrom.*, 349:134–144.

[Podolyák, 2005] Podolyák, Z. (2005). Isomeric decay studies with fragmentation beams. *Acta Physica Polonica B*, 36(4):1269–1279.

[Podolyák et al., 2009] Podolyák, Z., Farrelly, G., Regan, P., Garnsworthy, A., Steer, S., Górska, M., Benlliure, J., Casarejos, E., Pietri, S., Gerl, J., et al. (2009). Proton–hole excitation in the closed shell nucleus 205Au. *Physics Letters B*, 672(2):116–119.

[Pohjalainen, 2018] Pohjalainen, I. (2018). *Gas-phase chemistry, recoil source characterization and in-gas-cell resonance laser ionization of actinides at IGISOL*. PhD thesis, University of Jyväskylä.

[Purushothaman et al., 2017] Purushothaman, S., Ayet San Andrés, S., Bergmann, J., Dickel, T., Ebert, J., Geissel, H., Hornung, C., Plaß, W. R., Rappold, C., Scheidenberger, C., Tanaka, Y. K., and Yavor, M. I. (2017).

Hyper-EMG: A new probability distribution function composed of exponentially modified gaussian distributions to analyze asymmetric peak shapes in high-resolution time-of-flight mass spectrometry. *Int. J. Mass Spectrom.*, 421:245–254.

[Purushothaman et al., 2013] Purushothaman, S., Reiter, M. P., Haettner, E., Dendooven, P., Dickel, T., Geissel, H., Ebert, J., Jesch, C., Plaß, W. R., Ranjan, M., Weick, H., Amjad, F., Ayet, S., Diwisch, M., Estrade, A., Farinon, F., Greiner, F., Kalantar-Nayestanaki, N., Knöbel, R., Kurcewicz, J., Lang, J., Moore, I., Mukha, I., Nociforo, C., Petrick, M., Pfuetzner, M., Pietri, S., Prochazka, A., Rink, A.-K., Rinta-Antila, S., Scheidenberger, C., Takechi, M., Tanaka, Y. K., Winfield, J. S., and Yavor, M. I. (2013). First online results of a cryogenic stopping cell with short-lived heavy uranium fragments produced at 1000 MeV/u. *Eur. Phys. Lett.*, 104:42001.

[R Core Team, 2021] R Core Team (2021). *R: A Language and Environment for Statistical Computing*. R Foundation for Statistical Computing, Vienna, Austria.

[Raeder et al., 2016] Raeder, S., Bastin, B., Block, M., Creemers, P., Delahaye, P., Ferrer, R., Fléchard, X., Franchoo, S., Ghys, L., Gaffney, L., et al. (2016). Developments towards in-gas-jet laser spectroscopy studies of actinium isotopes at LISOL. *Nuclear Instruments and Methods in Physics Research Section B: Beam Interactions with Materials and Atoms*, 376:382–387.

[Raeder et al., 2014] Raeder, S., Heggen, H., Lassen, J., Ames, F., Bishop, D., Bricault, P., Kunz, P., Mjøs, A., and Teigelhöfer, A. (2014). An ion guide laser ion source for isobar-suppressed rare isotope beams. *Rev. Sci. Instrum.*, 85:033309.

[Ranjan, 2012] Ranjan, M. (2012). *Design and Characterization of a Cryogenic Stopping Cell for Radioactive Ions*. PhD thesis, KVI, University of Groningen.

[Rauth et al., 2008] Rauth, C., Ackermann, D., Blaum, K., Block, M., Chaudhuri, A., Di, Z., Eliseev, S., Ferrer, R., Habs, D., Herfurth, F., Heßberger, F. P., Hofmann, S., Kluge, H.-J., Maero, G., Martin, A., Marx, G., Mukherjee, M., Neumayr, J. B., Plaß, W. R., Rahaman, S., Rodriguez, D., Scheidenberger, C., Schweikhard, L., Thirolf, P. G., Vorobjev, G., and Weber, C. (2008). First Penning trap mass measurements beyond the proton drip line. *Phys. Rev. Lett.*, 100:012501.

[Reiter, 2015] Reiter, M. P. (2015). *Pilot Experiments with Relativistic Uranium Projectile and Fission Fragments Thermalized in a Cryogenic Gas-Filled Stopping Cell*. PhD thesis, Justus Liebig University Gießen.

[Reiter et al., 2016] Reiter, M. P., Rink, A.-K., Dickel, T., Haettner, E., Heiße, F., Plaß, W. R., Purushothaman, S., Amjad, F., Ayet San Andrés, S., Bergmann, J., Blum, D., Dendooven, P., Diwisch, M., Ebert, J., Geissel, H., Greiner, F., Hornung, C., Jesch, C., Kalantar-Nayestanaki, N., Knöbel, R., Lang, J., Lippert, W., Miskun, I., Moore, I. D., Nociforo, C., Petrick, M., Pietri, S., Pfützner, M., Pohjalainen, I., Prochazka, A., Scheidenberger, C., Takechi, M., Tanaka, Y. K., Weick, H., Winfield, J. S., and Xu, X. (2016). Rate capability of a cryogenic

stopping cell for uranium projectile fragments produced at 1000 MeV/u. *Nucl. Instrum. Methods B*, 376:240–245.

[Ringle et al., 2021] Ringle, R., Bollen, G., Lund, K., Nicoloff, C., Schwarz, S., Sumithrarachchi, C., and Villari, A. (2021). Particle-in-cell techniques for the study of space charge effects in the advanced cryogenic gas stopper. *Nuclear Instruments and Methods in Physics Research Section B: Beam Interactions with Materials and Atoms*, 496:61–70.

[Rink, 2017] Rink, A.-K. (2017). *Mass and Life-Time Measurement of the 1.7 ms ^{215}Po Isotope - A crucial Test of the Novel Concept of the Cryogenic Ion Catcher for the Super FRS at GSI-FAIR*. PhD thesis, Justus Liebig University Gießen.

[Rodriguez, 2013] Rodriguez, D. (2013). The advanced trapping facility MATS at FAIR. *Int. J. Mass Spectrom.*, 349-350:255–263.

[Roeckl, 2001] Roeckl, E. (2001). Decay experiments on n z nuclei: The role of masses, q values and separation energies. *Hyperfine Interactions*, 132:153–161.

[Rosenbusch et al., 2023] Rosenbusch, M., Wada, M., Chen, S., Takamine, A., Iimura, S., Hou, D., Xian, W., Yan, S., Schury, P., Hirayama, Y., et al. (2023). The new mrtof mass spectrograph following the zerodegree spectrometer at riken's ribf facility. *Nuclear Instruments and Methods in Physics Research Section A: Accelerators, Spectrometers, Detectors and Associated Equipment*, 1047:167824.

[Rotaru et al., 2022] Rotaru, A., Amanbayev, D., Balabanski, D. L., Benyamin, D., Constantin, P., Dickel, T., Gröf, L., Mardor, I., Miskun, I., Nichita, D., et al. (2022). Increase: An in-cell reaction system for multi-nucleon transfer and spontaneous fission at the frs ion catcher. *Nuclear Instruments and Methods in Physics Research Section B: Beam Interactions with Materials and Atoms*, 512:83–90.

[Rubio, 2006] Rubio, B. (2006). Decay spectroscopy (DESPEC) at the new FAIR-NUSTAR facility. *International Journal of Modern Physics E*, 15(08):1979–1988.

[Savard, 2011] Savard, G. (2011). Large radio-frequency gas catchers and the production of radioactive nuclear beams. *J. Phys: Conf. Series*, 312:052004.

[Savard et al., 2016] Savard, G., Levand, A., and Zabransky, B. (2016). The CARIBU gas catcher. *Nuclear Instruments and Methods in Physics Research Section B: Beam Interactions with Materials and Atoms*, 376:246–250.

[Savory et al., 2009] Savory, J., Schury, P., Bachelet, C., Block, M., Bollen, G., Facina, M., Folden III, C. M., Guenaut, C., Kwan, E., Kwiatkowski, A. A., Morrissey, D. J., Pang, G. K., Prinke, A., Ringle, R., Schatz, H., Schwarz, S., and Sumithrarachchi, C. S. (2009). rp process and masses of N $\approx$ Z $\approx$ 34 nuclides. *Phys. Rev. Lett*, 102:132501.

[Scheidenberger et al., 1994] Scheidenberger, C., Geissel, H., Mikkelsen, H., Nickel, F., Brohm, T., Folger, H., Irnich, H., Magel, A., Mohar, M., Münzenberg, G., et al. (1994). Direct observation of systematic deviations from the bethe stopping theory for relativistic heavy ions. *Phys. Rev. Lett.*, 73(1):50.

[Schury et al., 2006] Schury, P., Bollen, G., Block, M., Morrissey, D., Ringle, R., Prinke, A., Savory, J., Schwarz, S., and Sun, T. (2006). Beam purification techniques for low energy rare isotope beams from a gas cell. *Hyperfine Interact.*, 173:165–170.

[Schury et al., 2016] Schury, P., Wada, M., Ito, Y., Arai, F., Kaji, D., Kimura, S., Morimoto, K., Haba, H., Jeong, S., Koura, H., et al. (2016). Status of the low-energy super-heavy element facility at riken. *Nuclear Instruments and Methods in Physics Research Section B: Beam Interactions with Materials and Atoms*, 376:425–428.

[Schwarz, 2011] Schwarz, S. (2011). Rf ion carpets: The electric field, the effective potential, operational parameters and an analysis of stability. *International Journal of Mass Spectrometry*, 299(2-3):71–77.

[Shibata et al., 2011] Shibata, K., Iwamoto, O., Nakagawa, T., Iwamoto, N., Ichihara, A., Kunieda, S., Chiba, S., Furutaka, K., Otuka, N., Ohsawa, T., et al. (2011). Jendl-4.0: a new library for nuclear science and engineering. *Journal of Nuclear Science and Technology*, 48(1):1–30.

[Shikegava et al., 2021] Shikegava, Y., Yamaguchi, A., Sato, N., Takamine, A., Wada, M., and Haba, H. (2021). Measurement of extraction time and efficiency of 220Rn ions using a cryogenic RF-carpet gas cell for the chemistry of superheavy elements. *RIKEN Accel. Prog. Rep.*, 54:145.

[Sobiczewski and Litvinov, 2014] Sobiczewski, A. and Litvinov, Y. A. (2014). Accuracy of theoretical descriptions of nuclear masses. *Phys. Rev. C*, 89:024311.

[Sonoda et al., 2020] Sonoda, T., Katayama, I., Wada, M., Iimura, H., Sonnenschein, V., Iimura, S., Takamine, A., Rosenbusch, M., Kojima, T. M., Ahn, D. S., Fukuda, N., Kubo, T., Nishimura, S., Shimizu, Y., Sumikama, T., Suzuki, H., Takeda, H., Tanigaki, M., Tomita, H., Yoshida, K., and Ishiyama, H. (2020). First confirmation of stopped RIs at parasitic gas cell with new approach. *RIKEN Accel. Prog. Rep. 2019*, 53:105.

[Sonoda et al., 2016] Sonoda, T., Tsubota, T., Wada, M., Katayama, I., M., T., Kojima, and Reponen, M. (2016). A gas circulation and purification system for gas-cell-based low-energy RI-beam production. *Rev. Sci. Instrum.*, 87:065104.

[Sonoda et al., 2013] Sonoda, T., Wada, M., Tomita, H., Sakamoto, C., Takatsuka, T., Furukawa, T., Iimura, H., Ito, Y., Kubo, T., Matsuo, Y., et al. (2013). Development of a resonant laser ionization gas cell for high-energy, short-lived nuclei. *Nuclear Instruments and Methods in Physics Research Section B: Beam Interactions with Materials and Atoms*, 295:1–10.

[Spătaru et al., 2020] Spătaru, A., Balabanski, D., Beliuskina, O., Constantin, P., Dickel, T., Hornung, C., Kankainen, A., Karpov, A., Nichita, D., Plass, W., et al. (2020). Production of exotic nuclei via mnt reactions using gas cells. *Acta Physica Polonica B*, 51(3).

[Spătaru et al., 2022] Spătaru, A., Hornung, C., Dickel, T., Haettner, E., Pietri, S., San Andrés, S. A., Bagchi, S., Balabanski, D., Bergmann, J., Ebert, J., et al. (2022). First coupling of the frs particle identification and the frs-ion catcher data acquisition systems: The case of 109in. *Nuclear Instruments and Methods in Physics Research Section B: Beam Interactions with Materials and Atoms*, 522:32–37.

[State et al., 2022] State, A., Beck, S., Amanbayev, D., Balabanski, D., Brand, H., Constantin, P., Dickel, T., Hornung, C., Nichita, D., Plaß, W., et al. (2022). The slow control system of the frs ion catcher. *Nuclear Instruments and Methods in Physics Research Section A: Accelerators, Spectrometers, Detectors and Associated Equipment*, 1034:166772.

[State, 2022] State, A.-N. (2022). *Ion transport and extraction with gas flows in next generation ion catchers*. PhD thesis, University Polytechnica of Bucharest.

[Steck and Litvinov, 2020] Steck, M. and Litvinov, Y. A. (2020). Heavy-ion storage rings and their use in precision experiments with highly charged ions. *Progress in Particle and Nuclear Physics*, 115:103811.

[Stephan and Atlas, 2010] Stephan, P. and Atlas, V. H. (2010). B1 Fundamentals of Heat Transfer. *VDI Heat Atlas*, pages 15–30.

[Sternberg et al., 2015] Sternberg, M. G., Segel, R., Scielzo, N. D., Savard, G., Clark, J. A., Bertone, P. F., Buchinger, F., Burkey, M., Caldwell, S., Chaudhuri, A., Crawford, J. E., Deibel, C. M., Greene, J., Gulick, S., Lascar, D., Levand, A. F., Li, G., Galvan, A. P., Sharma, K. S., Schelt, J. V., Yee, R. M., and Zabransky, B. J. (2015). Limit on tensor currents from ^{8}Li β decay. *Phys. Rev. Lett*, 115:182501.

[Stolz et al., 1999] Stolz, A., Faestermann, T., Körner, H.-J., Schneider, R., Wefers, E., and Winkler, S. (1999). A detector system for the identification of relativistic heavy ions at high rates. *GSI Scientific Report 1998*, page 174.

[Stone, 1991] Stone, R. E. (1991). Some average distance results. *Transportation Science*, 25(1):83–90.

[Takamine et al., 2019] Takamine, A., Rosenbuch, M., Wada, M., Schury, P., Moon, J., Sonoda, T., Kojima, T., Katayama, I., Watanabe, Y., Ueno, H., and Ishiyama, H. (2019). Offline test for RF carpet transportation in RF ion guide gas cell at the SLOWRI facility. *RIKEN Accel. Prog. Rep.*, 52:139.

[Takamine et al., 2005] Takamine, A., Wada, M., Ishida, Y., Nakamura, T., Okada, K., Yamazaki, Y., Kambara, T., Kanai, Y., Kojima, T. M., Nakai, Y., Oshima, N., Yoshida, A., Kubo, T., Ohtani, S., Noda, K., Katayama, I., Hostain, P., Varentsov,

V., and Wollnik, H. (2005). Space-charge effects in the catcher gas cell of a rf ion guide. *Rev. Sci. Instrum.*, 76:103503.

[Takamine et al., 2014] Takamine, A., Wada, M., Okada, K., Sonoda, T., Schury, P., Nakamura, T., Kanai, Y., Kubo, T., Katayama, I., Ohtani, S., Wollnik, H., and Schuessler, H. A. (2014). Hyperfine structure constant of the neutron halo nucleus $^{11}Be^{+}$. *Phys. Rev. Lett.*, 112:162502.

[Tarasov and Bazin, 2008] Tarasov, O. B. and Bazin, D. (2008). LISE++: Radioactive beam production with in-flight separators. *Nucl. Instrum. Methods B*, 266(19-20):4657–4664.

[Taskinen et al., 1989] Taskinen, P., Penttilä, H., Äystö, J., Dendooven, P., Jauho, P., Jokinen, A., and Yoshii, M. (1989). Efficiency and delay of the fission ion guide for on-line mass separation. *Nuclear Instruments and Methods in Physics Research Section A: Accelerators, Spectrometers, Detectors and Associated Equipment*, 281(3):539–546.

[Togashi et al., 2018] Togashi, T., Tsunoda, Y., Otsuka, T., Shimizu, N., and Honma, M. (2018). Novel shape evolution in sn isotopes from magic numbers 50 to 82. *Phys. Rev. Lett.*, 121:062501.

[Tolmachev et al., 1997] Tolmachev, A. V., Chernushevich, I. V., Dodonov, A. F., and Standing, K. G. (1997). A collisional focusing ion guide for coupling an atmospheric pressure ion source to a mass spectrometer. *Nucl. Instrum. Methods B*, 124:112–119.

[Varentsov and Yakushev, 2019] Varentsov, V. and Yakushev, A. (2019). Concept of a new universal high-density gas stopping cell setup for study of gas-phase chemistry and nuclear properties of super heavy elements (unicell). *Nuclear Instruments and Methods in Physics Research Section A: Accelerators, Spectrometers, Detectors and Associated Equipment*, 940:206–214.

[Varentsov and Yakushev, 2021] Varentsov, V. and Yakushev, A. (2021). Fair-wind gas cell for the unicell setup. *Nuclear Instruments and Methods in Physics Research Section A: Accelerators, Spectrometers, Detectors and Associated Equipment*, 1010:165487.

[Vermeeren et al., 1994] Vermeeren, L., Bijnens, N., Huyse, M., Kudryavtsev, Y. A., Van Duppen, P., Wauters, J., Qamhieh, Z., Thoen, P., Vandeweert, E., and Silverans, R. (1994). An on-line laser ion source based on resonance photoionization in a gas cell. *Physical review letters*, 73(14):1935.

[von der Wense et al., 2016] von der Wense, L., Seiferle, B., Laatiaoui, M., Neumayr, J. B., Maier, H.-J., Wirth, H.-F., Mokry, C., Runke, J., Eberhardt, K., Duellmann, C. E., Trautmann, N. G., and Thirolf, P. G. (2016). Direct detection of the ^{229}Th nuclear clock transition. *Nature*, 533(7601):47–51.

[Voss et al., 1995] Voss, B., Brohm, T., Clerc, H.-G., Grewe, A., Hanelt, E., Heinz, A., De Jong, M., Junghans, A., Morawek, W., Röhl, C., et al. (1995). The

scintillation-detector equipment of the gsi projectile—fragment separator. *Nuclear Instruments and Methods in Physics Research Section A: Accelerators, Spectrometers, Detectors and Associated Equipment*, 364(1):150–158.

[Wada, 2013] Wada, M. (2013). Genealogy of gas cells for low-energy RI-beam production. *Nucl. Instrum. Methods B*, 317:450–456.

[Wada et al., 2003] Wada, M., Ishida, Y., Nakamura, T., Yamazaki, Y., Kambara, T., Ohyama, H., Kanai, Y., Kojima, T. M., Nakai, Y., Ohshima, N., Yoshida, A., Kubo, T., Matsuo, Y., Fukuyama, Y., Okada, K., Sonoda, T., Ohtani, S., Noda, K., Kawakami, H., and Katayama, I. (2003). Slow RI-beams from projectile fragment separators. *Nucl. Instrum. Methods B*, 204:570–581.

[Wang et al., 2017] Wang, M., Audi, G., Kondev, F. G., Huang, W. J., Naimi, S., and Xu, X. (2017). The AME2016 atomic mass evaluation (II). Tables, graphs and references. *Chin. Phys. C*, 41(3):030003.

[Wang et al., 2021] Wang, M., Huang, W., Kondev, F. G., Audi, G., and Naimi, S. (2021). The ame 2020 atomic mass evaluation (II). tables, graphs and references. *Chinese Physics C*, 45(3):030003.

[Wang and Liu, 2011] Wang, N. and Liu, M. (2011). Nuclear mass predictions with a radial basis function approach. *Physical Review C*, 84(5):051303.

[Ward et al., 1967] Ward, T., Ihochi, H., Karras, M., and Meason, J. (1967). New isotope au 204 and decay of au 202. *Physical Review*, 164(4):1545.

[Wasserheß, 2020] Wasserheß, M. (2020). Efficiency for spontaneous fission products extracted from a cryogenic stopping cell: A comparison between model and experiment. Internal report, Studienprojekt, Justus-Liebig-Universität Gießen.

[Watanabe et al., 2015] Watanabe, Y., Kim, Y., Jeong, S., Hirayama, Y., Imai, N., Ishiyama, H., Jung, H., Miyatake, H., Choi, S., Song, J., et al. (2015). Pathway for the production of neutron-rich isotopes around the N=126 shell closure. *Physical review letters*, 115(17):172503.

[Weaver and Westphal, 2002] Weaver, B. and Westphal, A. (2002). Energy loss of relativistic heavy ions in matter. *Nuclear Instruments and Methods in Physics Research Section B: Beam Interactions with Materials and Atoms*, 187(3):285–301.

[Weick et al., 2018] Weick, H., Geissel, H., Iwasa, N., Scheidenberger, C., and Sanchez, J. R. (2018). Improved accuracy of the code ATIMA for energy loss of heavy ions in matter. *GSI Sci. Rep. 2017*, 2018-1:130.

[Weick et al., 2000] Weick, H., Geissel, H., Scheidenberger, C., Attallah, F., Baumann, T., Cortina, D., Hausmann, M., Lommel, B., Münzenberg, G., Nankov, N., Nickel, F., Radon, T., Schatz, H., Schmidt, K., Stadlmann, J., Sümmerer, K., Winkler, M., and Wollnik, H. (2000). Slowing down of relativistic few-electron heavy ions. *Nucl. Instrum. Methods B*, 164-165:168–179.

[Weick et al., 2002] Weick, H., Sørensen, A., Geissel, H., Scheidenberger, C., Attallah, F., Chichkine, V., Elisseev, S., Hausmann, M., Irnich, H., Litvinov, Y., et al. (2002). Energy-loss straggling of (200–1000) mev/u uranium ions. *Nucl. Instrum. Methods B*, 193(1-4):1–7.

[Weisend, 1998] Weisend, J. G. (1998). *Handbook of cryogenic engineering*. Taylor and Francis, Philadelphia, Pa. englisch.

[Will, 2019] Will, C. (2019). *Achieving One Million Mass Resolving Power with a Multiple-Reflection Time-of-Flight Mass Spectrometer*. Master thesis, Justus Liebig University Gießen.

[Wolf et al., 2013] Wolf, R., Wienholtz, F., Atanasov, D., Beck, D., Blaum, K., Borgmann, C., Herfurth, F., Kowalska, M., Kreim, S., Litvinov, Y. A., et al. (2013). ISOLTRAP's multi-reflection time-of-flight mass separator/spectrometer. *Int. J. Mass Spectrom.*, 349-350:123–133.

[Wollnik, 1987] Wollnik, H. (1987). Laterally and longitudinally dispersive recoil mass separators. *Nuclear Instruments and Methods in Physics Research Section B: Beam Interactions with Materials and Atoms*, 26(1-3):267–272.

[Wollnik and Przewloka, 1990] Wollnik, H. and Przewloka, M. (1990). Time-of-flight mass spectrometers with multiply reflected ion trajectories. *Int. J. Mass Spectrom. Ion Processes*, 96:267–274.

[Wu et al., 2006] Wu, G., Cooks, R. G., Ouyang, Z., Yu, M., Chappell, W. J., and Plass, W. R. (2006). Ion trajectory simulation for electrode configurations with arbitrary geometries. *J. Am. Soc. Mass Spectrom.*, 17:1216–1228.

[Xu et al., 2019] Xu, X., Liu, J. H., Yuan, C. X., Xing, Y. M., Wang, M., Zhang, Y. H., Zhou, X. H., Litvinov, Y. A., Blaum, K., Chen, R. J., Chen, X. C., Fu, C. Y., Gao, B. S., He, J. J., Kubono, S., Lam, Y. H., Li, H. F., Liu, M. L., Ma, X. W., Shuai, P., Si, M., Sun, M. Z., Tu, X. L., Wang, Q., Xu, H. S., Yan, X. L., Yang, J. C., Yuan, Y. J., Zeng, Q., Zhang, P., Zhou, X., Zhan, W. L., Litvinov, S., Audi, G., Naimi, S., Uesaka, T., Yamaguchi, Y., Yamaguchi, T., Ozawa, A., Sun, B. H., Kaneko, K., Sun, Y., and Xu, F. R. (2019). Masses of ground and isomeric states of ^{101}in and configuration-dependent shell evolution in odd-a indium isotopes. *Phys. Rev. C*, 100:051303.

[Yavor et al., 2015] Yavor, M. I., Plaß, W. R., Dickel, T., Geissel, H., and Scheidenberger, C. (2015). Ion-optical design of a high-performance multiple-reflection time-of-flight mass spectrometer and isobar separator. *Int. J. Mass Spectrom.*, 381-382:1–9.

[Zhang et al., 2023] Zhang, M., Zhou, X., Wang, M., Zhang, Y., Litvinov, Y. A., Xu, H., Chen, R., Deng, H., Fu, C., Ge, W., et al. (2023). B ρ-defined isochronous mass spectrometry and mass measurements of 58 ni fragments. *The European Physical Journal A*, 59(2):27.

[Ziegler et al., 2010] Ziegler, J. F., Ziegler, M. D., and Biersack, J. P. (2010). SRIM - the stopping and range of ions in matter (2010). *Nucl. Instrum. Methods B*, 268:1818–1823.